Evolution and Non-Linear Consequences of Magnetic Twists in Flowing Plasmas

Thomas Williams

Supervised by: Dr Youra Taroyan

Physics Department

Aberystwyth University

A thesis submitted for the degree of

Doctor of Philosophy

May 2017

Word count of thesis: .....

Declaration

This work has not previously been accepted in substance for any degree and is not concurrently submitted in candidature for any degree.

Signed .....(candidate)

Date .....

Statement 1

This thesis is the result of my own investigations, except where otherwise stated. Where correction services have been used, the extent and nature of the correction is clearly marked in a footnote(s). Other sources are acknowledged by footnotes giving explicit references. A bibliography is appended.

Signed .....(candidate)

Date .....

Statement 2

I hereby give consent for my thesis, if accepted, to be available for photocopying and for interlibrary loan, and for the title and summary to be made available to outside organisations.

Signed .....(candidate)

Date .....

Acknowledgements

Firstly, I would like to thank Youra for his friendship, encouragement, and continual guidance during the last few years as my supervisor. I look forward to continuing our friendship and collaboration in the future. My fellow PhD candidates and friends; Paddy, Daniel, Dylan, and Jay for all the memories. Finally, a special thanks goes to my parents, Alun and Charlotte; my sister, Emily; and my loving girlfriend, Alex, for their support.

Abstract

In this thesis the overarching investigation is the interaction of Alfvén waves with flowing plasmas. The main consequence of this interaction is that Alfvén waves are amplified in proximity of negative flow gradients. This amplification is investigated using three numerical models. The first and third studies implement fully non-linear Magnetohydrodynamics (MHD) systems, whereas the second study is a combination of a linear model and analytics. All studies adopt the thin flux tube approximation in 1.5-D MHD.

In the first study, the flow is supersonic yet sub-Alfvénic and undergoes a classical shock. The flow in this case is akin to the Evershed effect in sunspots. This is the first numerical confirmation that a shock may lead to Alfvén wave amplification through over-reflection. This over-reflection may only occur when an instability criterion is upheld. The amplification of the Alfvénic pulse leads to pressure perturbations which destabilise the shock. A global twist of the flux tube is generated where $B_\theta \approx B_z$.

The linear study investigates the wave-flow coupling for a decelerating downflow in an intergranular lane. This shows that a negative flow gradient leads to amplification of Alfvén waves. The spatial and temporal evolution of the amplified Alfvén waves in the presence of the smooth plasma flow are investigated.

The final study is an extension of the sunspot model and is applicable to prominence formation. Here, the wave-flow coupling is extended into the non-linear regime and the introduction of a second footpoint

leads to amplification for any supersonic flow speed. The key results from this study is that the global twist generated by the mechanism now reaches $B_\theta \approx 5B_z$. This causes a reversal of the flow in the descending leg of the structure due to the wave-flow coupling, leading to a density increase of about 30 times its original value.

Contents

List of Figures

Chapter 1

Introduction

The aim of this thesis is to numerically investigate the behaviour of Alfvén waves within flowing plasmas in context of the Sun and its atmosphere. The results of the following chapters will discuss the implications of the wave-flow interactions with respect to sunspots, intergranular downflows, and loops. In this chapter, we will begin with a brief overview of the fundamental literature. The main focus will be background material on the solar atmosphere, MHD theory, and waves.

1.1 The Solar Atmosphere

The nature of the solar atmosphere is vastly different to our own atmosphere on Earth. It is composed of ionised gas called plasma and has numerous complex structures, which are contorted by the magnetic field lines and dominate the landscape. Even the regions of quiet Sun where no visible structures can be seen are likely to consist of smaller, unresolved magnetic structures. The surface, or photosphere, is the region where optical photons originate. Moving up through the photosphere leads to a temperature decrease until it reaches a minimum of 4400 K. This temperature minimum defines the top of the photosphere and is some 525 km above optical depth unity for wavelengths of 500 nm. On average, the optical depth, $\tau_\lambda = 2/3$ for a given wavelength, λ leads to the effective temperature of the photosphere where, $T = 5777$ K [Carroll and Ostlie, 2006, p.360].

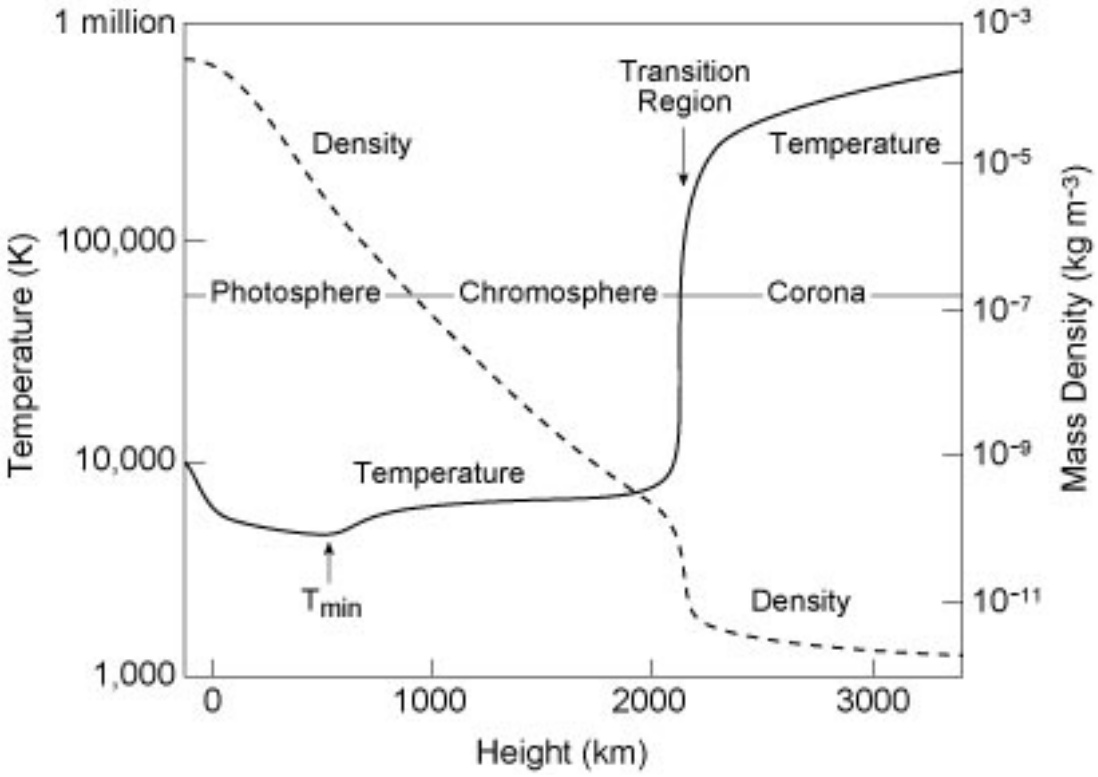

Figure 1.1: A schematic of the solar atmosphere. Temperature and density variations through the photosphere, chromosphere, transition region, and corona are shown. Image courtesy of: http://astro.phys.sc.chula.ac.th/news/April07/070404B_02.jpg

Above the photosphere is the lowest portion of the solar atmosphere - the chromosphere. This layer of the atmosphere is approximately 2,000 km thick and the temperature increases from $5,500$ K at the photosphere to about $10,000$ K just below the transition region. Above this is the corona. The two regions are separated by a thin layer called the transition region. Temperature rapidly increases here, whereas density decreases (Figure 1.1). Recent observations show that this classical view is not strictly accurate as the transition region is highly dynamic and variable.

Heat flowing from the corona into the chromosphere ionises hydrogen atoms, creating this layer between the hot corona and underlying chromosphere. The

temperature continues to increase in the corona and may reach values over 2 MK. Loops, coronal holes and active regions are just some of the features that occur in the corona.

The plasma-β is a ratio of the thermal pressure to magnetic pressure and is discussed in §1.2.1. Plasma, such as that contained within coronal loops, has a low plasma-β value. This means the plasma is 'tied-in' to the magnetic field and the shape, orientation, and size of these structures is determined by the field lines. Contrary to this, plasma in the solar wind has a high plasma-β. This means that rather than the magnetic field lines dictating the motion of the plasma, it is the plasma that determines the field line orientation.

As the corona is much hotter than the underlying chromosphere and photosphere, it led to an issue in solar physics during the 20^{th} century - the coronal heating problem. One phenomenon that may help explain this problem is Alfvén waves. It is possible that Alfvén waves formed within the Sun carry energy through the chromosphere and into the corona where it is dissipated as heat energy. A consequence of such a mechanism is the formation of a spicule-like structure within the chromosphere. It is generally accepted that this is how spicules are formed and they may play a pivotal role in heating the corona [Hollweg et al., 1982; Kudoh and Shibata, 1999].

1.1.1 Solar Spicules and Spicule-Like Features

The chromosphere is comprised of long, thin jets of plasma. These dynamic structures when on the limb are called spicules. However, if these structures are observed in active regions and quiet Sun locations they are called fibrils and mottles, respectively [Tsiropoula et al., 2012]. In recent years, improved spatial resolution has aided the study of these features. Previously, there were numerous contradictory publications as to the height, width, and temperatures of these structures, though density measurements were fairly consistent [James et al., 2003]. These contradicting reports are due to the fact that spicules were at the spatial resolution limitations of previous instruments [Sterling, 2000]. *Hinode* led

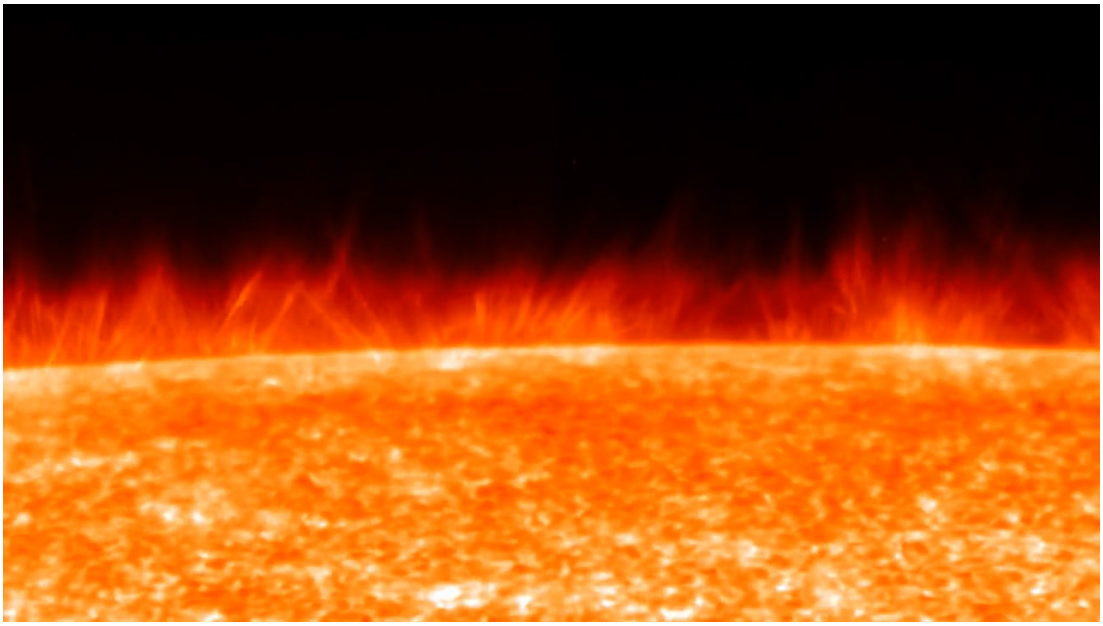

Figure 1.2: This *Hinode* image shows the thread-like appearance of spicules in the solar chromosphere. Image courtesy of: https://svs.gsfc.nasa.gov/12377.

to the discovery of a new spicule-type with different properties [De Pontieu et al., 2007] and bringing about two classifications for spicules - Type-I and Type-II. Type-I are the classical spicules whereas Type-II spicules are the newly discovered and highly debated variety [Klimchuk, 2012; Zhang et al., 2012].

Type-I spicules typically have rise velocities of $15 - 40$ km s^{-1} and reach heights of $3 - 5$ Mm above the photosphere. They have typical lifetimes of 150-400 s. Type-II spicules are more dynamic with ascending velocities of $30 - 110$ km s^{-1}, reach greater heights above the photosphere, and are shorter-lived structures with lifetimes of $50 - 150$ s. Unlike Type-I spicules, the Type-II variant are not seen to fall down but rather they fade into the background around their maximum length [Pereira et al., 2012].

Despite the improved spatial and temporal resolution of instruments, observations alone fail to explain the formation and behaviour of spicules as well as their role in coronal heating. Numerical models, such as those discussed in Sterling

[2000], attempt to describe the theory that observations alone cannot sufficiently explain.

1.1.2 Coronal Seismology and Waves in the Solar Atmosphere

Leighton [1960] discovered that oscillating regions of periodicity 5 minutes span the photosphere and low chromosphere. These oscillations are caused by global acoustic waves trapped beneath the solar surface in a resonant cavity. Here, they are free to propagate and display velocity amplitudes $\approx 0.4\ km\ s^{-1}$ and slowly increase with height until upward vertical and horizontal phase speeds of $30 - 100\ km\ s^{-1}$ are observed [Priest, 2014].

In the chromosphere these oscillations have a wide range of periodicities, but the main power is concentrated around $300\ s$. In the photosphere, these oscillations have no phase difference, which suggests the waves are evanescent; this is not the case in the chromosphere with the oscillations propagating at $\approx c_S$. The transition region displays fluctuations of $2 - 3\ km\ s^{-1}$ with indiscernible periodicities due to the fact they are destroyed as they propagate through the inhomogeneous chromosphere.

Using observed oscillations as a diagnostic tool for determining plasma properties in the corona was suggested originally by Uchida [1970] and subsequently expanded upon by Roberts et al. [1984]. The technique uses the properties of the many different waves detected in the corona to infer properties that cannot be directly measured such as the magnetic field, heating rate, finite structuring, and transport coefficients. Until recently, the application of coronal seismology had been limited due to a lack of high-quality coronal oscillation observations. The launch of SoHO (*Solar Heliospheric Observatory*) and TRACE (*Transition Region and Coronal Explorer*) lead to waves and oscillations being observed in a wide variety of coronal structures [Ballester, 2006]. The applications of coronal seismology now extend beyond the solar corona [Banerjee et al., 2007]. For reviews on coronal seismology, please see: Ballester et al. [2007]; De Moortel and

Nakariakov [2012]; Erdélyi and Goossens [2011].

1.2 Magnetohydrodynamics

Magnetohydrodynamics (MHD), is the study of electrically conducting fluids and their magnetic properties. Examples include salt water, plasma, and liquid metals. The fundamental concept of MHD is that magnetic fields can induce currents in a moving conductive fluid, which in turn polarises the fluid and reciprocally changes the magnetic field itself. The behaviour of a continuous plasma is governed by a combination of Maxwell's equations of electromagnetism, and Navier-Stokes equations of fluid mechanics. A derivation of the fundamental MHD equations is given in Priest [2014, §2].

Hannes Alfvén was awarded the Nobel Prize in Physics in 1970 for his pioneering work [Alfvén, 1942] on the field of MHD. There are various types of MHD, such as resistive, Hall, and two-fluid MHD. However, in this thesis, and subsequently, this section, ideal MHD is the primary focus. The typical governing MHD equations are the continuity, momentum, energy, and induction equations, which are given by:

$$\frac{\partial \rho}{\partial t} + \nabla \cdot (\mathbf{v}\rho) = 0, \tag{1.1}$$

$$\frac{\partial}{\partial t}(\rho \mathbf{v}) + \nabla \cdot (\mathbf{v}\rho\mathbf{v} - \mathbf{B}\mathbf{B}) + \nabla \mathrm{p_{tot}} = 0, \tag{1.2}$$

$$\frac{\partial e}{\partial t} + \nabla \cdot (\mathbf{v}\mathrm{e} - \mathbf{B}\mathbf{B} \cdot \mathbf{v} + \mathbf{v}\mathrm{p_{tot}}) = \nabla \cdot (\mathbf{B} \times \eta \mathbf{J}), \tag{1.3}$$

$$\frac{\partial \mathbf{B}}{\partial t} + \nabla \cdot (\mathbf{v}\mathbf{B} - \mathbf{B}\mathbf{v}) = \nabla \times (\eta \mathbf{J}), \tag{1.4}$$

where

$$p = (\gamma - 1)\left(e - \frac{\rho \mathbf{v}^2}{2} - \frac{\mathbf{B}^2}{2}\right), \tag{1.5}$$

$$p_{tot} = p + \frac{\mathbf{B}^2}{2}, \tag{1.6}$$

and

$$\nabla \times \mathbf{B} = \mu_0 \left(\mathbf{J} + \epsilon_0 \frac{\partial \mathbf{E}}{\partial t} \right). \tag{1.7}$$

The plasma mass density is given as ρ, $\mathbf{v}$ is the velocity vector, e is the internal energy density, $\mathbf{B}$ is the magnetic field vector, p_{tot} is the total pressure (magnetic plus thermal, p), and γ is the adiabatic index. $\mathbf{J}$ is the current density and the magnetic diffusivity is η. The resistive terms are not considered in this thesis due to ideal MHD being studied, *i.e.* $\eta = 0$. Subsequently, the are no source terms on the RHS of the equations. μ_0 and ϵ_0 are permeability and permittivity of free space, respectively whereas $\mathbf{E}$ is the electric field. From Maxwell's equations we also have:

$$\nabla \cdot \mathbf{B} = 0, \tag{1.8}$$

and

$$\nabla \cdot \mathbf{E} = \frac{\sigma}{\epsilon_0}, \tag{1.9}$$

where σ is the electric charge density.

1.2.1 Dimensionless Parameters

The *sonic Mach number* measures the flow speed, u relative to the sound speed, $c_S = (\gamma p/\rho)^{1/2}$, and is given by:

$$M_c = \frac{u}{c_S}. \tag{1.10}$$

Similarly, *the Alfvén Mach number* is expressed as:

$$M_A = \frac{u}{c_A}, \tag{1.11}$$

where the Alfvén speed is, $c_A = B_0/\left(\mu\rho\right)^{1/2}$, and μ is the magnetic permeability. M_A gives the relative magnitude of the flow speed with respect to the Alfvén speed.

The *plasma beta*, β is the measure of thermal pressure against magnetic pres-

sure, such that:

$$\beta = \frac{2\mu p}{B_0^2}. \tag{1.12}$$

If $\beta \ll 1$, then the magnetic pressure dominates the plasma, and we have a 'low-β' plasma. The plasma dominates in the photosphere, giving a 'high β' value, but as the plasma beta rapidly decreases with altitude above the solar surface, the magnetic field dominates in the low corona ($\beta < 1$). It follows that $\beta = 1$ surface occurs somewhere in the low-chromosphere.

The *magnetic Reynolds number* in terms of a typical plasma speed, u length-scale, L and the diffusive term, η is:

$$R_m = \frac{Lu}{\eta}. \tag{1.13}$$

This is a measure of the coupling strength between the flow and magnetic field. $R_m \ll 1$, means the coupling is weak and the magnetic field diffuses through the plasma. However, if $R_m \gg 1$, the magnetic field is 'frozen-in' to the plasma. This expression becomes the *Lundquist number* when $u = c_A$. Large Lundquist numbers indicate a highly conducting plasma whereas low Lundquist numbers indicate a more resistive one. The Lundquist number becomes important for events such as magnetic reconnection.

The ratio of the inertial and viscous forces within a fluid, which is subject to relative internal movement due to different fluid velocities is given by the *Reynolds number*:

$$R_e = \frac{Lu}{\upsilon}, \tag{1.14}$$

where υ is the dynamic viscosity of the fluid. The Reynolds number is used to predict the velocity at which turbulence will occur.

1.2.2 Ideal MHD

Here, it is assumed that the diffusivity is infinitesimal, such that, the magnetic Reynolds number, $R_m \gg 1$ as $\eta = 0$ can be assumed. When $R_m \gg 1$, Alfvén's

frozen-flux theorem[1] is maintained, implying that magnetic field lines and magnetic flux are conserved for ideal plasma flows. Thirdly, the magnetic topology is conserved. That is, the magnetic field lines are free to move and bend, but if the magnetic field changes at one particular point, it is the same as if the magnetic field lines were to move with the plasma. Plasma is free to move along the field lines but perpendicular to the field lines, either the field lines are dragged with the plasma, or they push the plasma. Consequently, the magnetic flux velocity, $\mathbf{w}_\perp$ is equal to the plasma velocity perpendicular to the field lines, $\mathbf{v}_\perp$. The velocities are expressed through:

$$\mathbf{w}_\perp = \mathbf{v}_\perp = \frac{\mathbf{E} \times \mathbf{B}}{B^2}, \tag{1.15}$$

which can be obtained by taking the vector product of Ohm's law, $\mathbf{E} + \mathbf{v} \times \mathbf{B} = 0$ with $\mathbf{B}$. This result, along with the fact that the velocities match the field line velocity, $\mathbf{v}_\parallel$ follows from the result of the 'frozen-in' condition.

Magnetic Flux Tube Consideration

Magnetic flux tubes, along with current sheets are the two fundamental magnetic configurations. A current sheet is an electric current which is confined to a surface, such as the Heliospheric current sheet, as opposed to being contained within a volume of space. In the corona, current sheets have an aspect ratio of $\approx 10^5$ [Biskamp, 1997, page 130], and are treated as zero thickness structures as a result of simplifying assumptions made in ideal MHD. On the other hand, magnetic flux tubes are cylindrical, or tube-like, regions of space that contain a magnetic field. In the photosphere, examples of flux tubes include sunspots where a large flux tube permeates through the solar surface, and intense magnetic tubes, which are significantly smaller tubes and are concentrated along granular and supergranular boundaries. In the corona, the multitude of coronal loops present, along with solar prominences serve as examples of flux tubes. Spicules are an example of a chromospheric flux tube. A twisted flux tube is often referred to as a flux rope whilst a flux tube is considered to be isolated if the external magnetic field vanishes.

[1] *Alfvén's frozen flux theorem*: the magnetic flux moving through a curve with the plasma is conserved when the global $R_m \gg 1$.

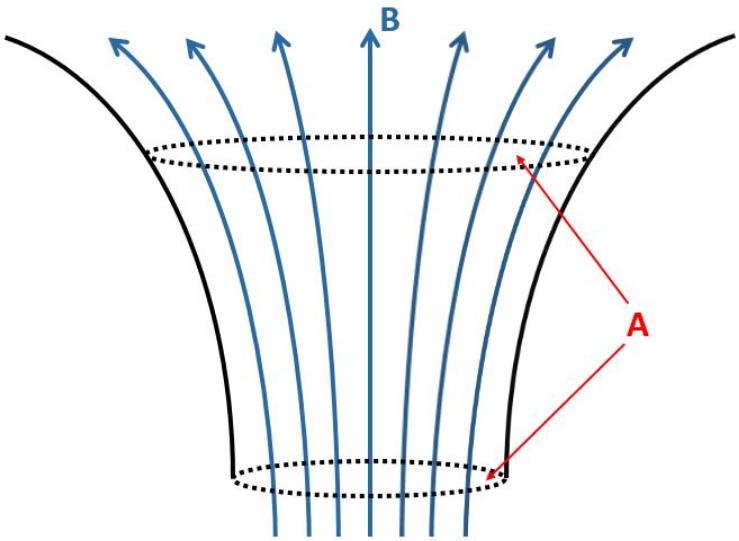

Figure 1.3: Schematic showing the magnetic strength remains constant along the length of a flux tube.

The magnetic strength, F_M of a flux tube is defined as the magnetic flux through a cross-section, S:

$$F_M = \int_S \mathbf{B} \cdot d\mathbf{S}, \tag{1.16}$$

where $d\mathbf{S}$ is always taken so that $F_M > 0$. The strength remains constant along the length of a flux tube due to $\nabla \cdot \mathbf{B} = 0$. The cross-section area of the tube, and the magnetic field contained within it may vary but the magnetic flux is always constant. In order for this to uphold when a flux tube narrows or widens, the mean field strength ($\bar{B}$) must increase or decrease, such that $F_M = \bar{B}A = constant$, where A is the cross-sectional area.

Another quirk is that the flux tube geometry alters the fundamental wave modes as they propagate along its length. For example, in a uniform flux tube, an Alfvén wave propagates at a uniform speed but as the flux tube widens or narrows, becomes denser or more rarefied, the Alfvén speed of the flux tube alters and so too does the Alfvén wave propagation. Also, the Alfvén waves may be absorbed and heat the plasma at critical radii where Alfvén or cusp resonances may occur.

Two modes of magnetoacoustic waves that may exist are kink, and sausage modes. Kink waves are oblique fast mode waves, which are guided by the structure and they displace the axis of the plasma structure. Sausage modes are also oblique fast mode waves that are guided by the plasma structure. However, they cause expansion and contraction of the plasma structure as they propagate along it. Unlike kink mode waves, they do not displace the axis of the structure. The amplitude of magnetoacoustic tube waves is radially dependent. A slow kink surface wave propagates with speed, $\frac{c_A}{\sqrt{2}}$, and a slow sausage surface wave travels at speeds slower than the tube speed,

$$c_T = \frac{c_S c_A}{\sqrt{c_S^2 + c_A^2}}.$$

Slow kink and sausage body waves travel at the tube speed but fast body or surface waves travel at the external sound speed.

1.2.3 Magnetic Waves

In Priest [2014] it is shown that the electric current density may be expressed as:

$$\mathbf{j} = \nabla \times \frac{\mathbf{B}}{\mu}. \tag{1.17}$$

Substituting this expression for the current density into the magnetic force, $\mathbf{j} \times \mathbf{B}$ yields:

$$\mathbf{j} \times \mathbf{B} = (\nabla \times \mathbf{B}) \times \frac{\mathbf{B}}{\mu} = \frac{(\mathbf{B} \cdot \nabla)\,\mathbf{B}}{\mu} - \nabla \left(\frac{B^2}{2\mu} \right). \tag{1.18}$$

From this it follows that the Lorentz force may be interpreted as the sum of the magnetic tension force (first term on RHS) and magnetic pressure force (second term on RHS). The tension, τ permits transverse waves to propagate along an elastic string with speed, $\sqrt{\tau/\rho}$, which is the Alfvén speed as $\tau = B_0^2/\mu$. The tension may be considered to allow waves to propagate in the direction of the magnetic field at the Alfvén speed. In coronal active regions this is typically 3000 $km\ s^{-1}$ whereas a typical photospheric Alfvén speed is 10 $km\ s^{-1}$.

Starting with the equations for continuity of mass, momentum, energy, and the induction equation, it is possible to derive the plane-wave solution. Consider small departures from the equilibrium such that, $\rho = \rho_0 + \rho_l$, $p = p_0 + p_l$, $\mathbf{v} = \mathbf{v_1}$, and $\mathbf{B} = \mathbf{B_0} + \mathbf{B_1}$. The aforementioned basic equations are linearised, and the products and squares of the perturbed quantities (subscript l) are neglected. From this, the plane-wave solution of a generalised wave equation for a disturbance velocity, $\mathbf{v_1}$ when a magnetic field is present is:

$$\omega^2 \mathbf{v_1} = c_S^2 \mathbf{k} \left(\mathbf{k} \cdot \mathbf{v_1}\right) + i \left(\gamma - 1\right) g \hat{\mathbf{z}} \left(\mathbf{k} \cdot \mathbf{v_1}\right) + ig\mathbf{k} v_{lz} - 2i\omega \boldsymbol{\Omega} \times \mathbf{v_1} + \left\{\mathbf{k} \times \left[\mathbf{k} \times \left(\mathbf{v_1} \times \mathbf{B_0}\right)\right]\right\} \times \frac{\mathbf{B_0}}{\mu\rho}, \quad (1.19)$$

where $\mathbf{k}$ is the wavenumber vector and ω is the frequency [Priest, 2014, §4.2]. If the magnetic field dominates the equilibrium such that quantities $g = \Omega = p = 0$, (where Ω is the angular velocity) and consequently $c_S = 0$, equation (1.19) may be reduced to yield:

$$\omega^2 \mathbf{v_1} = \left\{\mathbf{k} \times \left[\mathbf{v_1} \times \hat{\mathbf{B}}_\mathbf{0}\right]\right\} \times \hat{\mathbf{B}}_\mathbf{0} c_A^2, \quad (1.20)$$

where $\hat{\mathbf{B}}_\mathbf{0}$ is the unit vector along the magnetic field. This can be expressed in terms of θ_B, which is the angle between $\hat{\mathbf{B}}_\mathbf{0}$ and the direction of propagation, $\hat{\mathbf{k}}$:

$$\frac{\omega^2 \mathbf{v_1}}{c_A^2} = k^2 \cos^2\left(\theta_B\right) \mathbf{v_1} - \left(\mathbf{k} \cdot \mathbf{v_1}\right) k \cos\left(\theta_B\right) \hat{\mathbf{B}}_\mathbf{0} + \left[\left(\mathbf{k} \cdot \mathbf{v_1}\right) - k \cos\left(\theta_B\right) \left(\hat{\mathbf{B}}_\mathbf{0} \cdot \mathbf{v_1}\right)\right] \mathbf{k}. \quad (1.21)$$

For magnetically driven waves the following are true:

$$\mathbf{k} \cdot \mathbf{B_1} = 0, \quad \hat{\mathbf{B}}_\mathbf{0} \cdot \mathbf{v_1} = 0,$$

where $\mathbf{B_1}$ is the magnetic field disturbance. The first property indicates that magnetic waves are perpendicular to the propagation direction. The second property shows that the perturbed velocity is perpendicular to the magnetic field vector and is obtained by taking the scalar product of equation (1.20) with $\hat{\mathbf{B}}_\mathbf{0}$. Taking

the scalar product of (1.20) with $\mathbf{k}$ yields:

$$\left(\omega^2 - k^2 c_A^2\right)\left(\mathbf{k}\cdot\mathbf{v_1}\right) = 0, \tag{1.22}$$

giving two distinct solutions - torsional Alfvén waves and fast-mode waves.

Torsional Alfvén Waves

If the perturbation is incompressible, *i.e.* $(\nabla\mathbf{v_1} = 0)$, then $\mathbf{k}\cdot\mathbf{v_1} = 0$, and the square root of equation (1.20) yields:

$$\omega = \pm k c_A \cos\left(\theta_B\right), \tag{1.23}$$

where $c_A\cos\left(\theta_B\right)$ is the phase speed of the shear Alfvén wave. For propagation along the field line this is simply the Alfvén speed as $\theta_B = 0$. The positive and negative roots of equation (1.23) indicate propagation in the same or opposite direction as the magnetic field. It can be seen from equation (1.23) that the torsional Alfvén waves propagate most quickly along the field lines and not at all normal to them ($\theta_B = 90°$).

Assuming a magnetic field aligned along the z-axis, then $\omega = k_z c_A$, and the group speed is obtained by differentiating *w.r.t.* k_z. From this, it follows that energy is carried along the magnetic field at the Alfvén speed despite the fact the waves may travel at an inclination to the field line. The velocity perturbation of Alfvén waves is normal to the propagation due to the property, $\mathbf{k}\cdot\mathbf{v_1} = 0$, and as such the waves are considered transverse. In addition to this, there are no accompanying perturbations to the plasma density or pressure as the waves propagate.

The plane-wave solution for torsional Alfvén waves becomes:

$$-\omega\mathbf{B_1} = \left(\mathbf{k}\cdot\mathbf{B_1}\right)\mathbf{v_1} - \left(\mathbf{k}\cdot\mathbf{v_1}\right)\mathbf{B_0}. \tag{1.24}$$

This, in combination with equation (1.23) and $\mathbf{k} \cdot \mathbf{v_l} = 0$, implies that $\mathbf{v_l}$ and $\mathbf{B_l}$ are both in the same direction:

$$\mathbf{v_l} = \pm \frac{\mathbf{B_l}}{\sqrt{\mu\rho}}, \tag{1.25}$$

where the sign is dependent on the propagation being with or against the field line direction. As $\hat{\mathbf{B}}_\mathbf{0} \cdot \mathbf{v_l} = 0$, it can also be shown that the magnetic field perturbation is normal to the field line, $\mathbf{B_0} \cdot \mathbf{B_l} = 0$.

When the Alfvén wave amplitudes are large, the waves cease to propagate with constant profiles (wavelength and amplitude). Non-linear Alfvén waves display compressive motions, which lead to the waves interacting with themselves and steepening [Farahani et al., 2012].

Fast-Mode Waves

Fast-mode waves or compressional Alfvén waves yield the second solution to (1.22):

$$\omega = kc_A. \tag{1.26}$$

Their phase speed is the Alfvén speed regardless of the propagation angle relative to the magnetic field line. The group velocity is propagated isotropically and is expressed as:

$$\mathbf{v_g} = c_A \mathbf{k}. \tag{1.27}$$

Equation (1.20) and property, $\mathbf{k} \cdot \hat{\mathbf{B}}_\mathbf{0} = 0$ imply that $\mathbf{v_l}$ is normal to $\mathbf{B_0}$ and in the $(\mathbf{k}, \mathbf{B_0})$ plane. Thus, fast mode waves possess both longitudinal and transverse components and give rise to perturbations in the plasma density and pressure. When pressure gradients are present, the waves become fast magnetoacoustic or fast-mode waves.

Propagation along the magnetic field line, such that $\theta_B = 0$ leads to the fast-mode waves degenerating into shear Alfvén waves. The wave is now driven wholly by magnetic tension and the magnetic pressure plays no part. The result of this is that the wave does not produce compression.

1.3 Sound and Shock Waves

Sound is transmitted through liquids, gases, and plasma as compression (longitudinal) waves. Thus, unlike electromagnetic waves, they require a medium in which they can propagate. In solids, sound can travel as both longitudinal and transverse waves. The compression waves generate pressure perturbations from the equilibrium, creating regions of compression and rarefaction. On the other hand, transverse sound waves in solids are waves of alternating shear stress normal to the propagation direction. In longitudinal waves, the alternation between regions of compression and rarefaction generate pressure gradients in the form of a restoring force, which tries to restore the original equilibrium within the medium of propagation. In a uniform medium, the waves travel at a constant speed, c_S in all directions.

The main role of sound waves is to transport energy away from the source, however, their amplitude is generally small, such that they only slightly perturb the ambient medium around them. In the case that their amplitude is large, they may steepen and form into shock waves. An example of this is the sonic boom as an aircraft accelerates beyond the sound speed and becomes supersonic.

1.3.1 Sound Waves

The disturbance velocity, $\mathbf{v_1}$ can be expressed as:

$$\omega^2 \mathbf{v_1} = c_S^2 \mathbf{k} \left(\mathbf{k} \cdot \mathbf{v_1} \right), \tag{1.28}$$

when the only pressure gradient present is the restoring force. Taking the scalar product with $\mathbf{k}$ yields:

$$\omega^2 = k^2 c_S^2, \tag{1.29}$$

when the assumption $\mathbf{k} \cdot \mathbf{v_1} \neq 0$ is valid. Following from this, the dispersion relation for sound waves is:

$$\omega = \pm k c_S. \tag{1.30}$$

Thus, acoustic waves propagate at a phase speed ($\mathbf{v_p} = \omega/k$) that is equal to the sound speed and group speed ($d\omega/dk$), $\mathbf{v_g} = c_S$ in all directions $\pm\mathbf{k}$. In the solar atmosphere, the sound speed ($c_S = \sqrt{\gamma p/\rho}$) varies from $\approx 10\,km\,s^{-1}$ in the photosphere to $\approx 200\,km\,s^{-1}$ in the corona. The prerequisite that $\mathbf{k} \cdot \mathbf{v_l}$ does not vanish suggests that sound waves owe their existence to the fact that the plasma is compressible.

1.3.2 Shocks

The Sun is highly dynamic, and the globally present motions often lead to the formation of shocks. One example is the preceding Type-II radio burst that is associated with coronal mass ejections,[1] which contain large-scale prominence eruptions. Another example is magnetic reconnection and the formation of magnetic shock waves. If two distinct magnetic flux structures interact with each other, or new flux emerges from beneath the photosphere, the reconnection events invariably generate shock waves of magnetic origin. These are examples of large-scale shocks but small-scale occurrences exist which are likely due to spicules, surges, and granular motion in the photosphere.

Hydrodynamic Shocks

The relationship between the states either side of a hydrodynamic shock in a 1-D fluid can be described by the Rankine-Hugoniot jump conditions. The conditions are named after Scottish physicist and engineer, William John Macquorn Rankine [Rankine, 1859], and French engineer Pierre Henri Hugoniot [Hugoniot, 1889]. The conditions are often written as:

$$\rho_1 v_1 = \rho_2 v_2, \tag{1.31}$$

$$p_1 + \rho_1 v_1^2 = p_2 + \rho_2 v_2^2, \tag{1.32}$$

[1] "The first evidence of shock acceleration in the solar corona came from radio Type-II bursts, which were identified as shock structures from imaging observations of their outward motion" - Aschwanden [2005, p.512]

and

$$p_1 v_1 + \left(\rho_1 e_1 + \frac{1}{2}\rho_1 v_1^2\right) v_1 = p_2 v_2 + \left(\rho_2 e_2 + \frac{1}{2}\rho_2 v_2^2\right) v_2, \tag{1.33}$$

for an ideal gas. The subscripts 1 and 2 denote the pre- and post-shock quantities, respectively.

The first equation (1.31) arises from the conservation of mass and gives the mass crossing a unit area per unit time. For the second equation (1.32), the term $(\rho v)v$ yields the transport rate of momentum across a unit surface area, and p is the force acting upon that area. In condition (1.33), the second and fourth terms represent the internal and kinetic energy transport rates. The rate at which the gas pressure enacts work is given by pv.

It is shown in Priest [2014, §5.2] that the jump conditions (1.31) - (1.33) can be expressed through the sonic Mach number as:

$$\frac{\rho_2}{\rho_1} = \frac{(\gamma+1)\, M_{c1}^2}{2 + (\gamma-1)\, M_{c1}^2}, \tag{1.34}$$

$$\frac{v_2}{v_1} = \frac{2 + (\gamma-1)\, M_{c1}^2}{(\gamma+1)\, M_{c1}^2}, \tag{1.35}$$

and

$$\frac{p_2}{p_1} = \frac{2\gamma M_{c1}^2 - (\gamma-1)}{\gamma+1}. \tag{1.36}$$

This concludes the fundamental material. In the following sections, work on the interaction between Alfvén waves and pre-existing plasma flows within various structures is presented. In §2 the interaction of an Alfvénic pulse and classical shock is described within a sunspot flux tube. §3 investigates how Alfvén waves behave in the presence of a decelerating downflow in an intergranular lane. The final piece of work (§4) once again investigates the interaction of an Alfvénic pulse in the presence of a classical shock, though this time the study is the context of prominence formation. Finally, the work is summarised in the final chapter (§5).

Chapter 2

The Non-Linear Evolution of a Twist in a Uniform Magnetic Shocktube

The work presented in the following chapter has been published in the Astrophysical Journal [Williams et al., 2016].

2.1 Abstract

The interaction between a small twist and a horizontal chromospheric shocktube is investigated. The magnetic flux tube is modelled using 1.5-D magnetohydrodynamics (MHD). The presence of a supersonic yet sub-Alfvénic flow along the flux tube allows the Alfvénic pulse driven at the photospheric boundary to become trapped and amplified between the stationary shock front and photosphere. The amplification of the twist leads to the formation of slow and fast shocks. The pre-existing stationary shock is destabilised and pushed forward as it merges with the slow shock. The propagating fast shock extracts the kinetic energy of the flow and launches rapid twists of $10 - 15\ km\ s^{-1}$ upon each reflection. A cavity is formed between the slow and fast shocks where the flux tube becomes globally twisted within less than an hour. The resultant highly-twisted magnetic flux tube is similar to those prone to kink instabilities, which may be responsible

for solar eruptions. The generated torsional flux is calculated.

2.2 Introduction

Magnetic flux tubes are ubiquitous within the solar atmosphere. They are known as the building blocks that may form small or large scale structures. Flux tubes on different scales often exhibit mass flow. Examples include siphon flows in coronal loops [Orlando et al., 1995a,b], counterstreaming [Lin et al., 2003] and field-aligned flows within filament channels [Lin et al., 2005], spicules [De Pontieu et al., 2004; Hollweg et al., 1982; Scullion et al., 2011; Zaqarashvili and Erdélyi, 2009], Evershed flows within sunspots [Montesinos and Thomas, 1997; Plaza et al., 1997]. In addition, non-thermal broadenings have been observed within the chromosphere [Beckers, 1968, 1972; Jess et al., 2009, 2015; Pishkalo, 1994]. These non-thermal broadenings are usually interpreted as Alfvén waves and have been considered as a possible mechanism responsible for Type-I spicule formation [Erdélyi and James, 2004; Hollweg, 1992; Hollweg et al., 1982; James et al., 2003; Kudoh and Shibata, 1999; Sterling and Hollweg, 1988] though it is possible that other mechanisms such as leakage of p-mode oscillations along inclined field lines are responsible [De Pontieu et al., 2004]. For a review, see Sterling [2000].

Using *Hinode* De Pontieu et al. [2007] proposed the existence of Type-II spicules, which are more explosive than the classical, Type-I variety. De Pontieu et al. [2012] used the Swedish 1 m Solar Telescope to establish and quantify three types of motions within Type-II spicules: *i*) field aligned flows of $50-100\ km\ s^{-1}$ *ii*) swaying back and forth with speeds of $15-20\ km\ s^{-1}$ and *iii*) torsional motions between $25-30\ km\ s^{-1}$. Type-II spicules are often associated with regions of rapid blue-shift and red-shift. The launch of *IRIS* (Interface Region Imaging Spectrograph) has led to observations of small-scale twists that propagate along these structures. The typical amplitudes are $10-30\ km\ s^{-1}$ and the duration is less than a minute [De Pontieu et al., 2014].

Recently, high-resolution observations from Crisp Imaging Spectro-Polarimeter

[Wedemeyer-Böhm et al., 2012] detected a number of small-scale chromospheric swirls. It was also shown numerically by (non) convection simulations [Fedun et al., 2011; Wedemeyer-Böhm et al., 2012] that granular-driven magnetic vortices in the photosphere [Bonet et al., 2008, 2010; Brandt et al., 1988] are capable of driving such motions up to the transition region and further into the lower corona, which provides an alternative method for transmitting energy. Li et al. [2012] witness flow channels within a solar tornado that rise and fall along curved trajectories and suggest that the motions are along helical magnetic field lines. They also claim that flows and density waves may propagate along the magnetic field lines within the solar tornado. In intergranular lanes, similar motions have been seen in the form of magnetic whirlpools of downflowing plasma [Bonet et al., 2008, 2010]. However, it is also worth mentioning that Panasenco et al. [2014] show rapid swirling motions and solar tornadoes may be an illusion caused by 2D projection effects at the solar limb.

Work by Vranjes [2014] has shown that partial ionisation of the chromosphere can lead to Alfvén waves being severely damped between the photosphere and corona. Studies by James et al. [2003] and Erdélyi and James [2004] have shown that partial ionisation of the atmosphere may aid Alfvén waves with the heating and formation of chromospheric structures such as spicules.

MHD instabilities in the solar atmosphere play an important role in the amplification of perturbations, which may drastically alter the system. Taroyan [2008] discovered the possibility of a new MHD instability which is based on the interaction between an incompressible Alfvénic perturbation and a compressible plasma flow. The perturbations amplify due to over-reflection - a concept first investigated by Acheson [1976] in regards to the Kelvin-Helmholtz instability.

The Alfvén instability was investigated for siphon flows within asymmetric coronal loops and found that linear torsional perturbations driven at the footpoints are exponentially amplified [Taroyan, 2009]. Taroyan [2011] considered the Alfvén instability for smooth plasma flow within open and expanding flux tubes in the presence of gravity. The analysis was extended by Taroyan [2015] to include non-

isothermal flows, a body force term in the momentum equation, and a full energy equation.

The study of shock waves can be dated back to the 17^{th} century with Sir Isaac Newton's *Principia* in 1687. Poisson's memoirs in 1808 laid the foundations for the first shock wave theory and later work by Laplace [1816] and subsequently Rankine [1859] improved Newton's theory by assuming that sound is an adiabatic process. In Hugoniot's (1889) memoirs, the equation which relates the internal energy to the kinetic energy of a thermodynamic system is introduced. Currently, shocks are a topical study in astrophysics and the Sun. Orlando et al. [1995b] investigate the physical conditions within coronal loops that allow the formation of isothermal and adiabatic shocks for shocked critical solutions and shocked supersonic solutions when a siphon flow is present. Shocks appear in abundance in the solar system with shock waves in the solar atmosphere [Centeno et al., 2009; Hollweg, 1992; Ryutova and Tarbell, 2003], CMEs [Fainshtein and Egorov, 2015; Lugaz et al., 2015; Magdalenić et al., 2014], interplanetary shocks within the solar wind [Grygorov et al., 2014] and at the solar wind termination shock [Baranov et al., 1996].

High resolution observations have shown that the Evershed flow is mainly concentrated into the dark penumbral filaments where the magnetic field is nearly horizontal [Title et al., 1992]. The flow speed can reach up to 20 $km\ s^{-1}$ or more in individual filaments. In some filaments the flow is observed to slow abruptly at a location of enhanced emission, which is strongly suggestive of a standing shock in supersonic siphon flow [Borrero et al., 2005; Georgakilas et al., 2003; Maltby, 1975]. However, none of these studies have focused on the interaction between a standing shock and an Alfvén wave, until now.

The present study is the first, pure numerical investigation that confirms the existence of the Alfvén instability. The study extends the analysis of the phenomenon to the non-linear regime. The interaction of a small Alfvénic twist with a classical gas-dynamic shock; the amplification of the twist and consequences of non-linearity; and the role the Alfvén wave plays in energy transfer are anal-

ysed. In the next section the model is presented. This includes the geometry used, choice of boundary conditions, replication of an Alfvén wave, setting up a stationary shock, and normalisation. In section 2.6, the conditions required for the Alfvén instability and thus the amplification of an Alfvén wave are discussed. The model results are presented in section 2.7 and discussed in sections 2.8 and 2.9.

2.3 The LCPFCT Flux Tube Model

Initially, the model was constructed using the FORTRAN library, LCPFCT - an FCT (flux corrected transport) algorithm updated from the previous version, ETBFCT. FCT algorithms are second order, conservative shock-capturing schemes that solve Euler, or other hyperbolic equations. FCT algorithms initially implement a transport stage, which is then followed by a corrective, anti-diffusion stage. Both stages are conservative and their interaction allows FCT schemes to resolve strong gradients such as shocks without artificial ripples arising [Boris and Book, 1973].

For this reason, and due to test problem 2 of LCPFCT (§8.2 Boris et al., 1993) having similar system geometry to that desired it was initially thought that LCPFCT would be ideally suited to handle the problem at hand. In this test problem, a gas flowing inside a tube is modelled in 1-D Cartesian coordinates. A shock is generated at some user-defined grid-point with the discontinuity described by the Rankine-Hugoniot jump conditions. The system parameters are solved for a number of iterations/time-steps using the LCPFCT subroutine which solves continuity equations of the following form:

$$\frac{\partial \rho}{\partial t} = -\frac{1}{r^{\alpha-1}}\frac{\partial}{\partial r}(r^{\alpha-1}\rho v) - \frac{1}{r^{\alpha-1}}\frac{\partial}{\partial r}(r^{\alpha-1}D_1) + C_2\frac{\partial D_2}{\partial r} + D_3, \qquad (2.1)$$

where ρ is the interested quantity. Additional source terms are added to the equation through the terms D_1, D_2, and D_3 with C_2 being a constant. The coordinate system is determined through α. If $\alpha = 1$ then Cartesian coordinates are used, $\alpha = 2$ corresponds to cylindrical coordinates, and $\alpha = 3$ is for spherical

geometry. User specified geometry can be chosen if α is set to 4.

In the test problem, only three equations are solved: mass conservation, momentum in the direction of flow, and energy. A constant longitudinal magnetic field was added to the system along with a transverse B-field that is initially set to zero. A fourth continuity equation, which describes the transverse momentum of the system is present in LCPFCT but remains unused in test problem 2. The transverse momentum equation can be included by adding a source term to the equation that describes an Alfvén wave. In this way, the transverse velocity, v_θ no longer remains zero during the simulation. This leads to the 1.5-D approximation as velocity now exists across the flux tube but it is assumed to be constant in that direction. The magnetic induction equation is added via a call to the LCPFCT library so that B_θ is the interested quantity, ρ of equation (2.1) and the appropriate source terms are included via D_1, D_2, and/or D_3.

For the modelled shocktube, the flow along the flux tube is sub-Alfvénic yet supersonic prior to interaction with the shock, at which point, the flow also becomes subsonic. These flow characteristics ensure that the flow-propagated torsional Alfvén wave is partially reflected and transmitted by the shock. A linear, Cartesian coordinate grid is used of 2000 cells with the shock positioned at cell 1000. The torsional Alfvén wave is generated at the photospheric level.

2.3.1 LCPFCT Model Equations

The five basic MHD equations that describe the system within the flux tube are those of mass conservation, longitudinal & transverse momentum, energy, and induction are shown here:

$$\frac{\partial}{\partial t}\left(\frac{\rho}{B_x}\right) = -\frac{\partial}{\partial x}\left(\frac{\rho}{B_x}v_x\right), \tag{2.2}$$

$$\frac{\partial}{\partial t}\left(\frac{\rho v_x}{B_x}\right) = -\frac{\partial}{\partial x}\left(\frac{\rho v_x}{B_x}v_x\right) - \frac{1}{B_x}\nabla(p), \tag{2.3}$$

$$\frac{\partial}{\partial t}\left(\frac{\rho v_y}{B_x}\right) = -\frac{\partial}{\partial x}\left(\frac{\rho v_y}{B_x} v_x\right) + \frac{1}{\mu_0}\frac{\partial B_y}{\partial x}, \tag{2.4}$$

$$\frac{\partial}{\partial t}\left(\frac{p}{B_x}\right) = -\frac{\partial}{\partial x}\left(\frac{p}{B_x} v_x\right) - (\gamma - 1) p \frac{\partial}{\partial x}\left(\frac{v_x}{B_x}\right), \tag{2.5}$$

$$\frac{\partial}{\partial t}\left(\frac{B_y}{B_x}\right) = -\frac{\partial}{\partial x}\left(\frac{B_y}{B_x} v_x\right) + \frac{\partial v_y}{\partial x}, \tag{2.6}$$

and

$$e = \frac{p}{(\gamma - 1)} + \frac{1}{2}\rho v_x^2 + \frac{1}{2}B_x^2, \tag{2.7}$$

The quantities ρ, v, e, p, and B, represent the plasma density, velocity, energy, pressure, and magnetic field. The system is assumed to be adiabatic, with an index $\gamma = {}^5/_3$. The subscripts x and y denote the longitudinal and transverse components of that quantity. The temperature of the plasma inside the flux tube is calculated by:

$$T = \frac{p}{\rho R} \ \ [K]\,, \tag{2.8}$$

where R is the molar gas constant.

Torsional Alfvén waves are generated by adding a perturbation force to the base of the flux tube that propagates in the x-direction. This is done by adding a half sinusoidal term to the transverse momentum equation:

$$F(t) = \begin{cases} \frac{A}{B_x}\rho \sin(\omega t) \cos\left(\frac{(x - x_0)\pi}{2x_h}\right) & \text{if } 0 \leq t \leq 57 \text{ s and } \mid x - x_0 \mid \leq x_h \\ 0 & \text{otherwise} \end{cases}, \tag{2.9}$$

where A is the amplitude, x is the current location within the region that a force is produced, x_0 is the peak location and x_h is the total height of the perturbation. The cosine function generates a smoothing profile of the perturbation in the modelled shocktube.

The state of the system parameters either side of the standing shock are de-

scribed by the following Rankine-Hugoniot jump conditions:

$$v_2 = v_1 \frac{(\gamma - 1)\frac{2}{M^2}}{\gamma + 1}, \tag{2.10}$$

$$\rho_2 = \rho_1 \frac{v_1}{v_2}, \tag{2.11}$$

$$p_2 = p_1 - \rho_2 v_2^2 + \rho_1 v_1^2, \tag{2.12}$$

$$e_1 = \frac{p_1}{\gamma - 1} + \frac{1}{2}\rho_1 v_1^2 + \frac{1}{2}B_1^2, \tag{2.13}$$

$$e_2 = \frac{p_2}{\gamma - 1} + \frac{1}{2}\rho_2 v_2^2 + \frac{1}{2}B_2^2, \tag{2.14}$$

where

$$v_1 = M c_{s1}, \tag{2.15}$$

and

$$c_{s1} = \sqrt{\gamma \frac{p_1}{\rho_1}}. \tag{2.16}$$

Here, c_{s1} is the sound speed, M is the Mach number, subscripts 1, and 2 represent the non-shocked and shocked plasma quantities, respectively.

2.3.2 Gibbs' Oscillations

In this section the numerical flaws introduced from the complexity of having a sharp shock and a smooth pulse propagating in the presence of a continuous flow are highlighted. It is worth mentioning that as the magnetic field in the longitudinal direction is constant, the Alfvén speed can be used to indicate the density jump caused by the Rankine-Hugoniot conditions.

A prominent issue with this method is Gibbs' phenomenon (Figure 2.1). This

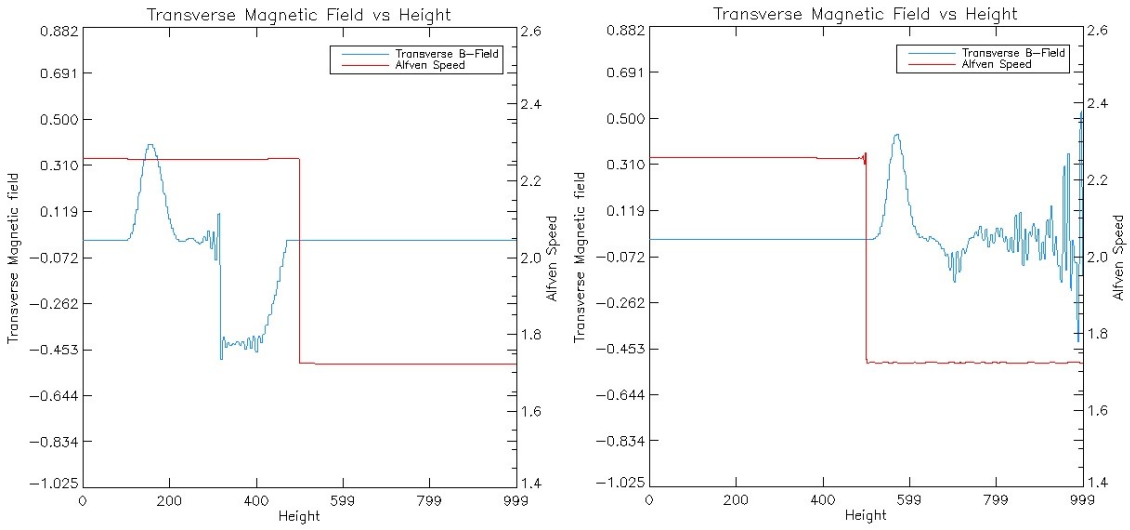

Figure 2.1: *left* is the shocktube prior to the Alfvén wave - shock interaction and *right* is the system post-interaction. The sharp decrease in Alfvén speed highlights the shock location. Gibbs' oscillations can be seen in the transverse pulse and Alfvén speed.

is where spurious oscillations are seen to arise in the presence of a jump condition. These oscillations are caused by the method continuously overshooting and undershooting around the actual solution [Foster and Richards, 1991]. This phenomenon can be eradicated from the LCPFCT model by altering the mask value.

Shock Smoothing

In order to control the Gibbs' phenomena seen in Figure (2.1), a mask value not equal to unity must be used to allow for minimal residual diffusion. This mask determines the anti-diffusion coefficient used by the FCT scheme. However, the mask must be decreased to ≈ 0.925 for LCPFCT in order to eliminate Gibbs' phenomena from the model, which is considerably lower than the typical mask of 0.98 - 1.0 [Book et al., 1991].

Within LCPFCT there is a mask that controls the amount of anti-diffusion ap-

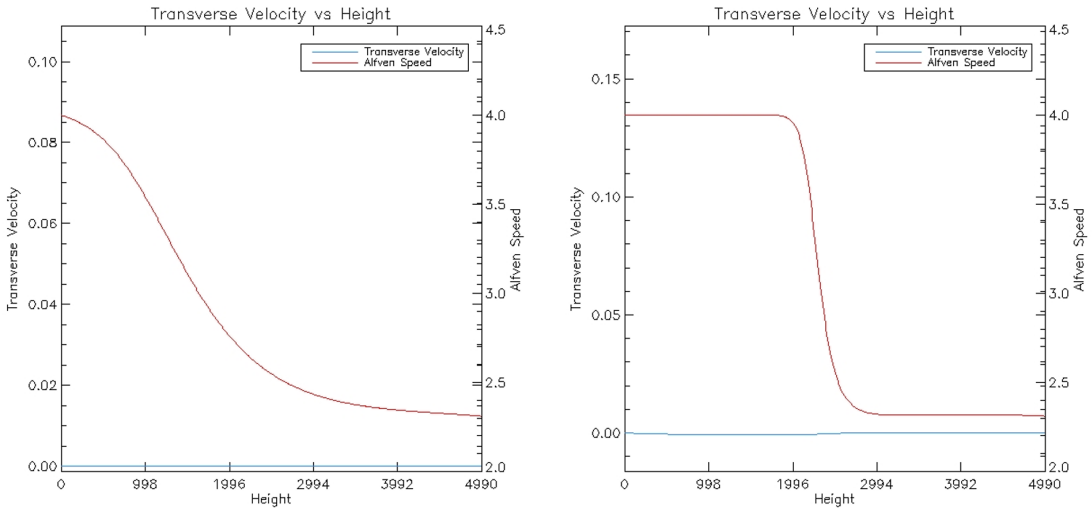

Figure 2.2: The two images show the final diffuse state of the shock location when the mask is set to 0 (*left*) and 0.8 (*right*). The default value for the mask is 1, which is used in Figure (2.1).

plied in the corrective stage of the algorithm. If a mask value below 0.925 is employed, then the shock smooths by diffusion (Figure 2.2). A small perturbation can be seen to propagate from the shock through the plasma upstream of the shock (Figure 2.3), and eventually out of the modelled shocktube. This happens at any mask value selected that is not unity, or close to unity. It is the result of the shock boundary altering in order to allow numerical stability. The lower the value of the anti-diffusion mask selected, the more exaggerated this becomes until eventually, the shock smooths into a slope when anti-diffusion is turned off (Figure 2.2).

2.3.3 Results and Analysis

The Alfvén wave - shock interaction occurs as expected for the system with the behaviour matching results from Taroyan [2008]. When the flow speed is supersonic and super-Alfvénic, two waves are formed which travel at different velocities. No reflection of the waves occur as they pass the shock (Figure 2.1). When the flow

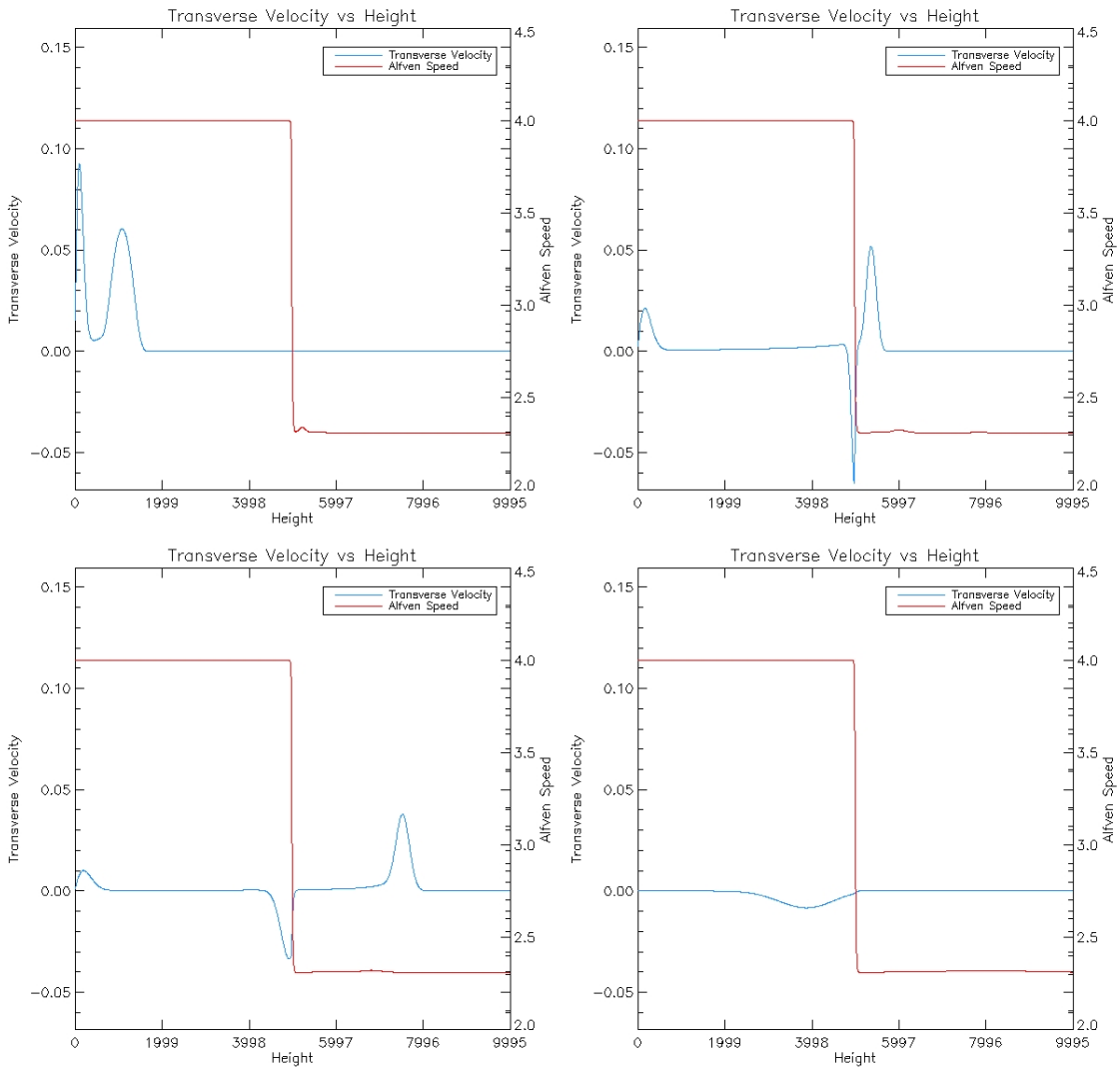

Figure 2.3: Temporal evolution of the torsional Alfvén wave with the simulation time in arbitrary units being: 6 (*top left*), 26 (*top right*), 46 (*bottom left*), and 300 (*bottom right*). The torsional wave is carried by the flow with partial reflection and transmission of the wave occurring at the shock location.

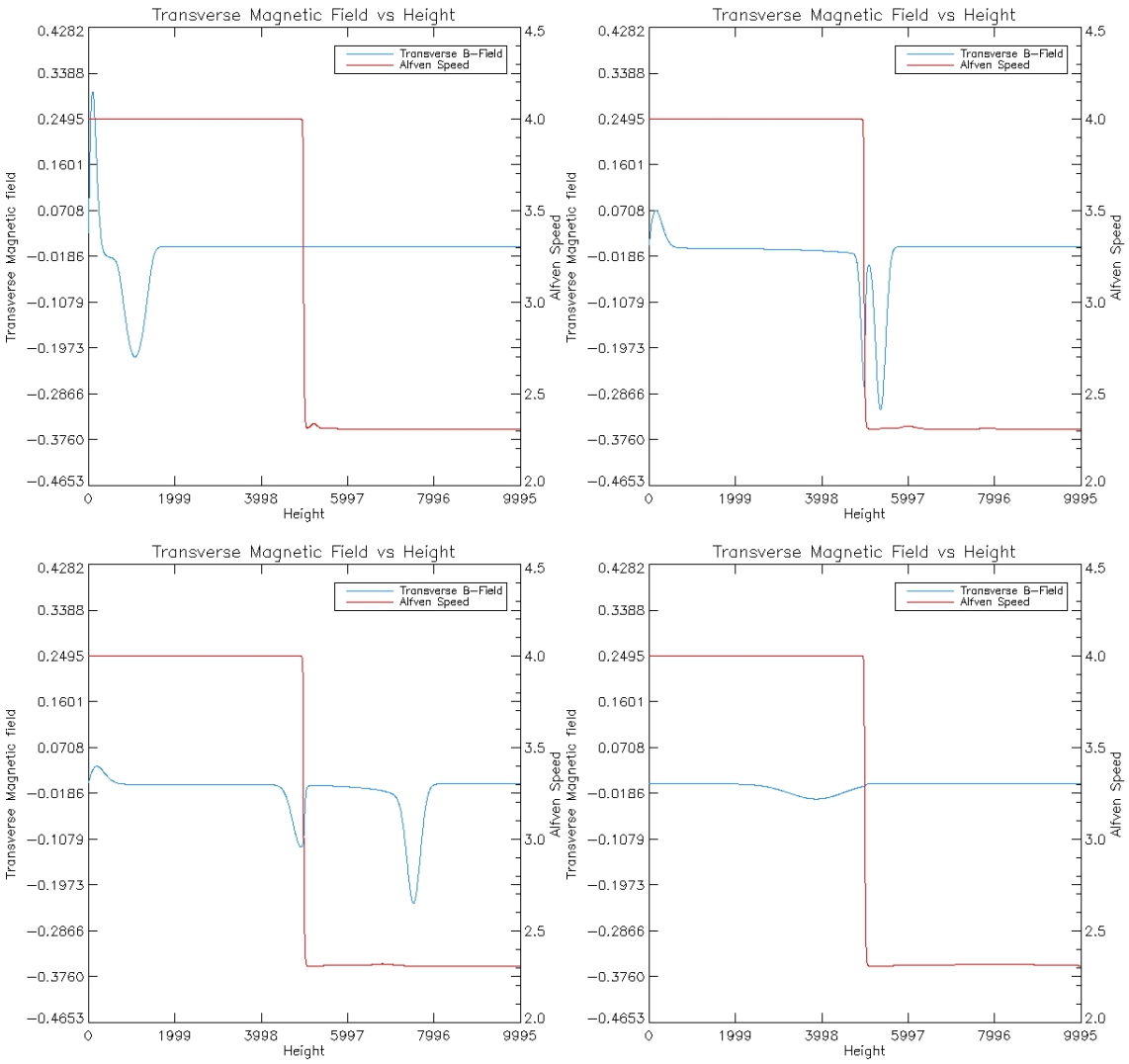

Figure 2.4: Transverse magnetic field of the flux tube with the same arbitrary times as Figure (2.3). The effect that diffusion has on the magnetic perturbation is evident, with the reflected perturbation merely diffusing into the background rather than propagating towards the left boundary.

is supersonic but sub-Alfvénic, there is only a single wave produced. This wave is partially transmitted and reflected by the shock (Figure 2.3). The generation of a single wave and it's partial reflection by the stationary shock is due to the relative magnitudes of the flow and Alfvén speeds. When the flow speed is sub-Alfvénic the wave is capable of propagating against the flow. This, in addition to the Alfvén driver launching waves in the $+x$ and $-x$-directions means that the $-x$ propagating wave does not get 'pushed' into propagating in the $+x$ direction, unlike when the flow is super-Alfvénic.

As can be seen in Figure (2.3), a smooth, torsional Alfvén wave is eventually generated from the model once Gibbs' phenomenon and the shock smoothing have been constrained. The Alfvén wave is propagated by the presence of the longitudinal flow and the shock splits the wave into reflected and transmitted components. However, the reflected wave is seen to diffuse across the numerical domain rather than propagate towards the flux tube base. Whilst the transmitted wave continues to propagate with the flow, its amplitude decreases and its distribution broadens. The behaviour of the reflected and transmitted waves is non-physical and not expected to occur in a uniform medium. This suggests that numerical diffusion is occurring for the transmitted wave as well. This can also be seen in the transverse magnetic field (Figure 2.4).

The factor, A in eq. (2.9) has a stabilising effect on the system. If the amplitude is > 0.01, the torsional wave generates spurious perturbations in density around the shock. This is most likely due to the relative size of v_y compared to v_x causing non-linear behaviour despite the fact that non-linear coupling has not been incorporated into the system equations.

2.3.4 Summary of LCPFCT Model

In this study, an Alfvén wave is driven from the left hand side of the flux tube and into the modelled shocktube. It is propagated by the presence of a flow until it reaches the shock generated by the Rankine-Hugoniot conditions. Here, the torsional wave is partially transmitted and reflected. Unfortunately, due

to the complexity of the problem at hand, the LCPFCT scheme is unable to accurately resolve the wave evolution. When anti-diffusion is applied with a mask of 1, the model becomes unstable with Gibbs‘ oscillations occurring prior to the launched Alfvén wave interacting with the stationary shock. After the wave has interacted with the shock, the shock also exhibits behaviour of these spurious oscillations. However, when anti-diffusion is reduced by taking a mask value less than unity, these oscillations for the shock are reduced but the Alfvén wave amplitude decreases upon generation and furthermore as it propagates along the flux tube. After the wave interacts with the shock, the transmitted component continues to propagate and the decline in amplitude and peak broadening persist. The reflected component of the wave appears to propagate much slower towards the $x = 0$ boundary and the peak broadening is more prominent. Due to no physical terms within equations (2.2) - (2.9) being able to explain this peak broadening, *i.e.* no source terms incorporating diffusion, this broadening must be a numerical artefact and the diffusion seen is not a consequence of the mask value of the anti-diffusion selected. This is because the amplitudes of the waves are seen to decrease and the peaks broaden if the mask is set to unity (default) or 0. For this reason, it was deemed that LCPFCT is not suitable to solve the problem at hand and a more robust scheme is required to resolve the linear model and advance into the non-linear regime. Whilst LCPFCT remains unsuitable to resolve the steep shocks produced in this model, it is still suitable for use when studying the coupling of small amplitude waves with smooth plasma flows. This is because the large gradients in the derivatives will not be present in such problems and thus the numerical solvers should be able to resolve the system accurately without the introduction of spurious oscillations.

2.4 The Versatile Advection Code

We now move away from the problematic LCPFCT scheme and utilise the Versatile Advection Code (VAC; Tóth, 1997). Several numerical models, which investigate Alfvén wave propagation inside a magnetic flux tube have employed VAC with success (Erdélyi and James, 2004; James et al., 2003; Kudoh and Shibata, 1999; and so on). VAC has several solvers for the user to choose from,

including two FCT schemes. These are ETBFCT and YDFCT. YDFCT is faster than ETBFCT as it can have a Courant number[1] up to 0.8 compared to 0.4 for ETBFCT. However, this does mean the YDFCT solution is less accurate than that obtained by ETBFCT. In addition to the FCT solvers, VAC also has several TVD (Total Variation Diminishing) and CD (Central Difference) schemes[2]. Unlike FCT schemes, which have been shown to yield regions of overshoots and undershoots around the exact solution, TVD schemes are designed to avoid these oscillations and have proved useful in computational fluid dynamics (CFD) and time-dependant gas dynamic systems [Versteeg and Malalasekera, 2007]. However, TVD, and other non-oscillatory schemes are limited to first order accuracy, whereas TVDLF, TVD-MUSCL, CD, and FCT are second-order accurate. That said, these schemes are not limited when resolving a shock as shocks must be solved with first-order accuracy. CD4 and RK4 are fourth-order accurate. CD (second order and fourth order) fall under the finite difference category, as do forward, and backward differencing. In general, finite difference for the derivative of a function $f'(x)$ can be described by:

$$f'(x) = \frac{f(x+u) - f(x-w)}{u+w}, \tag{2.17}$$

where h is the separation between two adjacent points in $f'(x)$. For forward differencing $u = h$ and $w = 0$, backward differencing $u = 0$ and $w = h$, and for central differencing $u = w = h$. The formula for CD4 is achieved by combining and solving 4 Taylor series to yield:

$$f'(x) = \frac{-f(x+2h) + 8f(x+h) - 8f(x-h) + f(x-2h)}{12h}. \tag{2.18}$$

[1] In 1-D, the Courant number is defined as $C = v\Delta x\Delta t$. Here, v is the characteristic wave speed of the system, Δx is the distance between two adjacent gridpoints, and Δt is the time-step.

[2] VAC also includes numerical schemes such as Runge-Kutta (RK), Poisson, and MacCormack. However, these are often used alongside the TVD, FCT, and CD schemes.

In general, the VAC schemes solve partial differential equations of the form:

$$\frac{\partial w}{\partial t} = \frac{\partial}{\partial x} F_i(w) + S(w) = R(w), \tag{2.19}$$

where w is a vector containing the flow variables, and F_i is the flux of each w vector in the directions i. S denotes the source terms and fluxes that are not included in F_i and R is the flux and source terms together. For methods that are designed to handle 1-D problems, source and dimensional splitting may be incorporated in order for multi-dimensional problems to be solved accurately. In the event that one of the w vectors has no temporal dependency, i.e. are time independent, then the 'nul' option may be used instead of the numerical solver. This means the vector is not advanced for each time-step, and can shorten the run-time for VAC. For example, in 1-D the magnetic field is not advected so that $\nabla \cdot \mathbf{B} = 0$ is maintained numerically, so B_i may be set to the 'nul' option.

There are several physics options for the user to choose from in the VAC library; these are the transport equation, hydrodynamics, adiabatic hydrodynamics, MHD, as well as isothermal and polytropic MHD. For this study, the MHD equations are used and they have the general form:

$$\frac{\partial \rho}{\partial t} + \nabla \cdot (\mathbf{v}\rho) = 0, \tag{2.20}$$

$$\frac{\partial}{\partial t}(\rho \mathbf{v}) + \nabla \cdot (\mathbf{v}\rho\mathbf{v} - \mathbf{B}\mathbf{B}) + \nabla \mathrm{p_{tot}} = -(\nabla \cdot \mathbf{B})\,\mathbf{B}, \tag{2.21}$$

$$\frac{\partial e}{\partial t} + \nabla \cdot (\mathbf{v}\mathrm{e} - \mathbf{B}\mathbf{B} \cdot \mathbf{v} + \mathbf{v}\mathrm{p_{tot}}) = -(\nabla \cdot \mathbf{B})\,\mathbf{B} \cdot \mathbf{v} + \nabla \cdot (\mathbf{B} \times \eta\mathbf{J}), \tag{2.22}$$

$$\frac{\partial \mathbf{B}}{\partial t} + \nabla \cdot (\mathbf{v}\mathbf{B} - \mathbf{B}\mathbf{v}) = -(\nabla \cdot \mathbf{B})\,\mathbf{v} - \nabla \times (\eta\mathbf{J}), \tag{2.23}$$

where

$$p = (\gamma - 1)\left(e - \frac{\rho\mathbf{v}^2}{2} - \frac{\mathbf{B}^2}{2}\right), \tag{2.24}$$

$$p_{tot} = p + \frac{\mathbf{B}^2}{2}, \tag{2.25}$$

and

$$\mathbf{J} = \nabla \times \mathbf{B}. \tag{2.26}$$

It is worth noting that the terms on the RHS of the above equations, which contain $\nabla \cdot \mathbf{B}$ are Powell's fix. These solve numerical problems related to the divergence of the magnetic field. However, for 1-D systems, this is not an issue.

In order to avoid the diffusive and oscillatory problems that occur with LCPFCT for the model, the robustness of the various solvers available in VAC were tested. The same geometry implemented by LCPFCT was used, that is, a stationary shock at an arbitrary grid location and an Alfvén wave driven from the base of the flux tube. Slab symmetry and the 1.5-D approximation were also incorporated.

It was found that for the geometry used, CD4, a 4^{th} order central differencing scheme coupled with a TVDLF (Total Variance Diminishing Lax-Friedrich) predictor step and a minmod limiter[1] yield the most stable system. This eliminates any spurious oscillations and spikes around the stationary shock location and only a small amount of diffusion is seen in the Alfvénic pulse - which remains a smooth variation throughout the simulation.

2.5 Numerical Model

The model presented in this chapter is a 1.5-D axisymmetric magnetic shock-tube, which was introduced by Hollweg et al. [1982] and subsequently employed by Kudoh and Shibata [1999]; Matsumoto and Shibata [2010]; Sterling and Hollweg [1988]; and others. It is discussed by Hollweg [1981] that a single field-line is modelled which resides close to but not on the axis of symmetry, such that for

[1]The minmod limiter is the default flux limiter in VAC. It is the most diffusive and often yields the most stable results. It only comes into play when sharp wave-fronts are present and it works by limiting the spatial derivatives of the PDE to realistic values.

typical cylindrical coordinates, $r \neq 0$ at any point. The equations used in these models may describe torsional and shear Alfvén waves in the non-linear regime depending on whether the chosen geometry is cylindrical or Cartesian (Priest, 2014, §4.3).

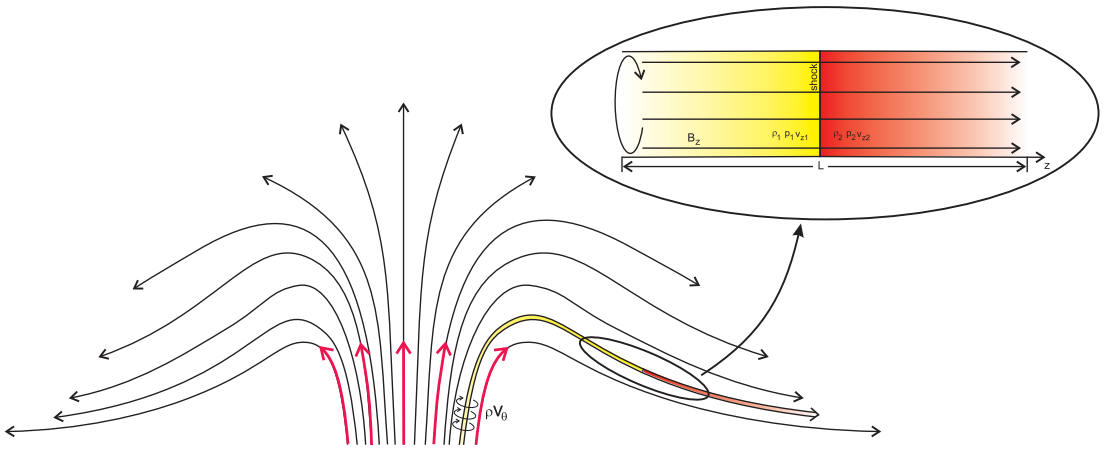

Figure 2.5: A schematic of the magnetic field above a sunspot region. A flow emanates from within a sunspot (red arrows) and propagates along the field lines (black lines). The encircled portion of the flux tube represents the region modelled in this study. In this region, the flow becomes supersonic and propagates from left to right along the magnetic field line, B_z. A stationary shock is situated in the centre of the modelled shocktube with subscripts 1 and 2 denoting the system variables upstream (yellow region) and downstream (red region) of the shock. The region either side of the shock are described by the Rankine-Hugoniot jump conditions (2.35) - (2.38) and result in the following inequalities: $\rho_1 < \rho_2$, $v_{z1} > v_{z2}$, $p_1 < p_2$, and $e_1 < e_2$. A driven boundary is implemented for ρv_θ at the left boundary and is denoted by the torsional arrows. All other boundary conditions are set to continuous for this study.

A uniform background magnetic field in the longitudinal direction, B_z which does not vary in space or time is defined. The magnetic field is highly inclined such that the field-line is virtually horizontal.

In the forthcoming analysis, θ denotes the azimuthal direction and as it is assumed that none of the quantities vary in the azimuthal direction, it follows that $\frac{\partial}{\partial \theta} = 0$. The model is generated using the MHD equations in VAC (Versatile

Advection Code), see *e.g.* Tóth [1997]. The numerical scheme used to resolve the system is CD4 (4^{th} order central differencing) with a TVDLF (Total Variance Diminishing Lax-Friedrich) predictor step and minmod limiter. The shocktube geometry can be seen in Figure (2.5).

2.5.1 Normalisation

Distance z is normalised with respect to the length L of the tube section under consideration. All other quantities are normalised with respect to the corresponding initial values in the upstream region which is denoted by the index, 1 (Figure 2.5). An initial plasma density, $\rho_1 = 5.26 \times 10^{-8}\ kg\ m^{-3}$ and sound speed, $c_{S1} = 10\ km\ s^{-1}$ are assumed. A background flow speed of $v_{z1} = 30\ km\ s^{-1}$, sonic Mach speed of $M_{c1} = 3$, and initial Alfvén speed of $c_{A1} = 38.9\ km\ s^{-1}$ are employed. These Alfvén speed and density values yield a constant magnetic field of $B_z = 100\ G$. The specific heats ratio, γ is taken as $\gamma = 1.2$ to represent the photosphere and low chromosphere where the shocktube is embedded. If the flux tube were in the corona then $\gamma = 5/3$ would represent a fully-ionised plasma. However, the effects of partial ionisation, such as in the lower solar atmosphere, can make γ as low as $\gamma \gtrsim 1$ (see Aschwanden, 2005 p.118-119). In order to satisfy equation (2.40) the thermal pressure is taken as $p_1 = 43.8\ dyn\ cm^{-2}$, which is consistent with the lower chromosphere. The numerical domain contains $1,000$ grid points with a uniform spacing of $10\ km$ for a total length, $L = 10,000\ km$. Physical time is normalised as L/c_{S1}, giving a unit time, t of $1,000\ s$.

2.5.2 Model Equations

For the 1.5-D problem, the MHD equations implemented in VAC which describe the model are shown below:

$$\frac{\partial \rho}{\partial t} + \frac{\partial}{\partial z}\left(v_z \rho\right) = 0, \tag{2.27}$$

$$\frac{\partial}{\partial t}\left(\rho v_z\right) + \frac{\partial}{\partial z}\left(v_z \rho v_z\right) = -\frac{\partial}{\partial z}\left(p_{tot}\right), \tag{2.28}$$

$$\frac{\partial}{\partial t}\left(\rho v_\theta\right) + \frac{\partial}{\partial z}\left(v_z \rho v_\theta\right) = \frac{B_z}{\mu_0}\frac{\partial}{\partial z}\left(B_\theta\right), \tag{2.29}$$

$$\frac{\partial e}{\partial t} + \frac{\partial}{\partial z}\left(v_z e\right) = \frac{B_z}{\mu_0}\frac{\partial}{\partial z}\left(v_z B_z + B_\theta v_\theta\right) - \frac{\partial}{\partial z}\left(v_z p_{tot}\right), \tag{2.30}$$

$$\frac{\partial B_\theta}{\partial t} + \frac{\partial}{\partial z}\left(v_z B_\theta\right) = \frac{B_z}{\mu_0}\frac{\partial}{\partial z}\left(v_\theta\right), \tag{2.31}$$

where

$$p_{tot} = \frac{1}{2}\mathbf{B}^2 + p, \tag{2.32}$$

and

$$p = (\gamma - 1)\left(e - \frac{1}{2}\rho\mathbf{v}^2 - \frac{1}{2}\mathbf{B}^2\right). \tag{2.33}$$

For brevity, $\mathbf{B} = B_z\mathbf{e_z} + B_\theta\mathbf{e}_\theta$, and $\mathbf{v} = v_z\mathbf{e_z} + v_\theta\mathbf{e}_\theta$. The plasma density is denoted by ρ, whereas the longitudinal and transverse velocities are presented as v_z, and v_θ. The internal energy is denoted by e, whilst the thermal, and total pressures are p, and p_{tot}. B_z, and B_θ are the longitudinal and transverse magnetic field components. The derivation of these equations is shown in Appendix A.

In this first study, the gravitational force is not included in the momentum equation, which implies a highly inclined longitudinal magnetic field. Such magnetic field configurations are observed in the photosphere and in the chromosphere. Examples include sunspot penumbrae and plage regions in the chromosphere.

The last terms of equations (2.28) and (2.30) describe the non-linear coupling between the z and θ variables. Due to the small initial twist the perturbation of the magnetic field and corresponding derivatives remain small. Therefore, the initial system behaviour is linear. With amplification of the perturbations, the p_{tot} terms become more significant and lead to non-linear behaviour by producing momentum perturbations in the z components.

The expression for energy conservation, which is of the same form as that used by Hollweg [1992] is obtained through combining equations (2.30), (2.32), and

(2.33):

$$\frac{\partial}{\partial t}\left[\frac{p}{\gamma-1}+\frac{1}{2}\rho\mathbf{v}^2+\frac{1}{2}B_\theta^2\right] + \frac{\partial}{\partial z}\left(v_z\left[\frac{\gamma p}{\gamma-1}+\frac{1}{2}\rho\mathbf{v}^2\right]\right) + \frac{\partial}{\partial z}\left(v_z B_\theta^2 - v_\theta B_\theta B_z\right) = 0. \quad (2.34)$$

The terms within the temporal derivative of equation (2.34) give the thermal, kinetic, and magnetic energy densities. The two terms within the first spatial derivative give the convection of enthalpy and kinetic energy whereas the two terms in the second spatial derivative give the Poynting flux in the inertial frame.

2.5.3 Shock Equilibrium

In order to set-up the required stationary gas-dynamic shock in the centre of the shocktube, a longitudinal background flow, which is supersonic yet sub-Alfvénic is introduced. The plasma either side of the gas-dynamic shock is described by the Rankine-Hugoniot jump conditions (2.35) - (2.38). Subsequently, the background flow becomes subsonic once it passes through the shock interface whereas the density, pressure, and temperature of the plasma increase:

$$v_{z2} = v_{z1}\frac{\rho_1}{\rho_2}, \quad (2.35)$$

$$\rho_2 = \rho_1\frac{v_{z1}}{v_{z2}}, \quad (2.36)$$

$$p_2 = p_1 - \rho_2 v_{z2}^2 + \rho_1 v_{z1}^2, \quad (2.37)$$

$$e_2 - e_1 = \frac{1}{2}\left(v_{z1}^2 - v_{z2}^2\right) + \frac{p_1\rho_2 - p_2\rho_1}{\rho_1\rho_2}, \quad (2.38)$$

where

$$v_{z1} = M_{c1}c_S, \quad (2.39)$$

and

$$c_S = \sqrt{\frac{\gamma P_1}{\rho_1}} = \sqrt{\frac{\gamma RT}{\xi}}. \tag{2.40}$$

Subscript 1 denotes the plasma upstream of the shock and subscript 2 denotes the post-shock plasma. M_{c1}, and c_S are the sonic Mach number of the plasma flow, and sound speed in region 1. R is the molar gas constant, T is the plasma temperature, and ξ is the molar mass. From Priest [2014, p.181], equations (2.35) - (2.37) can be expressed in terms of the sonic Mach number of region 1:

$$v_{z2} = \frac{(\gamma-1)M_{c1}^2 + 2}{(\gamma+1)M_{c1}^2} v_{z1}, \tag{2.41}$$

$$\rho_2 = \frac{(\gamma+1)M_{c1}^2}{(\gamma-1)M_{c1}^2 + 2} \rho_1, \tag{2.42}$$

$$p_2 = \frac{2\gamma M_{c1}^2 - (\gamma-1)}{\gamma+1} p_1. \tag{2.43}$$

Analytically, the shock location is represented by a sharp discontinuity in the density, pressure, and velocity variables. The computational modelling of such a structure is difficult due to numerical inaccuracies appearing at the shock region. This difficulty in replicating an analytical shock is true regardless of the number of grid-points incorporated as there will always be an associated error. These errors lead to the Gibbs phenomenon at the shock with a trailing wake of oscillations downstream of the discontinuity. In order to eliminate this and introduce stability throughout the simulation, smoothing is introduced using a smooth cubic function:

$$v_z(z) = \frac{v_z(0) + v_z(\delta)}{2} + \frac{v_z(\delta) - v_z(0)}{4} \times \left(\frac{2z - z(\delta)}{z(\delta)}\right)\left[3 - \left(\frac{2z - z(\delta)}{z(\delta)}\right)^2\right], \tag{2.44}$$

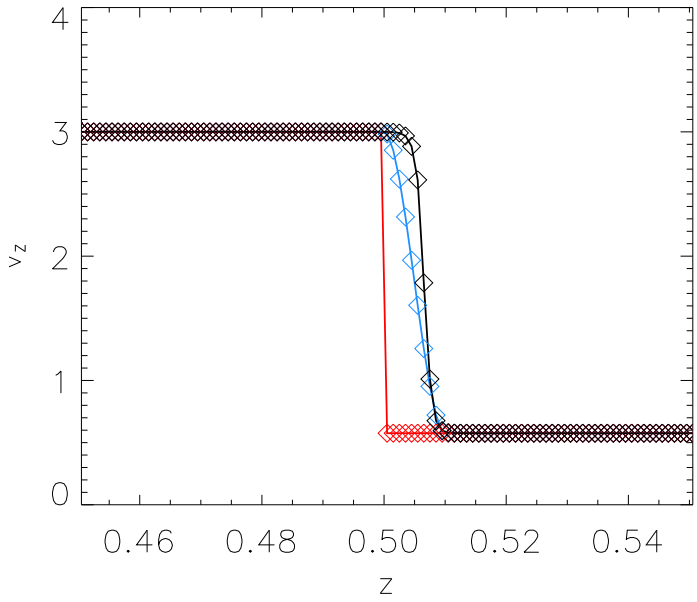

Figure 2.6: Plots show the intitial (*blue*) and final (*black*) shock interface configuration for a smooth cubic function. The final state shown here is the initial condition for subsequent simulations. The analytical (*red*), sharp discontinuity is provided for comparison.

where $z(0) < z < z(\delta)$, with $v_z(0) = v_{z1}$ and $v_z(\delta) = v_{z2}$ for $z > z(\delta)$. The flow speed at $t = 0$ is given by v_{z0}, and z is the physical position within the shocktube. The start and endpoints where the shock interface is modelled are denoted by positions $z(0)$, and $z(\delta)$. The smooth profile adjusts itself into a stable, static shock, where the Rankine-Hugoniot jump conditions are completely satisfied either side of this region (Figure 2.6). The resulting profile is then taken as the initial equilibrium from which the study begins.

2.5.4 Boundary Conditions

There are different approaches as far as photosphere boundary conditions are concerned. In studies of thin flux tubes it is customary to introduce a driven boundary at the photospheric level. For example, a driven photospheric boundary was introduced by Hollweg [1981] to study loop resonances and by Hollweg [1986], Van Ballegooijen et al. [2011] to study Alfvén wave turbulence via non-

linear interactions. On the other hand, in their study of wave propagation and conversion in $30 - 40\,Mm$ wide sunspot slabs, Khomenko et al. [2009] adopted a model which extends from $10\,Mm$ below the photosphere to the low chromosphere and has a gradual decrease in the density.

Two different types of wave excitation were implemented for the simulation. Firstly, consider a single sine-squared driver, F which is implemented as a source term in equation (2.29) with the following form:

$$\rho F = A \sin^2\left(\pi \frac{t - t_{min}}{t_{max} - t_{min}}\right) \sin^2\left(\pi \frac{z - z_{min}}{z_{max} - z_{min}}\right), \tag{2.45}$$

and in equation (2.30) as $\rho F \cdot v_\theta$. Note that, $t_{min} < t < t_{max}$, and $z_{min} < z < z_{max}$. The start time for the simulation is denoted as t_{min} and is chosen for any time after the equilibrium stabilises. The source term is active until time, $t = t_{max} = t_{min} + 0.2\,L/c_{S1}$. A is the amplitude of the driver and z_{min}, z_{max} denote the region in which the driver is active.

It is assumed that the ghost cells for ρ, ρv_z, e, B_z, and B_θ are all set as symmetric (reflects from close-by mesh cells). This corresponds to a zero derivative boundary condition, i.e. a Neumann boundary condition. This means that the reflected quantity is 'squashed' by the dense photosphere until the photosphere 'pushes' that quantity back into the atmosphere due to Newton's 3$^{\text{rd}}$ law of motion.

The boundary type for ρv_θ is set as asymmetric, which is the same as symmetric with the addition that the reflection is multiplied by -1. The multiplication by -1 means that the twist velocity changes sign and direction as the pulse interacts with the boundary. This corresponds to a Dirichlet boundary and allows the twist to reflect back into the direction it has just propagated from rather than allowing the twist to 'skip' off the surface and twist in the same direction continually. This choice of driver and boundary conditions generates a smooth Alfvénic pulse, which upon backward propagation reflects at the photospheric boundary.

Secondly, a driven boundary for ρv_θ was tested to drive the Alfvénic pertur-

bations from the photosphere. The driven boundary is prescribed as:

$$\rho v_\theta|_{z=0} = At \exp\left(-\frac{t}{T}\right), \tag{2.46}$$

where the decay time of the wave is $T = 1/1000\ L/c_{S1}$ and $t > t_{min}$. The remaining quantities are set to continuous at the left boundary. Additionally, it is worth mentioning that we also tested a driven boundary for $e|_{z=0} = e_1 + e_{k\theta}$ when driving the $\rho v_\theta|_{z=0}$ boundary. However, no discernible difference could be made between this incorporation and solely driving the $\rho v_\theta|_{z=0}$ boundary.

Convection in general is a complex compressible fluid motion with the energy spectrum corresponding to the turbulence. Cranmer and Van Ballegooijen [2005] took the power spectrum of transverse magnetic bright point motions in the photosphere as the lower boundary condition for their model of Alfvénic fluctuations. Here, we are interested in the basic physics of the twist evolution. In order to have a clear picture of the process, a single, decaying pulse of the form (2.46) is introduced at the footpoint. As the results are largely similar, the principle of Occam's razor may be applied in that the boundary condition (2.46) with fewest assumptions is best. That is, the ghost cells at the base of the magnetic shocktube are set as continuous for all variables except ρv_θ which is driven through equation (2.46) to excite Alfvén waves at the photospheric level. This is an inhomogeneous Dirichlet-like boundary condition for ρv_θ, which results in the boundary becoming reflective. At the other side of the shocktube, the boundary type for the ghost cells is set to continuous. This allows the propagation of waves and flows to pass through the end of the simulated region without any reflections.

2.6 The Instability Criterion

Alfvénic pulses generated in region 1 will become over-reflected and amplified at the shock interface if

$$v_{z1} > v_{z2} + c_{A2}, \tag{2.47}$$

where c_A denotes the Alfvén speed in the corresponding regions [Taroyan, 2008] and is described by:

$$c_A = \frac{B}{\sqrt{\mu\rho}}, \tag{2.48}$$

where μ is the permeability of free space.

In the case of a sub-Alfvénic flow, $v_{z1} < c_{A1}$ which also satisfies condition (2.47), the shock tube is unstable with respect to Alfvénic perturbations as they bounce back and forth between the shock interface and the photospheric driver upstream of the shock. The shock front reflects and transmits Alfvénic perturbations upstream and downstream with amplified amplitudes. It acts as an amplifier leading to the Alfvén instability. The flow velocity jump across the shock interface is expressed through the Rankine-Hugoniot relation (2.41).

Condition (2.47) contains equilibrium quantities both upstream and downstream of the shock that are dependent. Using the Rankine-Hugoniot relation for velocity (2.41) it is possible to rewrite the over-reflection condition (2.47) in terms of the independent sonic and Alfvénic Mach numbers in the upstream region 1. Firstly, note that the Alfvén speeds on either side of the shock are related through the equation:

$$\frac{v_{z1}}{c_{A1}^2} = \frac{v_{z2}}{c_{A2}^2}, \tag{2.49}$$

which is a consequence of the continuity condition (2.36). Substituting the expressions (2.41) and (2.49) into the over-reflection condition (2.47) yields

$$v_{z1} - \frac{(\gamma-1)\,M_{c1}^2 + 2}{(\gamma+1)\,M_{c1}^2} v_{z1} > \sqrt{\frac{v_{z2}}{v_{z1}}}\, c_{A1}. \tag{2.50}$$

Using the Rankine-Hugoniot relation (2.41) and the inequality (2.50), the following Alfvén instability criterion is derived in terms of the sonic Mach number, M_{c1}, and the Alfvénic Mach number, $M_{A1} = v_{z1}/c_{A1}$:

$$\frac{\sqrt{(\gamma+1)\,M_{c1}^2\,(\gamma-1)\,M_{c1}^2 + 2\,(\gamma+1)\,M_{c1}^2}}{2\,(M_{c1}^2 - 1)} < M_{A1} < 1. \tag{2.51}$$

This condition (2.51) shows that the Alfvén instability is not present when $M_{A1} \gtrsim 1$ because the flow becomes super-Alfvénic. For $\gamma \gtrsim 1$ the instability condition (2.51) is reduced to

$$\frac{M_{c1}}{M_{c1}^2 - 1} < M_{A1} < 1. \tag{2.52}$$

The above derived inequality (2.52) shows that the range of flow speeds for which the system is unstable becomes broader with increasing sonic Mach numbers.

2.7 Numerical Results

The implemented driver (2.46) which mimics the torsional component of the photospheric motions, such as granular buffeting, generates a small-amplitude torsional Alfvén wave. This twist propagates along the shocktube at a constant speed of $c_{A1} + v_{z1}$ until it interacts with the gas-dynamic shock.

At this point, if the flow is too low to satisfy the instability criterion (2.47), the pulse is partially reflected and transmitted with damped amplitudes. The reflected wave propagates against the supersonic plasma flow at a constant speed of $c_{A1} - v_{z1}$ until it reaches the photosphere. The wave bounces back and forth between the dense photosphere and static shock until the pulse vanishes after a few iterations of this process.

However, if the Alfvén instability is present, the Alfvén wave is amplified through over-reflection and transmission at the shock position. The pulse propagates backwards until it returns to the photosphere where it is reflected, and the process repeats (Supplementary Movie 1).

The amplification of the Alfvénic perturbation leads to the formation of secondary waves (Figures. 2.7 and 2.8). This occurs due to non-linear coupling of the transverse variables with the longitudinal variables in equations (2.28) and (2.31). The variable p_{tot} (2.32) translates twists in the magnetic field to form perturbations in the longitudinal variables. Initially, the Alfvénic perturbation is small, so the effects of this non-linear coupling between the two directions is negligible - *i.e.*

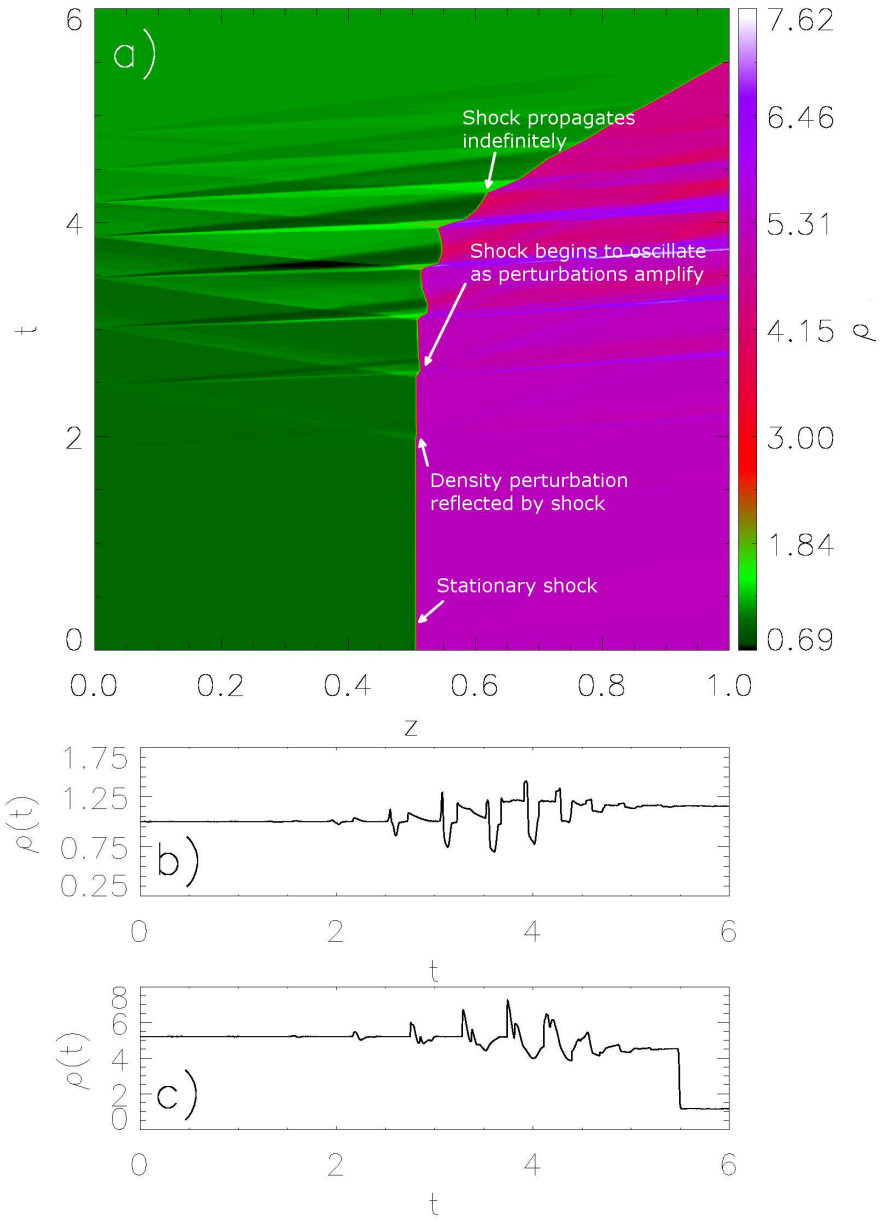

Figure 2.7: **a)** Time-distance plot for normalised density, ρ. The density upstream of the gas-dynamic shock increases and propagating shocks are seen here, as with Figure (2.8). **b)** The amplitude increase for the propagating secondary waves/shocks can be seen as a consequence of the Alfvén instability at $z = 0.3$. The final panel, **c)** shows the downstream density at $z = 0.99$.

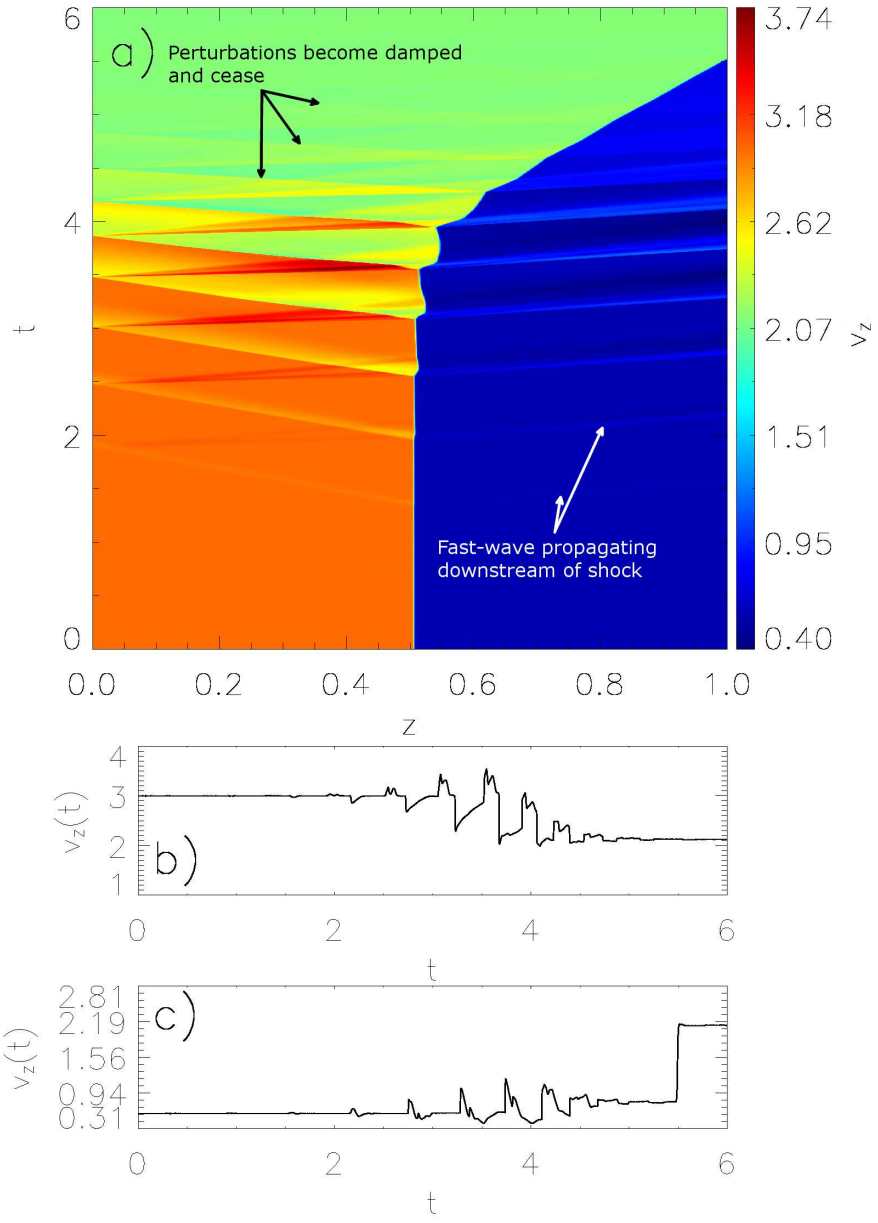

Figure 2.8: **a)** Time-distance plot of the normalised longitudinal velocity, v_z. It can be seen that the gas-dynamic shock remains stationary until propagating fast shocks form. Here, the shock is impelled along the z-direction by each shock that 'hits' the gas-dynamic shock. **b)** The flow speed upstream of the shock ($z = 0.3$) decreases as it is converted into twisting motions. Panel **c)** shows the flow speed at $z = 0.99$.

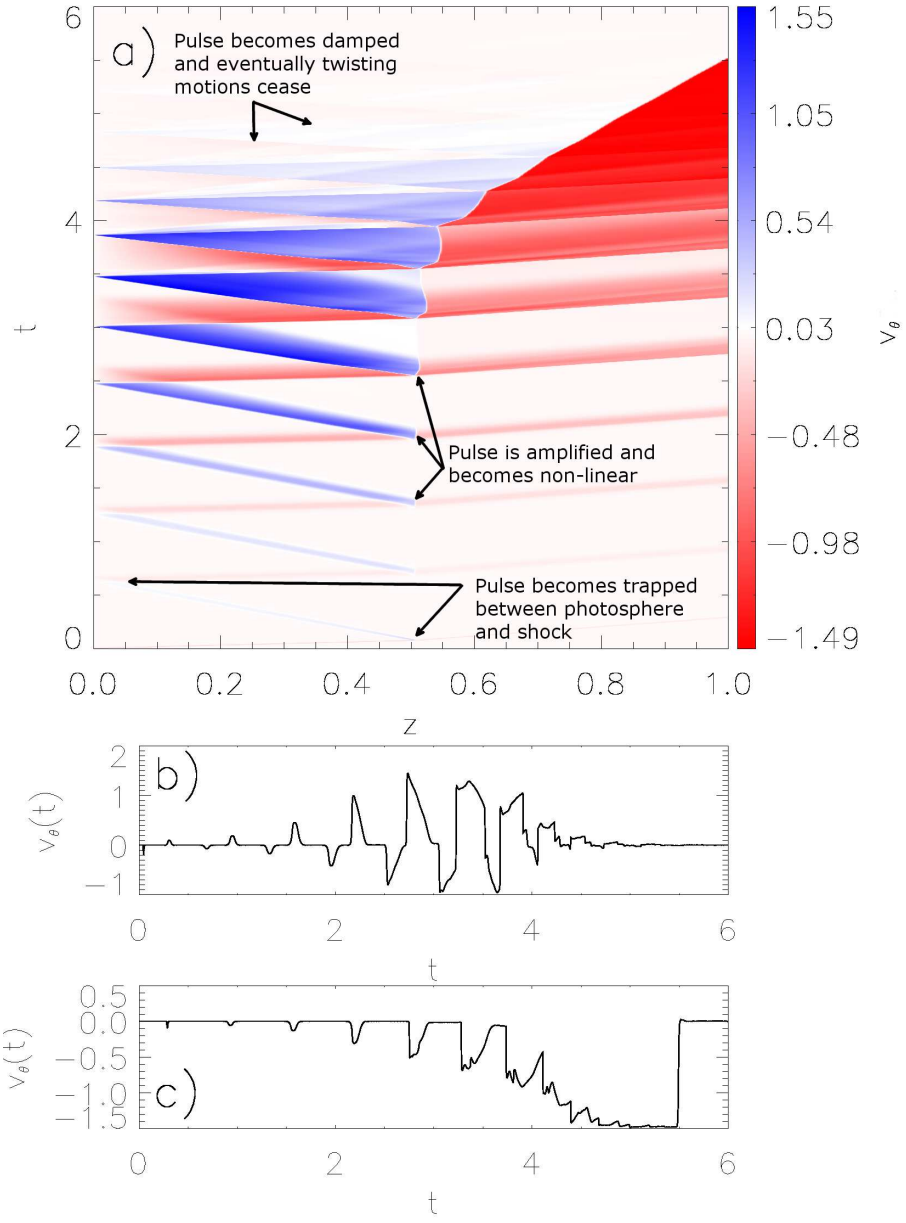

Figure 2.9: **a)** Time-distance plot of normalised v_θ. The velocity is negative upon forward propagation and positive on backward propagation of the Alfvén wave. The signal is amplified at the shock location upon each reflection, with a portion of the signal being transmitted. A standing slow shock forms at the gas-dynamic shock location and can be seen as a faint, white line after $t = 2$ at $z = 0.5$ (This is where v_θ transitions from negative (*red*) to positive (*blue*) values). **b)** shows the trapped portion of the Alfvén wave at $z = 0.3$. The transmitted portion is shown in panel **c)** for $z = 0.99$.

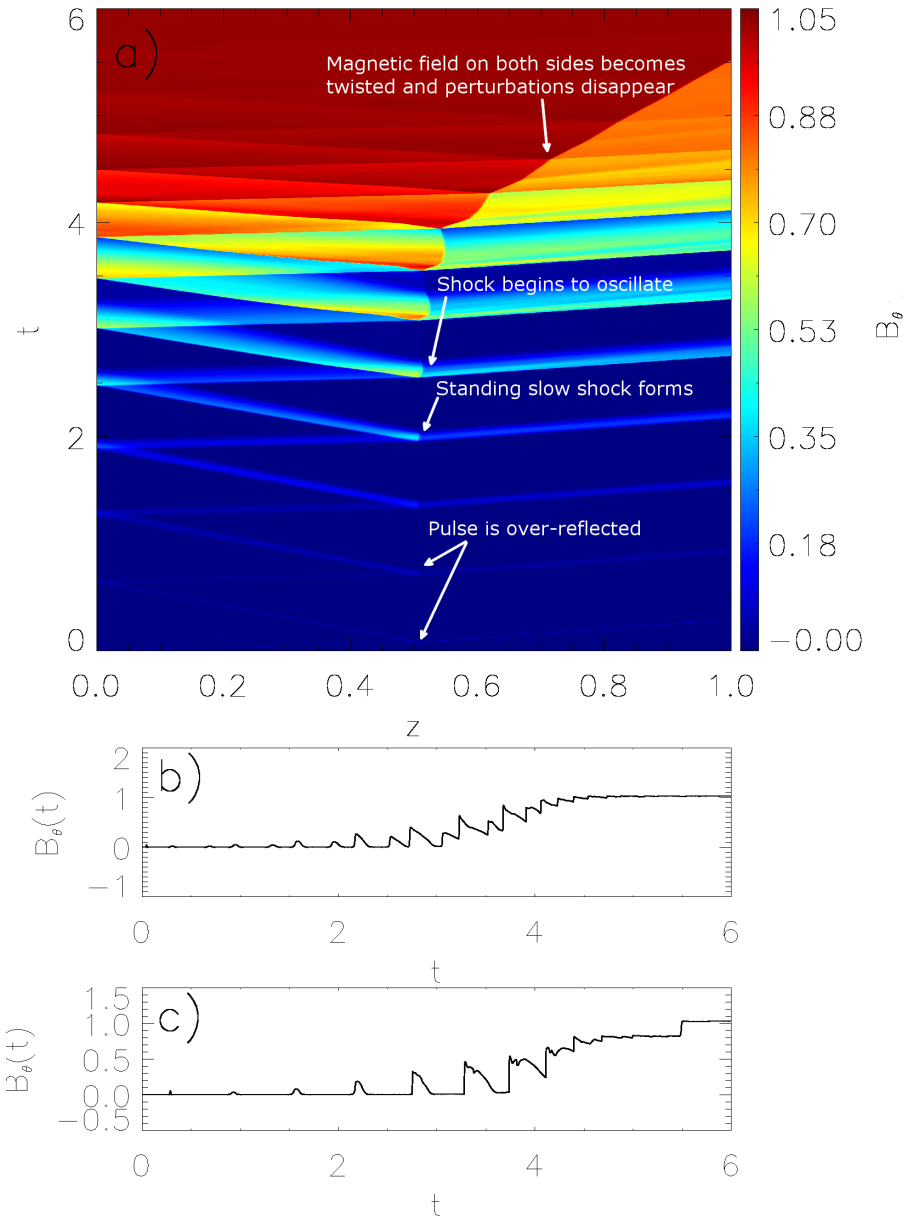

Figure 2.10: **a)** Normalised B_θ time-distance plot. The magnetic field initially exhibits a series of small twists that correspond to the Alfvén wave. These gradually amplify and form a standing shock, as is the case with v_θ. The twist is continually, in the same direction and the time taken for the twists to travel from the shock to the photopshere and back to the shock decreases upon each reflection. Panel **b)** shows that amplification and direction of the magnetic twist more clearly at $z = 0.3$. Panel **c)** highlights that the twist is not confined to the region between the shock and photosphere as a large amount of twisting occurs before the shock passes through $z = 0.99$. Once the shock propagates beyond the low-chromosphere, the magnetic flux tube remains permanently twisted.

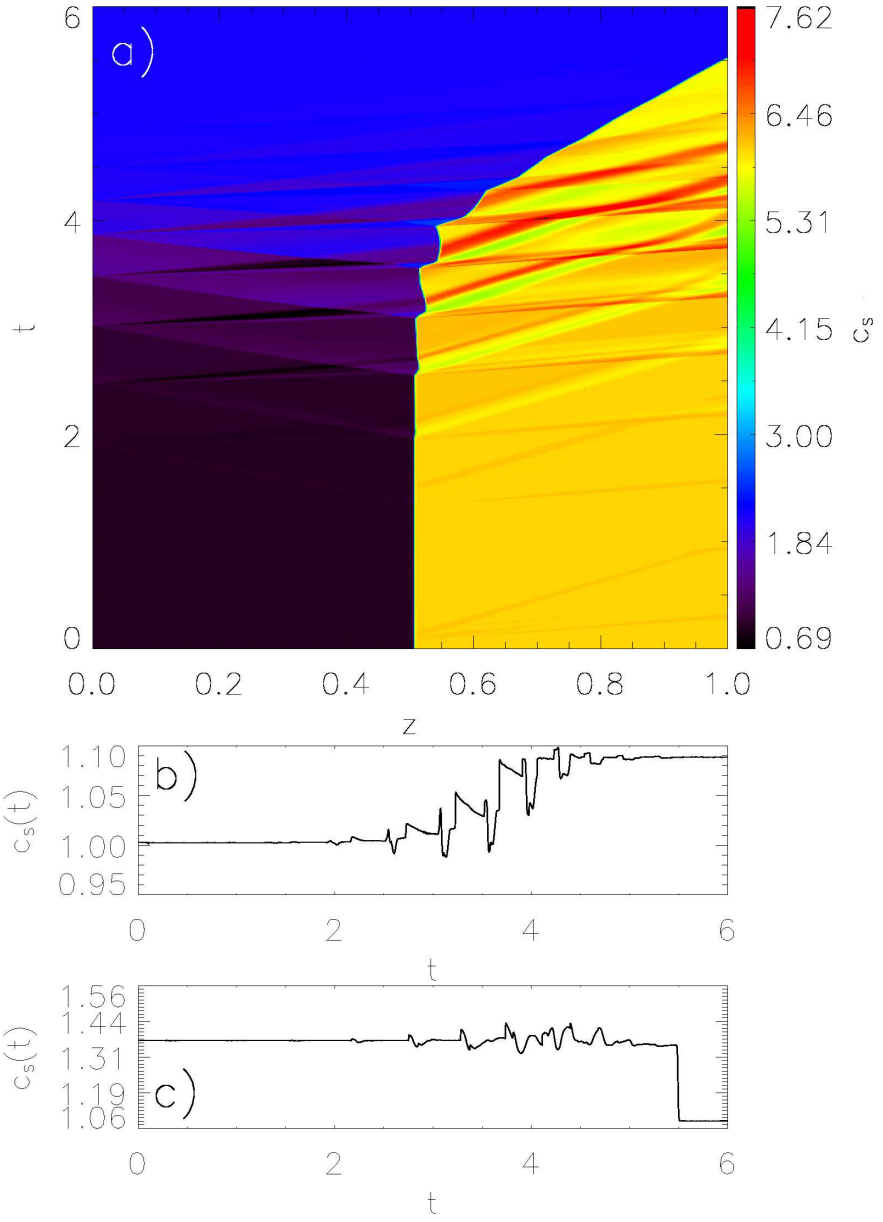

Figure 2.11: **a)** Normalised sound speed time-distance plot shows that as the non-linear effects take place, the sound speed, and from equation (2.40) temperature, increase upstream of the shock. **b)** Shows the sound speed variation for $z = 0.3$ and **c)** provides the variations for $z = 0.99$.

this corresponds to the linear stage of the amplification process. The secondary waves generated by the initial twist correspond to fast- and slow-magnetoacoustic waves propagating along the magnetic field lines with phase speeds of c_A and c_S in the flow reference frame. This is discussed in detail in the book by Priest [2014].

During the growth of the Alfvén wave via over-reflection, the non-linear coupling becomes more important, as the magnetoacoustic waves form into propagating shocks. These are described by Hollweg [1992] as an increase in $|B_\theta|$ across the shock for a fast shock and a decrease in $|B_\theta|$ across the shock for a slow one. The fast-shock corresponds to the leading edge of the Alfvénic pulse and travels at $c_A + v_z$ upon forward propagation, and $c_A - v_z$ on backward propagation. The slow-shock travels at the $c_S + v_z$ on forward propagation and corresponds to the trailing edge of the Alfvénic pulse.

However, unlike the fast-shock, the reflected slow-shock does not propagate against the plasma flow once it reaches the gas-dynamic shock, nor does it propagate through the shock interface and out of the low-chromosphere. Instead, it remains at the gas-dynamic shock location as it is too slow to propagate against the upcoming flow, yet too fast for the post-shock flow to overcome its backward propagation.

Note that unlike previous studies (Hollweg, 1992; Hollweg et al., 1982; and others), the formation of slow and fast shocks does not require the presence of gravity. Instead, the formation of these shocks is caused by the instability mechanism.

Each subsequent slow-shock that is generated by the photospheric reflection of the Alfvénic pulse is trapped in the same manner, with each one merging with the gas-dynamic shock and contributing to the formation of a standing shock in v_θ and B_θ. This evolution of the slow-mode waves with the gas-dynamic shock can be seen in Figures. (2.9) and (2.10) and Supplementary Movie (2) as initially there is no discernible difference between the pre-shock and post-shock values - and later it is clear that a standing shock is created in the transverse variables. In general, it is possible that when two or more shocks are formed that one may

catch-up and overtake the other(s). The shocks may then combine and continue to propagate as a single shock. This lead to the belief that shock heating is responsible for heating the chromosphere in early 1-D models. However, multi-dimensional studies have shown that this confluence does not occur and shocks merely pass through each other unless perfectly aligned. For more detail on the confluence of shocks, see Whitham (2011; p.52-53 & p.110-112).

In addition to the generation of shocks, the non-linear coupling also affects the sound speed (Figure 2.11), and Alfvén speed (Figure 2.12) of the shocktube plasma. It is clear that a change in sound speed also means a change in the plasma temperature (see equation 2.40). Therefore the system evolves into a configuration of ever-increasing complexity until the Alfvénic pulse ceases to amplify and twist the shocktube due to the propagation of the gas-dynamic shock. Figure (2.12) also shows that as the damping time of the driver becomes long, the amplification process and the non-linear evolution occurs over a shorter period of time. However, qualitatively the response of the system to the twist remains similar.

Once the gas-dynamic shock propagates out of the modelled magnetic flux tube, the Alfvén wave disappears, and a new equilibrium is formed. The resulting equilibrium is shown in Figure (2.12) and Supplementary Movies (2) and (3) after $t = 4.5\ L/c_{S1}$. The magnetic field has become highly twisted from the entrapment and amplification of the Alfvén wave between the gas-dynamic shock and photosphere. The highly twisted magnetic field leads to the Alfvén speed doubling when the non-linear coupling is at its strongest, and remains raised thereafter (Figure 2.12). The plasma flow remains supersonic, though its speed has been reduced by the Alfvén wave amplification through over-reflection at the shock interface. The density and pressure have been raised to $\rho = 1.14\rho_1$ and $p = 1.33p_1$. This is a consequence of the non-linear coupling, which has altered the plasma properties, *i.e.* heating of the flux tube, increased magnetic field strength, Alfvén and sound speeds increasing and a decrease in flow speed upstream of the shock.

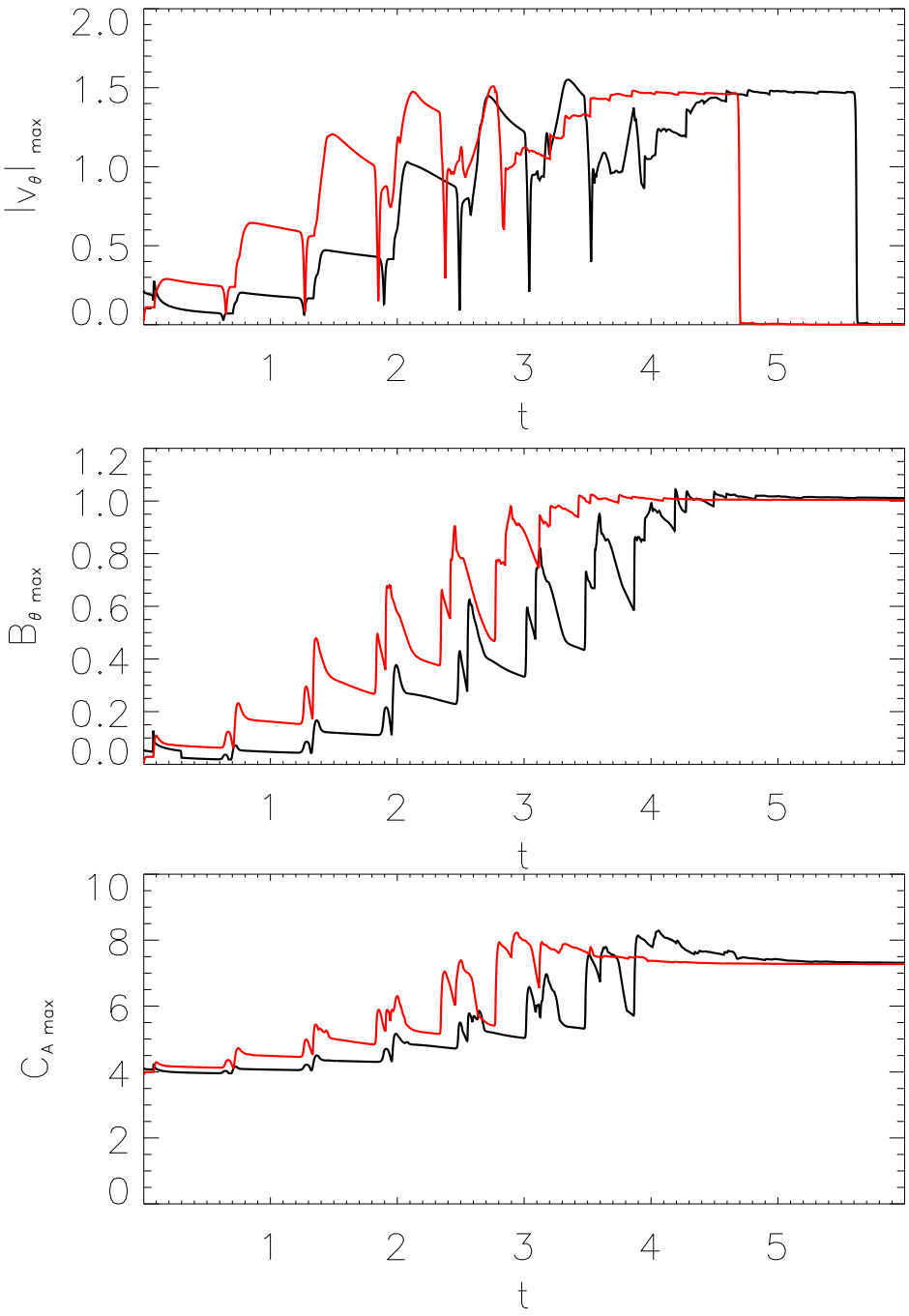

Figure 2.12: Plots showing the maximum values of $\mid v_\theta \mid$, B_θ, and the Alfvén speed as functions of time. The sharp, thin dips seen in $\mid v_\theta \mid$ correspond to a change in direction for the pulse, i.e. the velocity is changing from positive to negative or negative to positive - the velocity value decreases, passes through zero and increases to the correct size. A comparison where the decay period, T of equation (2.46) is changed to 10 T is provided (*red lines*).

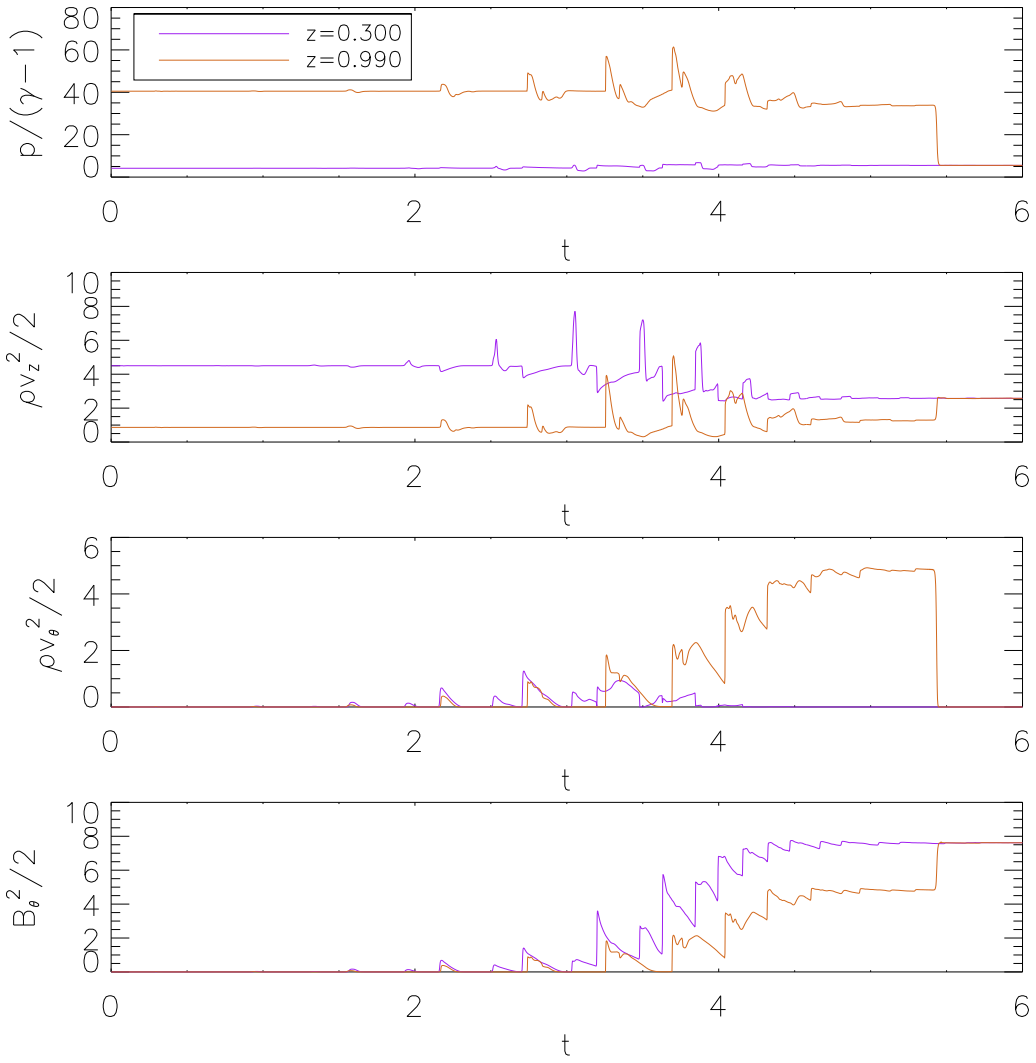

Figure 2.13: The internal energy of the shocktube plasma is split into its constituents - thermal, z-kinetic, θ-kinetic, and θ-magnetic energies for $z = 0.3$ (*brown*) and $z = 0.99$ (*purple*).

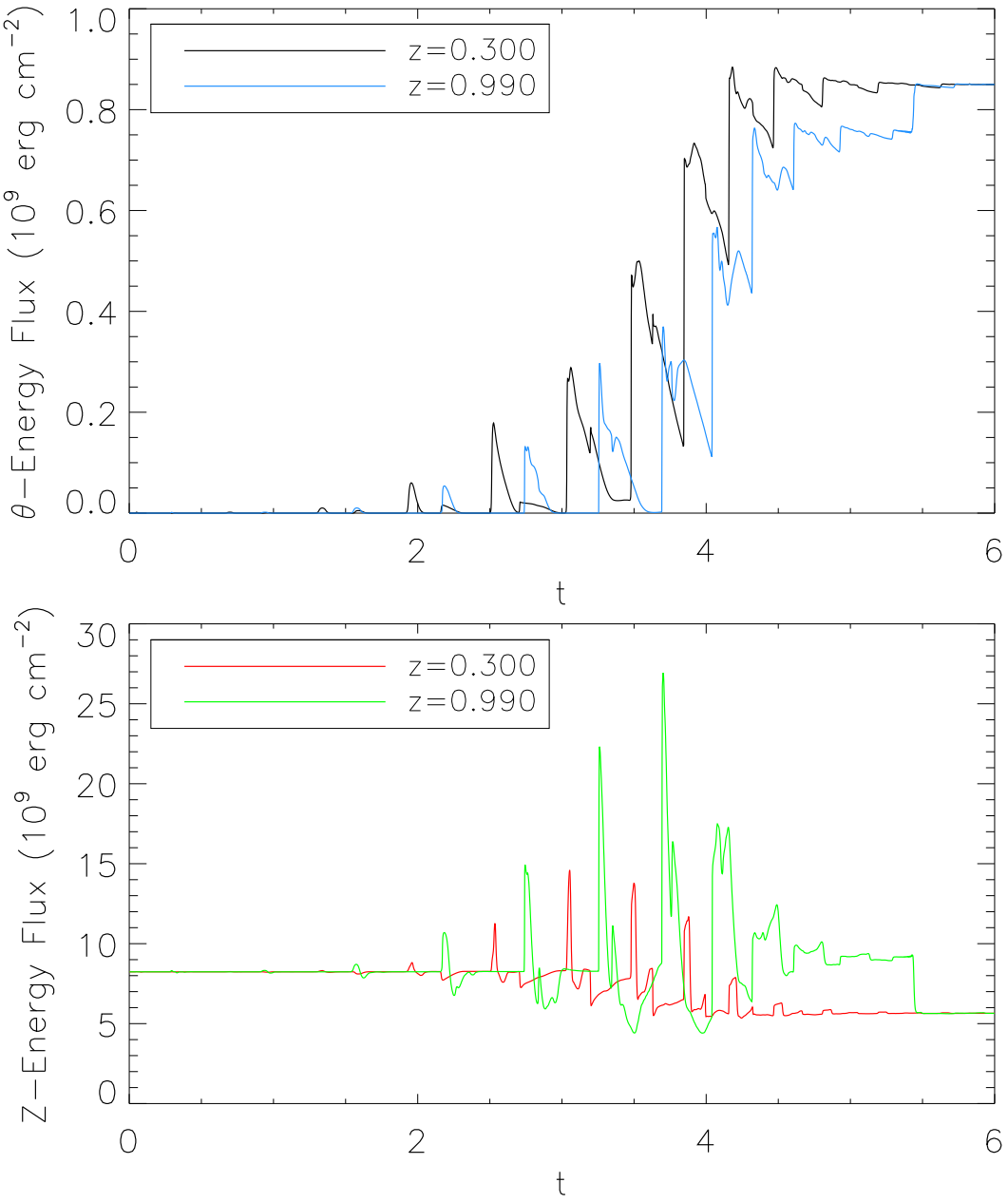

Figure 2.14: *Top*: z-energy flux density, *bottom*: θ-energy flux density of the shocktube plasma. Each plot shows their respective quantities for all time at positions $z = 0.3$ and $z = 0.99$.

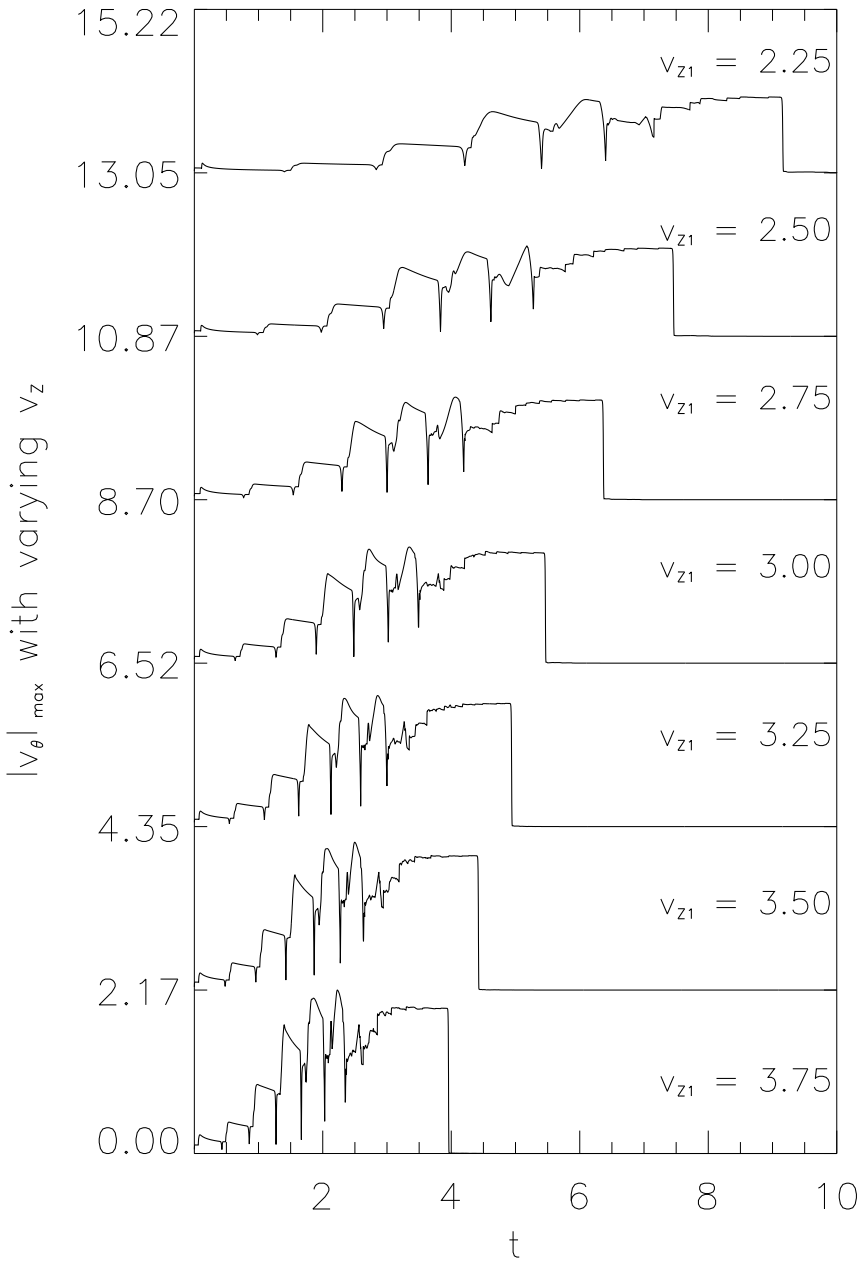

Figure 2.15: Plots show the effect varying the flow speed, v_z has on the evolution of v_θ. Each plot is shifted by a value of 2.175, which is the maximum amplitude of v_θ seen in any of the simulations. The increase in v_z shows that the duration for the amplification to occur and 'push' the gas-dynamic shock beyond the low-chromosphere reduces and the maximum amplitudes of the wave increases. An initial flow speed of $v_{z1} = 2.25\ c_{S1}$ is the lower limit for the instability to occur with the chosen Alfvén and sound speeds.

2.7.1 Gas-Dynamic Shock Propagation

Here, the physical behaviour of the region which is related to the gas-dynamic shock is considered. Initially, the momentum either side of the shock is balanced due to the Rankine-Hugoniot jump conditions (2.35) - (2.38). The advection term in the longitudinal momentum equation (2.28) is balanced by the pressure gradient on the right hand side. When the propagating shock-waves are reflected by the gas-dynamic shock, a standing shock is formed. This leads to an extra non-linear magnetic pressure force in the momentum equation, which is positive due to the negative gradient in B_θ. The total pressure force becomes positive and the shock front gains momentum in the positive direction. This imbalance persists until the magnetic pressure force declines and is no longer able to push the shock-front forward.

At first, the shock returns to its initial location as the movement of the gas-dynamic shock is small (this can be seen in all the time-distance plots and Supplementary Movies 2 and 3). The non-linear magnetic pressure force vanishes due to the vanishing gradient in B_θ. The negative thermal pressure force takes over and the shock-front is 'pulled' back due to the total pressure force becoming negative on the right hand side of the momentum equation (2.28). Once the trailing edge clears the immediate downstream of the shock, the Rankine-Hugoniot jump conditions are virtually restored and the shock becomes quasi-static.

Upon each reflection of the Alfvénic pulse at the interface, the width and amplitude of the propagating pulse increases. It is this broadening of the signal which is responsible for the eventual propagation of the gas-dynamic shock. Again, consider the same situation as before, but with an Alfvénic pulse with large amplitude. Once the leading edge of the Alfvénic pulse and fast-shock pass through the shock-front, the slow shock and with it the magnetic pressure gradient increase in amplitude. The separation between the fast- and slow-shock has now become sufficiently large so the time from when the initial pulse reaches the shock-front until all the Alfvénic perturbations have propagated beyond the immediate downstream of the interface has increased significantly. This means it

takes longer for the Rankine-Hugoniot conditions to be restored and the shock to become stationary again.

Once the signal is sufficiently amplified and broadened however, this restoration ceases to occur. The Alfvénic pulse that was previously reflected from the gas-dynamic shock has travelled to the photosphere, reflected, and propagated back to the reference frame before the trailing edge has cleared the immediate downstream of the gas-dynamic shock. This increases the imbalance further, and causes the gas-dynamic shock to continue to propagate along the shock-tube before the Rankine-Hugoniot conditions can be restored. This key juncture in the balance of forces at the gas-dynamic shock location occurs between $t = 4.0 - 4.5\, L/c_{S1}$.

The propagation of the gas-dynamic shock can be interpreted by looking at the non-linear term of equation (2.28). As is mentioned previously, the slow propagating shock becomes trapped at the gas-dynamic shock upon reflection as it cannot propagate against the upflow of plasma, but is too fast for the plasma downstream of the gas-dynamic shock to carry it forwards. This means B_θ decreases across the slow shock in the direction of the plasma flow. This leads to a negative derivative, and as there is a minus sign in-front of the term in equation (2.28), the term becomes positive. Thus, as the slow shock grows in amplitude at the gas-dynamic shock position, it leads to the torsional magnetic twists being converted into z-momentum.

2.7.2 The Conversion of Energy and Generation of a Global Twist

In the non-linear regime, the slow shock becomes important in the over-reflection process. As the fast shock propagates back and forth between the photosphere and gas-dynamic shock, the slow shock becomes trapped upon reflection and forms a stationary shock, which is separate to the gas-dynamic shock. The slow shock grows in amplitude upon each successive reflection of the Alfvénic pulse. This prevents the fast shock amplitude from decreasing, as it provides a cavity

in which the flux tube may continually twist.

Downstream of the gas-dynamic shock, the fast shock only ever propagates forwards. This means that the derivative of p_{tot} is always negative, giving an increase to the longitudinal momentum from equation (2.28). Thus, downstream of the gas-dynamic shock, the Alfvén wave converts magnetic energy into kinetic energy. This behaviour means the Alfvén signal acts as a means of energy transport between the two regions either side of the gas-dynamic shock.

The non-linear term also allows the Alfvén wave to convert kinetic energy of the plasma flow into magnetic energy when the Alfvén instability is present. Once the wave has been reflected by the gas-dynamic shock, the backward propagating pulse generates an increase in the derivative of B_θ in the direction of the flow. This causes a decrease in v_z at the location of the pulse. As the pulse amplifies and broadens, the tail end of the pulse occupies the entirety of the plasma upstream of the gas-dynamic shock. Now, the pulse continually converts kinetic energy from the entire region into magnetic twists, and the flow does not get a chance to restore to its initial velocity.

Whilst the non-linear term in equation (2.28) is responsible for creating the slow shock in the z-momentum and allowing the over-reflection process to evolve, it is also responsible for its demise. The generation of B_θ perturbations leads to an increased Alfvén speed for the plasma (Figure 2.12). This increase in Alfvén speed changes the minimum flow speed required for the Alfvén instability to occur from 2.25 c_{S1} to 2.95 c_{S1} by $t = 4\ L/c_{S1}$. The flow at this time has decreased to $v_z = 2.853\ c_{S1}$. Thus, the amplification of the Alfvén wave no longer occurs as the Alfvén instability is not present. The non-linear coupling continues to convert the kinetic energy of the flow into magnetic twists, further decreasing the flow speed, and the Alfvénic signal dampens and then ceases.

2.7.3 Energy Flux and Energy Density

Following Hollweg [1992], equation (2.34) can be split into longitudinal and transverse components to yield the energy fluxes for z and θ:

$$F_z = \frac{1}{2}\rho v_z^3 + \frac{v_z \gamma p}{\gamma - 1}, \tag{2.53}$$

and

$$F_\theta = \frac{1}{2}\rho v_\theta^2 v_z + \frac{1}{\mu}\left(B_\theta^2 v_z - B_z v_\theta B_\theta\right). \tag{2.54}$$

where μ is the permeability of free space.

It is worth noting that the integral of the internal energy may be expressed as:

$$\frac{\partial}{\partial t}\int_{z_1}^{z_2} e \, \mathrm{d}z = F(z_1) - F(z_2). \tag{2.55}$$

This shows that the difference in the energy flux between two spatial locations is equal to the temporal derivative of the energy content in the region between those two locations. The energy content in a region increases when the right hand side of the above equation is positive. Conversely, a negative flux difference corresponds to a decrease in the energy content.

Figure (2.14) shows that during the linear stage of the evolution the torsional flux upstream and downstream of the gas-dynamic shock are approximately equal and there is no change in the energy content. However, as the system becomes non-linear, the θ-flux downstream of the gas-dynamic shock does not amplify as much as the flux upstream of the gas-dynamic shock (Figure 2.14). The explanation for this is related to the propagation of the fast shock. That is, the non-linear coupling term in equation (2.28) translates the magnetic perturbations into z-momentum. Thus, some of the θ-flux generated by the Alfvénic perturbations at $z = 0.3\ L$ is not seen by the time the perturbations reach $z = 0.99\ L$. The decrease in the θ-flux from left to right is represented by the difference between the black and blue curves in Figure (2.12). According to equation (2.55) this leads to an increase in the corresponding energy content, namely, the magnetic energy and the θ component of the kinetic energy. Indeed, Figure (2.13) shows an in-

creasing trend for the θ components of the energy density. Similarly, the increase in the z-flux from left to right represented by the difference between green and red curves in Figure (2.12). According to equation (2.13), the result is a decrease in the corresponding energy content represented by the thermal energy and the z-component of the kinetic energy. Again, this is evidenced by Figure (2.13). The slight increase in the kinetic energy density at $z = 0.99\ L$ is explained above. These results indicate that the instability mechanism extracts the z components of energy and largely converts those into θ components.

2.7.4 The Effect of Flow Speed on the System Evolution

The effect the initial flow speed, v_z has on the evolution with respect to the Alfvénic instability discussed in section (2.6) is also investigated. For an initial Alfvén speed of 3.89 c_{S1}, the range for the flow-speed that will yield the Alfvénic instability is $2.25\, c_{S1} \leq v_{z1} \leq c_{A1}$. All parameters are kept constant, with the same values as used before, but with v_{z1} varying from $2.25\, c_{S1}$ to $3.75\, c_{S1}$ in increments of $0.25\, c_{S1}$. Figure (2.15) shows that as the initial flow-speed approaches the initial Alfvén speed, the time required for the Alfvénic pulse to amplify and 'push' the gas-dynamic shock out of the low-chromosphere decreases. The speed of this process more than doubles when $v_{z1} = 3.75\, c_{S1}$ compared to when the initial speed is taken as the lower velocity limit, $v_{z1} = 2.25\, c_{S1}$. It can also be seen in Figure (2.15) that not only does the time required for this process to occur decrease but the amplitude of the Alfvénic perturbations increase with increasing flow-speed. These results are interesting as one could initially assume that as the flow-speed approaches the Alfvén speed, it may inhibit the backward propagation of the reflected waves/shocks due to $c_A - v_z$ approaching 0. When the initial flow-speed approaches the Alfvén speed, the strength of the over-reflection of the pulse at the gas-dynamic location must sufficiently increase the Alfvén speed upon reflection so that the backward propagation is not inhibited. It may be trivial to mention, but it is worth remembering that the fast- and slow-shock forward propagation will only increase as the flow-speed increases, which is another contributing factor into the decreasing timespan for the instability to amplify the Alfvén waves and 'push' the gas-dynamic shock out of the shocktube.

2.8 Discussion

It has been shown that a small twist may amplify through over-reflection at a gas-dynamic shock. This occurs for a supersonic yet sub-Alfvénic flow. The Alfvén wave amplifies through harnessing kinetic energy of the supersonic flow upon reflection at the shock location and converts it into magnetic twists. Due to this strong reflection at the shock, and the inability for perturbations to propagate into the photosphere, the Alfvénic pulse becomes trapped between the photosphere and gas-dynamic shock. Here, it continually amplifies and broadens until a non-linear system evolves due to the instability. The magnetic twists reach a maximum velocity of $v_\theta = 15.4\ km\ s^{-1}$ with the magnetic field eventually reaching a global twist of $B_\theta = 1.04\ B_z$. During the linear stage of the evolution, the twists propagate downstream quasi-periodically with each pulse lasting for about $10\ s$. However, as the amplitudes increase and non-linearity sets in, the periodicity deteriorates and the pulses last longer. The propagating non-linear twists are a signature of fast shocks accompanied by fluctuations in density, temperature and flow speed. The entire process of evolution from an undisturbed shocktube to a globally twisted tube takes about 50 minutes. This is within the lifetimes of Evershed flows [Rimmele, 1994].

The non-linear coupling means that the Alfvén pulse converts the kinetic energy of the plasma flow into magnetic energy upstream of the stationary shock. Downstream of the shock, these twists are partially converted back into the flow as kinetic energy. The Alfvén pulse thus acts as a means of energy transport from the upstream to the downstream plasma.

The conversion of kinetic energy from the background flow to magnetic energy in the upstream plasma leads to an imbalance in the total pressure gradient as a slow shock is set-up. At first, the gas-dynamic shock remains quasi-stationary as the Rankine-Hugoniot jump conditions are disturbed then restored. However, as the over-reflection of the Alfvénic pulse continues, the time taken for the jump conditions to restore increases until eventually they cannot be restored before the leading edge of the pulse has returned to the gas-dynamic shock. At this point,

the gas-dynamic shock continually propagates until it exits the flux tube.

Before the shock is lost, the Alfvénic perturbations have sufficiently converted kinetic energy of the supersonic flow into magnetic twists such that the Alfvén instability is lost. The perturbations are now damped upon reflection and eventually cease all together.

The magnetic field, unlike the torsional velocity, continually twists in the same direction during this study. This is regardless of the propagation direction of the torsional perturbations. Similar twisting motions have been seen as magnetic swirls in solar tornadoes [Li et al., 2012; Su et al., 2014]. Wedemeyer-Böhm and Steiner [2014] showed numerically that such spiral motions are caused by the rotation of magnetic field structures, which are driven by photospheric vortices. However, previous work by Shelyag et al. [2013] demonstrates that these motions are due to torsional Alfvén waves.

The twisting motions are not only confined to the region between the photosphere and gas-dynamic shock. It is seen in Figure (2.10) that the portion of the Alfvénic pulse, which is transmitted through the gas-dynamic shock induces a global magnetic twist. This means that the mechanism could permanently twist a larger flux tube without the gas-dynamic shock propagating along the entirety of the flux tube. The final state of the shocktube presented is similar to the equilibrium assumed by Zaqarashvili et al. [2010] and Díaz et al. [2011]. They consider a magnetic flux tube with a helical magnetic field and mass flow along the z-axis. This means the magnetic field structure is 'pulled' along the flux tube without any deformation. These twisted flux tubes are prone to the kink instability, which may lead to explosive events such as solar flares and CMEs.

The amplification of the Alfvén wave results in velocities $\approx 10-15\ km\ s^{-1}$, which is within the lower limits of the ranges observed in the chromosphere [De Pontieu et al., 2007, 2014]. The observed twists last for less than a minute and propagate at the local Alfvén speed. However, the torsional amplitude of the waves presented in this model is somewhat lower than the reported values in Type-II

spicules, which have torsional velocities of $25 - 30\ km\ s^{-1}$ [De Pontieu et al., 2012]. That said, the field-aligned flow of Type-II spicules observed by De Pontieu et al. [2012] is between $50 - 100\ km\ s^{-1}$, which is $2 - 3$ times the initial background flow employed in this study. Also, the amplitudes are expected to increase with increasing altitude when gravitational stratification is taken into account.

The θ-energy flux density observed during this study is $4 - 5\times$ larger than that seen in spicular studies [Hollweg et al., 1982; Kudoh and Shibata, 1999; Matsumoto and Shibata, 2010]. However, this is not necessarily a negative attribute as these studies either meet the lower end of the energy requirement to heat the quiet corona [Kudoh and Shibata, 1999] or fail to meet even these minimum requirements for coronal heating [Hollweg, 1992]. This increased flux density is due to the background flow, the energy of which is extracted and transferred downstream by amplified twists. That said, the values employed are all consistent with the lower chromosphere.

Incorporating gravity and a magnetic flux tube that expands as a function of height, such that $rB_z \approx constant$, where r is the flux tube radius, leads to increased torsional velocities as an Alfvén wave propagates outwards [Erdélyi and James, 2004; Hollweg, 1992; James et al., 2003]. These additions to the model will only serve to further increase the amplitude of the torsional motions seen, and possibly strengthen the effects of the Alfvénic instability along the shocktube.

2.9 Conclusion

Using the 1.5-D approximation for a magnetic shocktube, it has been shown that a gas-dynamic shock traps and amplifies a twist when the flow is supersonic and sub-Alfvénic. Propagating fast shocks are produced due to the non-linear coupling in equations (2.28) and (2.30) once the Alfvén wave is sufficiently amplified. The amplification and broadening of the Alfvénic pulse leads to magnetic twisting motions that are always in the same direction, much like the swirls seen in solar tornadoes [Li et al., 2012]. This continuous twisting in the same direction leads

to a global twist along the flux tube where B_θ becomes, and remains comparable to B_z.

The amplification strengthens the non-linear effects and destabilises the gas-dynamic shock. Initially, the shock sways back and forth as the total pressure balance is repeatedly disturbed by the impelling signals.

Eventually, the pressure balance can no longer be restored and the gas-dynamic shock propagates indefinitely. The twisting motions cease to amplify at this point as the Alfvénic pulse becomes damped in the absence of the Alfvén instability. The end result is a highly twisted magnetic flux tube with a sub-Alfvénic mass flow which pulls the magnetic field structure along the z-axis. This is much like the flux tubes used as a starting point for kink instability studies by Zaqarashvili et al. [2010] and Díaz et al. [2011].

The torsional energy flux generated by this mechanism is comparable to spicular models that provide sufficient energy to heat the corona (Kudoh and Shibata, 1999; Matsumoto and Shibata, 2010). However, adding gravitational stratification, losses and expansion of the flux tube will affect the Alfvén instability and torsional flux generated by the model and will be addressed in a future study.

Chapter 3

Alfvén Wave Amplification in an Intergranular Lane Downflow

The work presented in this chapter has been published in the Astrophysical Journal [Taroyan and Williams, 2016].

3.1 Abstract

The interaction of an intergranular downdraft with an embedded vertical magnetic field is examined. It is demonstrated that the downdraft may couple to small magnetic twists leading to an instability. The descending plasma exponentially amplifies the magnetic twists when it decelerates with depth due to increasing density. Most efficient amplification is found in the vicinity of the level where the kinetic energy density of the downdraft reaches equipartition with the magnetic energy density. Continual extraction of energy from the decelerating plasma and growth in the total azimuthal energy occurs as a consequence of the wave-flow coupling along the downdraft. The presented mechanism may drive vortices and torsional motions that have been detected between granules and in simulations of magnetoconvection.

3.2 Introduction

Millions of granules representing the visible tops of convective cells cover the photosphere of the Sun. They have different shapes and sizes. Hot material rising to the surface in bright granules falls back down along the cool and dark intergranular lanes. Numerical experiments show that the topology of convection beneath the solar surface is dominated by effects of stratification. This leads to gentle, expanding and structureless warm upflows on the one hand, and strong, converging filamentary cool downdrafts on the other hand [Stein and Nordlund, 1989]. These experiments are confirmed by spectral observations of granulation which reveal blue shifts in the bright sections with red shifts and increased line widths in the darker sections [Nesis et al., 2001].

The magnetic field is ubiquitously present in the solar photosphere and exhibits a wide range of scales and strengths [de Wijn et al., 2009; Solanki et al., 2006]. Magnetic flux emergence through the solar surface is driven by buoyancy and advection. On granular scales, it undergoes continual deformation and displacement because the ratio of gas to magnetic pressure is large in the convection zone. Diverging upflows sweep magnetic flux to intergranular downflow lanes where the downflow speeds significantly exceed the upflow speeds [Tao et al., 1998; Thelen and Cattaneo, 2000; Vögler, 2005; Weiss et al., 2002]. This results in a magnetic field strength of a few hundred Gauss at the solar surface. Flux tubes emerging through the surface are produced either from emerging loops that then open up through the top boundary or by concentration of magnetic flux by horizontal flows in the intergranular lanes. Far below the surface their field lines spread out in many different directions [Stein and Nordlund, 2006].

Further intensification to kG strength may be driven by the mechanism of convective collapse [Bushby et al., 2008; Spruit and Zweibel, 1979; Webb and Roberts, 1978]. Numerical simulations of convective collapse [Danilovic et al., 2010] and *Hinode*/SOT observations [Fischer et al., 2009; Nagata et al., 2008; Shimizu et al., 2008] show downflows of between 7 and 14 km s^{-1}.

Downdrafts are often seen to support vortices in simulations of convection [Muthsam et al., 2010] and magnetoconvection [Nordlund et al., 2009]. Moll et al. [2011] found that the vortex features which develop in the downflow lanes typically exist for a few minutes, during which they are moved and twisted by the motion of the ambient plasma. Shelyag et al. [2013] argued that the apparent vortex-like motions are signatures of propagating twists or torsional Alfvénic perturbations rather than vortices.

Vortex flows were only recently detected in SST and Sunrise observations of magnetic bright points in the photosphere [Bonet et al., 2008, 2010; Steiner et al., 2010]. Photospheric twists and vortices are thought to be responsible for producing similar types of motions in the solar atmosphere. These include chromospheric swirls [Wedemeyer-Böhm and van der Voort, 2009], prominence tornadoes [Li et al., 2012; Wedemeyer-Böhm et al., 2013], and twists on spicules [De Pontieu et al., 2014]. However, no clear connection has yet been established although some studies show that vortex tubes can penetrate into the chromosphere and substantially affect the structure and dynamics of the solar atmosphere [Kitiashvili et al., 2012a].

Different source terms in the vorticity equation have been considered as possible candidates for enhancement of vorticity in the solar context. Non-magnetic simulations of turbulent convection show that vortex stretching can be a primary source for the generation of small-scale vorticity [Kitiashvili et al., 2012b]. The baroclinic term in the vorticity equation may lead to the formation of horizontally oriented vortex tubes [Steiner et al., 2010]: the gradients of pressure and density are close to vertical in the convection zone, so their cross product is mainly horizontally oriented. During this process the vortex tubes move into the intergranular lanes and become vertical due to convective downdrafts. The generation of the vortical flows observed by Bonet et al. [2008] has been attributed to compression: the downdraft acts as a sink and as the matter has angular momentum with respect to the draining point, it must spin up when approaching the sink, giving rise to a whirlpool also known as the bathtub drainage effect [Spurk and Aksel, 2008, page 358].

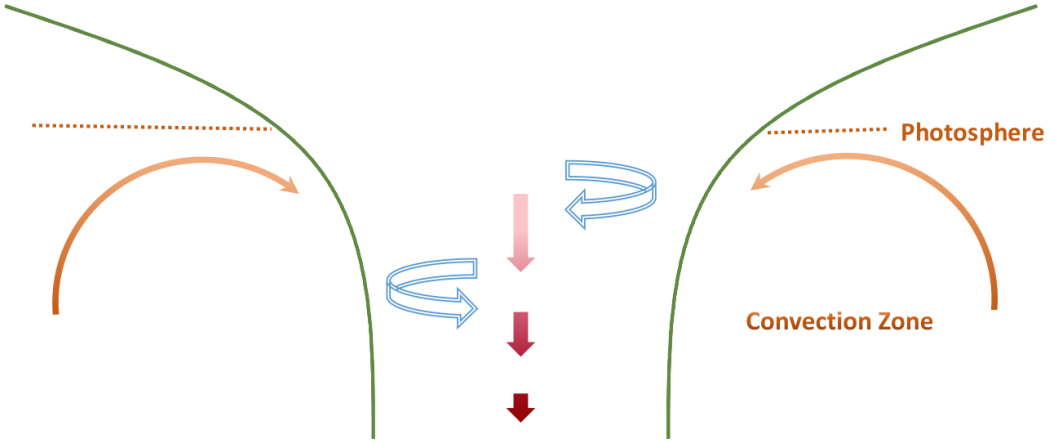

Figure 3.1: Cartoon representation of an intergranular downdraft (*red*) in a near-vertical flux tube (*green*). The tube is in a horizontal pressure balance with the surrounding convection zone, where the density increases with depth due to gravitational stratification. The red vertical arrows become shorter and darker as the downdraft slows down in the lower dense regions. Twisting motions of the tube are indicated with blue arrows.

The mechanisms described above are hydrodynamic in their nature. In the real Sun, interaction between vortices and ubiquitous magnetic fields is expected. Simulations of magnetoconvection usually begin with a weak, initially random [Moll et al., 2011] or uniform magnetic field [Stein and Nordlund, 2006]. Vortices with a small inclination appear mostly inside the integranular lanes where the downflows are strong. Horizontal flows advect the weak field and concentrate it in the turbulent downflow lanes where vortical motions are already well established.

One would expect stronger magnetic fields to have a stabilising influence on the turbulent flows and vortex motions. However, Shelyag et al. [2011] found that when the field strength rises to a few kilogauss in the intergranular lanes, small-scale vortices and torsional motions develop at the photospheric level that are co-spatial with these magnetic field concentrations. These small-scale motions are not seen in the non-magnetic model. They demonstrated that the vorticity

enhancement in the intergranular lanes was caused by a source term in the vorticity equation which contains magnetic tension.

Here, we describe how a downdraft may amplify twists of an ambient magnetic field. The theoretical mechanism behind the amplification process is the Alfvén instability introduced by Taroyan [2008]. In the following sections, we present the model and the conditions under which twists may become amplified. In §3.4, we tackle the problem analytically to find the continuous spectrum of eigenvalues and construct the eigenfunctions. A forcing term is introduced in §3.5 and the governing equations are integrated numerically to examine the spatio-temporal evolution in the linear regime. In §3.6, the energy source and the physical nature of the instability associated with the twist amplification are discussed.

3.3 Model and Governing Equations

3.3.1 Downdraft Model

A near-vertical segment of an expanding magnetic flux tube is embedded in a gravitationally stratified convection zone and permeated by a field-aligned downdraft as shown in Figure. (3.1). We assume that the plasma inside the tube remains in equilibrium with the surrounding medium.

The density in the convection zone increases with depth due to the gravitational stratification. If the magnetic field remains constant then the density inside the tube will have to increase with depth as well in order to sustain a horizontal total pressure balance. According to mass conservation, the downdraft speed is $u_0 = \text{const} \times c_A^2$, as the momentum and magnetic field are constant. $c_A = B_0/\sqrt{\mu_0 \rho_0}$ is the Alfvén speed defined as the ratio of the magnetic field and the square root of density with μ_0 being the permeability of free space. Note that the flow speed decreases more rapidly with depth than the Alfvén speed does.

The critical level where $u_0 = c_A$ corresponds to equipartition between the magnetic energy density, B_0^2/μ_0, and the kinetic energy density of the flow, $\rho_0 u_0^2/2$.

The equipartition level may not exist if the magnetic energy dominates the kinetic energy of the downdraft everywhere in the upper subphotospheric layers.

We adopt a cylindrical coordinate system, where z denotes depth and θ represents the azimuthal coordinate. In the thin flux tube approximation, the linear equations governing the motion of small axisymmetric twists are decoupled from the other MHD equations. These motions are governed by the azimuthal components of the equations of momentum and induction [Ferriz-Mas et al., 1989; Hollweg et al., 1982]:

$$\rho_0 \frac{Dv_\theta}{Dt} = \frac{B_0}{\mu_0} \frac{\partial b_\theta}{\partial z}, \tag{3.1}$$

$$\frac{Db_\theta}{Dt} = B_0 \frac{\partial v_\theta}{\partial z} - b_\theta \frac{\partial u_0}{\partial z}, \tag{3.2}$$

where b_θ, and v_θ denote the azimuthal perturbations of the magnetic field and velocity, with

$$\frac{D}{Dt} = \frac{\partial}{\partial t} + u_0 \frac{\partial}{\partial z}, \tag{3.3}$$

being the substantial derivative. Note that when θ is replaced by the Cartesian coordinate x, the same set of equations describes the propagation of shear Alfvén waves in a flowing plasma with a uniform magnetic field.

In the absence of an equilibrium flow ($u_0 = 0$), the set of equations (3.1) and (3.2) describes the propagation of incompressible Alfvén waves in a static medium. The waves result from the combined effects of the tension force (right hand side of equation (3.1)) and the plasma inertia (first term on the right hand side of equation (3.2)).[1]

The presence of a constant flow ($u_0 = \text{const}$) leads to a constant Doppler shift due to the added advection term in the substantial derivative (3.3).

[1] If the equations of §2 are linearised for a hydrostatic plasma then the same solution may also be obtained.

The last term on the right hand side of the induction equation (3.2) appears only when the equilibrium flow is variable. It represents the effects of compression or expansion of the plasma on the incompressible axisymmetric twists.

3.3.2 Twist Amplification: Analogy with Vortex Stretching

In a weak field, the Alfvén speed is small compared with the speed of the flow, and the inertial term in equation (3.2) can be ignored. This eliminates the variable, v_θ from the induction equation, so it can be rewritten as:

$$\frac{Db_\theta}{Dt} = -b_\theta \frac{\partial u_0}{\partial z}. \tag{3.4}$$

Therefore, expansion of the plasma ($\partial u_0/\partial z > 0$) corresponds to attenuation while compression ($\partial u_0/\partial z < 0$) corresponds to amplification of b_θ. From the preceding discussion it follows that the latter situation is more likely to occur in downdrafts.

Equation (3.4) looks remarkably similar to the vorticity equation for an incompressible fluid:

$$\frac{D\omega}{Dt} = \omega \frac{\partial u_0}{\partial z}, \tag{3.5}$$

where ω denotes vorticity in the z direction. The right hand side of equation (3.5) represents the well-known vortex stretching effect: the angular velocity of a vortex tube increases when it is stretched and decreases when it is compressed [Spurk and Aksel, 2008, page 100].

In contrast, equation (3.4) shows that the θ component of the magnetic field increases when the flow decelerates and decreases when it accelerates. The fact that the twist amplification stems from the induction equation emphasises the magnetic nature of the process. Twist amplification may be thought of as a magnetic analogue of vortex stretching.

In a more general situation, when the magnetic field is not weak, the twist evolution requires a more detailed treatment. In the following sections we study the twist amplification analytically as an eigenvalue problem and numerically as a linear system. We also discuss the energy source, and the physics of the amplification process.

3.4 Unstable Twists in an Exponentially Decaying Downdraft

The set of governing equations (3.1) and (3.2) can be reduced to a single second order PDE for the magnetic field perturbation, b_θ [Taroyan, 2008]:

$$\frac{\partial^2 b_\theta}{\partial t^2} + 2\frac{\partial^2}{\partial t \partial z}\left(u_0 b_\theta\right) + \frac{\partial}{\partial z}\left(u_0 \frac{\partial}{\partial z}\left(\frac{u_0^2 - c_A^2}{u_0} b_\theta\right)\right) = 0, \tag{3.6}$$

where $u_0 = u_0(z)$, and $c_A = c_A(z)$. In deriving the above equation, we have used the equation of mass conservation. In a static medium with $u_0 = 0$, the well-known wave equation can be derived from equations (3.1) and (3.2):

$$\frac{\partial^2 b_\theta}{\partial t^2} = \frac{\partial}{\partial z}\left(c_A^2 \frac{\partial b_\theta}{\partial z}\right). \tag{3.7}$$

Equation (3.7) was first analysed by Ferraro [1954] in the context of Alfvén wave propagation in the solar atmosphere. Solutions in terms of the Bessel functions were constructed for an isothermal atmosphere with an exponential density profile:

$$\rho_0 = \rho_0(0) \exp\left(\frac{z}{z_0}\right), \tag{3.8}$$

where z_0 is the scale height. The corresponding Alfvén speed is given by:

$$c_A = c_A(0) \exp\left(-\frac{z}{2z_0}\right). \tag{3.9}$$

Note that in our notations z denotes depth. Equation (3.7) with the profile (3.8) was subsequently analysed by different authors. They found standing wave solutions in terms of the Bessel functions [An et al., 1989; Ferraro, 1954] or propagating wave solutions in terms of the Hankel functions [Cally, 2012; Hollweg, 1978] depending on the imposed boundary conditions.

An advantage of the smooth exponential profile is the absence of any model dependent artificial reflections that may arise due to discontinuities in the Alfvén speed or its derivatives [Cally, 2012]. One of the drawbacks is the finite Alfvén travel time to $z = -\infty$ [An et al., 1989].

In studies of the convection zone, it is common to adopt a polytrope with a linear temperature. Here, we adopt the exponential profiles (3.8) and (3.9) with a given scale height, z_0. This approach allows us to compare our results with those already known from studies of Alfvén wave propagation in a stratified and static environment. Conservation of mass requires that the downdraft speed diminishes as:

$$u_0 = u_0(0) \exp\left(-\frac{z}{z_0}\right), \tag{3.10}$$

provided the tube radius remains constant. We will see that the problems associated with the finite travel time to $z = -\infty$ are no longer relevant because the downdraft prevents propagation into the super-Alfvénic region.

The temperature represented by the square of the sound speed, $c_s^2 = \gamma p_0/\rho_0$, can be determined from the equilibrium equation of motion:

$$u_0 \frac{du_0}{dz} = -\frac{1}{\rho_0}\frac{dp_0}{dz} + g - \mathcal{F}, \tag{3.11}$$

where p_0 is thermal pressure, g is the gravitational acceleration, and $\mathcal{F}$ is a general force term which vanishes at $z = \infty$. Integration of equation (3.11) yields:

$$c_s^2 = c_0^2 + \frac{\gamma}{\rho_0}\int_0^z \rho_0 \left[\frac{c_\infty^2}{\gamma z_0} - \mathcal{F} - u_0\frac{du_0}{dz'}\right] dz', \tag{3.12}$$

where $c_0^2 = c_s(0)^2$, and $c_\infty^2 = g\gamma z_0$ is the limit of c_s^2 at $z = \infty$. Thus, in contrast to a static force-free model, the sound speed is no longer a constant. Instead, the behaviour of the sound speed and temperature will depend on the prescribed values for c_0 and c_∞.

The coefficients in the governing equation (3.6) are expressed through the Alfvén and flow speeds. Therefore, in the linear regime, the twist evolution does not depend on the temperature profile and the subsequent analysis is carried out without specifying the values of c_0 and c_∞.

Equation (3.6) is Fourier analysed and the result is the following ODE:

$$\frac{d}{dz}\left(u_0\frac{d}{dz}\left(\frac{u_0^2 - c_A^2}{u_0}\hat{b}_\theta\right)\right) - 2i\omega\frac{d}{dz}\left(u_0\hat{b}_\theta\right) - \omega^2\hat{b}_\theta = 0, \tag{3.13}$$

where

$$b_\theta = \hat{b}_\theta \exp(-i\omega t). \tag{3.14}$$

The equipartition level where $u_0 = c_A$ represents a singularity in equation (3.13). For simplicity we set this level at $z = 0$, so that $u_0(0) = c_A(0)$. It separates the upper super-Alfvénic region, $z < 0$, from the lower sub-Alfvénic region, $z > 0$.

For small wavelengths, $\lambda \ll z_0$, away from the singularity at $z = 0$, local phase speeds $u_0 \pm c_A$ can be introduced. The plus sign corresponds to propagation in the positive direction. The minus sign represents propagation in the negative direction in the sub-Alfvénic region ($z > 0$) and propagation in the positive direction when the flow is super-Alfvénic ($z < 0$). Thus, in contrast to the static model, any perturbation in the super-Alfvénic region will be swept down into the sub-Alfvénic region without being able to reach $z = -\infty$.

We introduce a dimensionless variable:

$$\tau = \left(\frac{c_A}{u_0}\right)^2 = \exp\left(\frac{z}{z_0}\right), \tag{3.15}$$

so that, $\frac{d}{dz} = \frac{\tau}{z_0}\frac{d}{d\tau}$, and transform equation (3.13) into:

$$(\tau - 1)\frac{d^2w}{d\tau^2} + (1-\nu)\frac{dw}{d\tau} - \frac{1}{4}(1+\nu)^2 w = 0, \tag{3.16}$$

where $\hat{b}_\theta = \tau\, w$, and

$$\nu = -1 - \frac{2i\omega z_0}{u_0(0)}. \tag{3.17}$$

The regular singularity at $\tau = 1$ corresponding to $z = 0$ requires separate treatment for $z > 0$ ($\tau > 1$) and $z < 0$ ($0 < \tau < 1$).

We show in the Appendix that the finite solution in the region $z > 0$ can be represented in terms of the modified Bessel function K_ν:

$$\hat{b}_\theta = C \exp\left(\frac{z}{z_0}\right) x^\nu K_\nu(x), \tag{3.18}$$

where

$$x = (\nu+1)\sqrt{\exp\left(\frac{z}{z_0}\right) - 1}, \tag{3.19}$$

and

$$C = \frac{\hat{b}_\theta(0)}{2^{\nu-1}\Gamma(\nu)}, \tag{3.20}$$

with $\Re(\nu) > 0$. According to the definition (3.17) of ν, a positive value of $\Re(\nu)$ corresponds to a positive value of $\Im(\omega)$, i.e., exponential growth in time. The growth rate is determined by the expression

$$\Im(\omega) = -\frac{1+\Re(\nu)}{2}\left[\frac{du_0}{dz}\right]_{z=0}. \tag{3.21}$$

Therefore, a finite solution to equation (3.13) corresponds to an instability ($\Im(\omega) > 0$). Note that solutions exist for arbitrary ν with positive $\Re(\nu)$ and the spectrum of eigenvalues is continuous. It is well-known that if the coefficients of the differential equation are singular at the boundary or if the interval is infinite then the spectrum of eigenvalues is continuous and a Fourier integral replaces the linear combination of the eigenfunctions [Courant and Hilbert, 1966, page 340]. In the

present problem, the interval extends from $z = 0$ to ∞ and there is a singularity at $z = 0$.

The existence of the instability is not affected by the flow behaviour in the region $z < 0$. However, for completeness we construct the solution in the super-Alfvénic region assuming that the flow profile is determined by equation (3.10). The finite solution in the region $z < 0$ is expressed in terms of the Bessel functions J_ν, Y_ν (see Appendix B, §5):

$$\hat{b_\theta} = \tilde{x}^\nu \exp\left(\frac{z}{z_0}\right) \left[C_1 J_\nu(\tilde{x}) + C_2 Y_\nu(\tilde{x})\right], \tag{3.22}$$

where

$$\tilde{x} = (\nu + 1)\sqrt{1 - \exp\left(\frac{z}{z_0}\right)}, \tag{3.23}$$

$$C_2 = -\frac{\pi \hat{b}_\theta(0)}{2^\nu \Gamma(\nu)}, \tag{3.24}$$

$$C_1 = \frac{(\nu-1)Y_\nu(\nu+1) - (\nu+1)Y_{\nu-1}(\nu+1)}{(\nu-1)J_\nu(\nu+1) - (\nu+1)J_{\nu-1}(\nu+1)} C_2. \tag{3.25}$$

The coefficient C_1 is derived assuming that v_θ vanishes at $z = -\infty$ due to the super-Alfvénic flow.

Figure. (3.2) displays $\hat{b}_\theta$ as a function of z and ν, where the normalisation $\hat{b}_\theta(0) = 1$ is applied. For simplicity, only real and positive values of ν corresponding to purely imaginary ω are considered. The corresponding eigenfunction shown in Figure. (3.2) is also real. Note that the maximum of $\hat{b}_\theta$ moves away from the equipartition level ($z = 0$) as ν increases.

Our analysis of the eigenvalue problem reveals the existence of an instability: small axisymmetric twists are exponentially amplified in a downdraft that exponentially decays with depth.

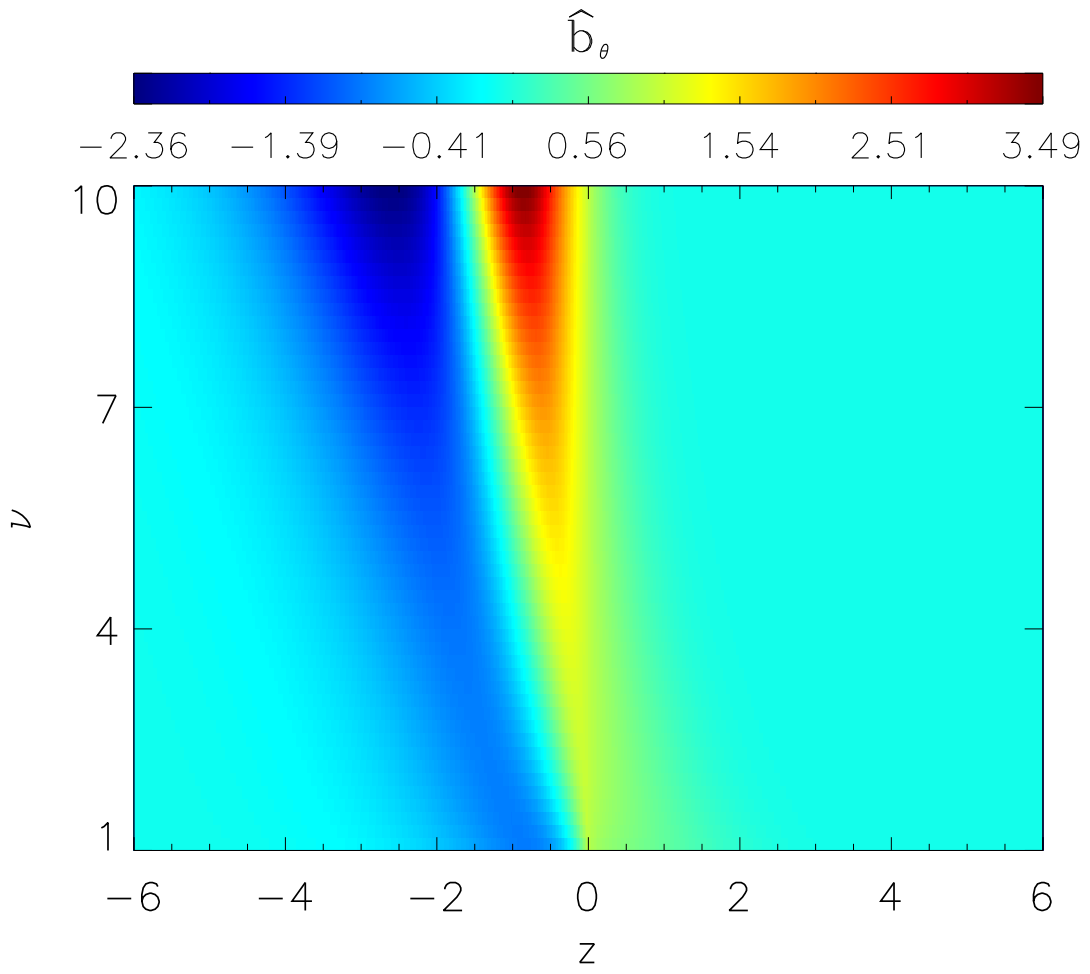

Figure 3.2: A plot of $\hat{b}_\theta$ as a function of z and ν, where the normalisation $\hat{b}_\theta(0) = 1$ is applied. The colour bar indicates the magnitude and the sign of $\hat{b}_\theta$. Only real and positive values of ν corresponding to purely imaginary ω and real $\hat{b}_\theta$ are considered.

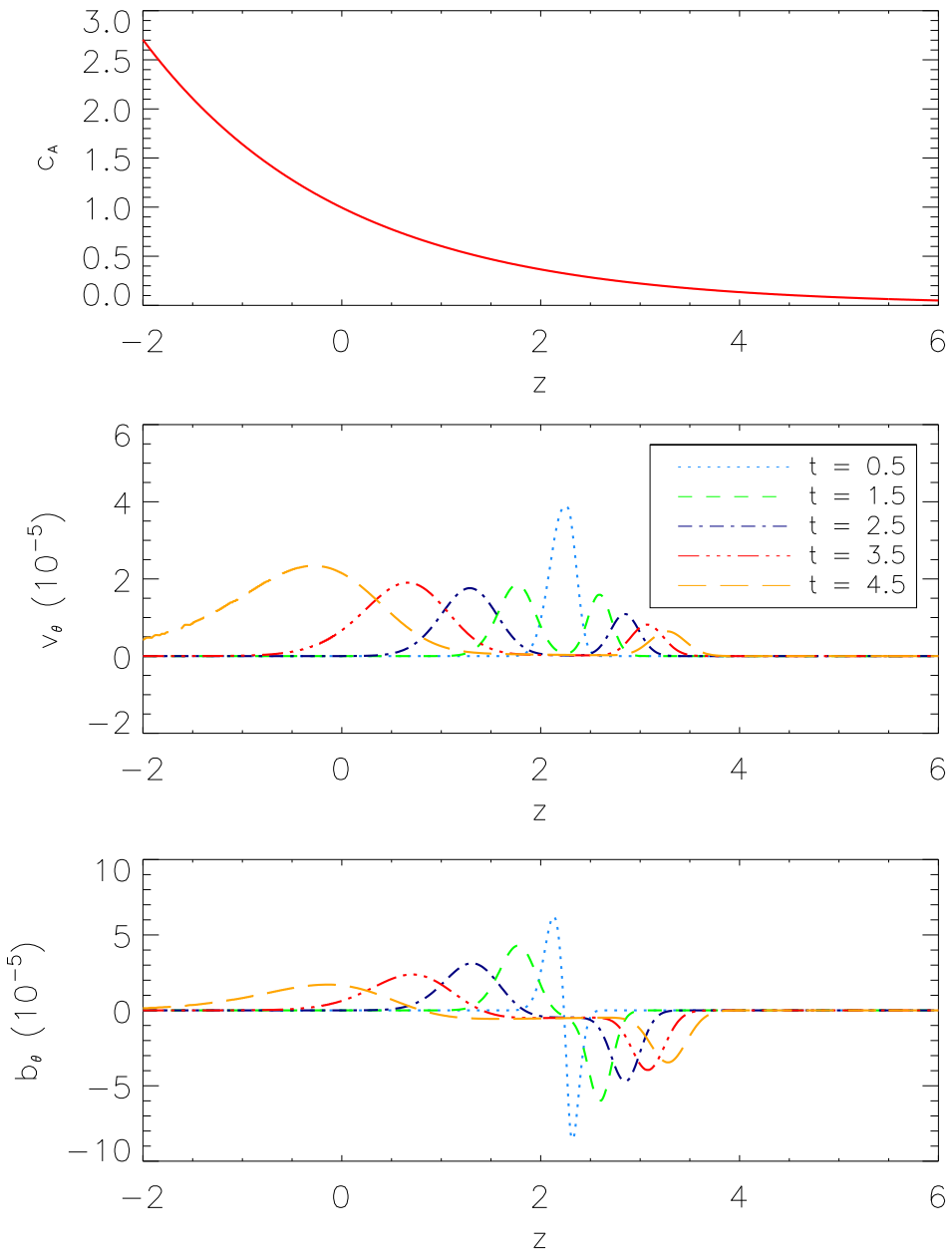

Figure 3.3: *Top*: Alfvén speed profile within a vertically stratified flux tube with no flow. *Middle*: v_θ velocity distribution for time 0.5 to 4.5. *Bottom*: the corresponding b_θ profile.

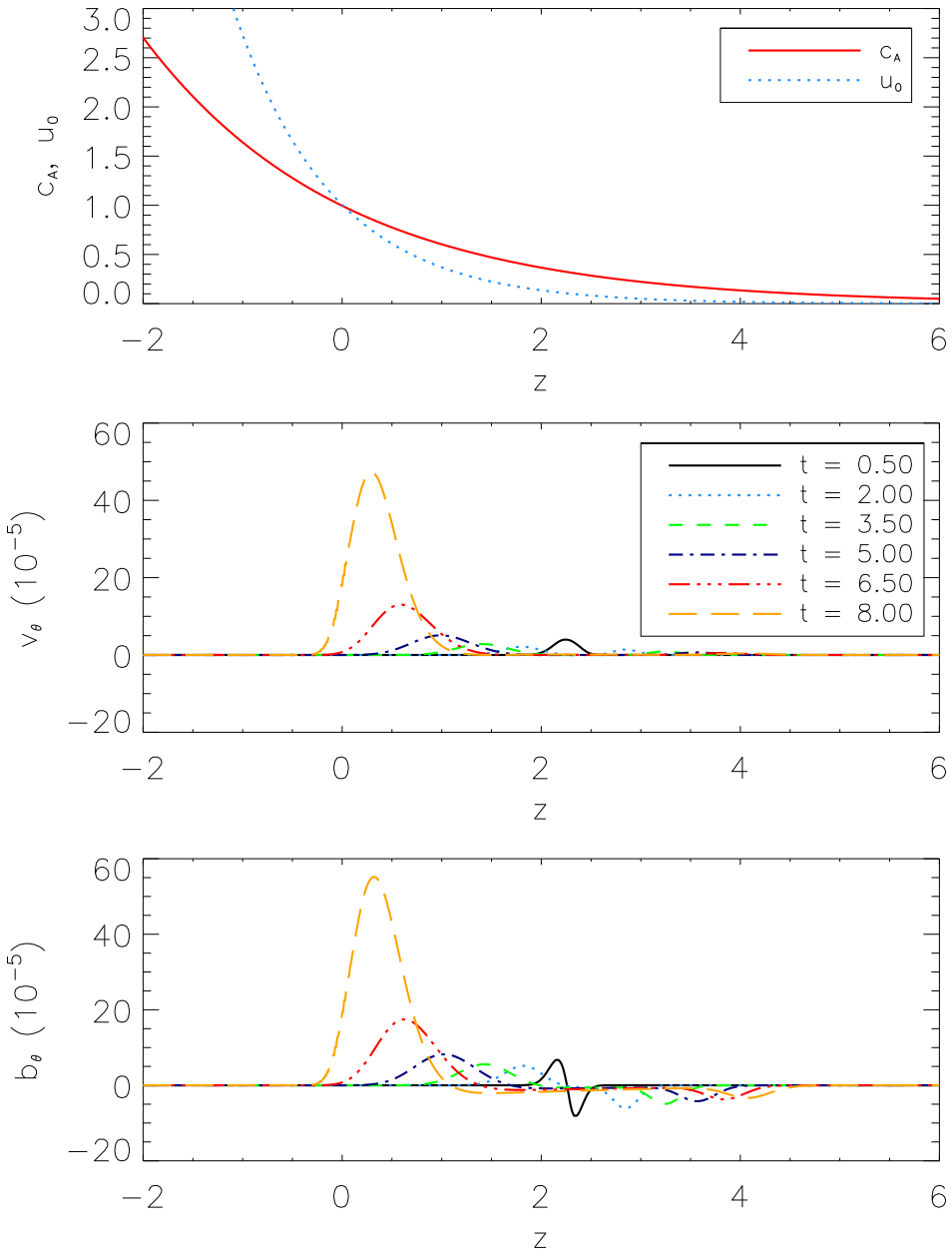

Figure 3.4: *Top*: Alfvén speed and flow-speed profiles within the modelled downdraft. The critical point $c_A(0) = u_0(0)$ can be seen clearly at $z = 0$ where the two plots intersect one another. *Middle*: v_θ velocity distribution for time 0.5 to 8. *Bottom*: the corresponding b_θ profile.

3.5 The Spatio-Temporal Evolution of the Instability

In this section, the evolution of a single twist is presented with two circumstances investigated. Both scenarios launch a single Alfvénic pulse from within the lower sub-Alfvénic part of the flux tube. However, the first case involves a static plasma with an exponential density profile (3.8), whereas the second case incorporates a downflow defined by equation (3.10).

Equations (3.1) and (3.2) are numerically integrated using the flux-corrected transport scheme [Boris et al., 1993]. A uniform grid is used which contains 1700 grid-points. The domain is extended in such a way that the boundaries are sufficiently far away from the region of interest as not to interfere with the simulations. The critical point where the flow changes from super-Alfvénic to sub-Alfvénic is situated at $z = 0$. The extension of the domain also means that any reflections or change in behaviour of the perturbations is purely down to physical mechanisms, such as Alfvén speed variation, and is not a numerical implication caused from a boundary region.

In what follows, length, speed and magnetic field are normalised with respect to the scale length, z_0, the Alfvén speed $c_A(0)$, and the equilibrium magnetic field B_0, respectively.

A smooth driver which describes a small-amplitude perturbation is added to the right hand-side of equation (3.1) as a source term, F:

$$F = \frac{A}{\rho_0} \sin^2\left(\pi \frac{t - t_{min}}{t_{max} - t_{min}}\right) \sin^2\left(\pi \frac{z - z_{min}}{z_{max} - z_{min}}\right). \tag{3.26}$$

Here, A is amplitude, t is time normalised with respect to $z_0/c_A(0)$, where $t_{min} = 0$ and $t_{max} = 0.5$ are the start- and end-times for which the driver is active. Similarly, $z_{min} = 2$ and $z_{max} = 2.3$ are the start- and end-points within the tube where the driver is active.

An exponentially decreasing profile is generated for the Alfvén speed (Figure. 3.3: Top panel) with the plasma in a static equilibrium. A single twist is launched which separates into upward (negative direction) and downward (positive direction) propagating pulses (Figure. 3.3: Middle and Bottom panels). The upward propagating pulse has an increasing amplitude in the velocity perturbation and a decreasing amplitude in the magnetic field perturbation. Note that the kinetic energy remains finite due to the density decrease with height. This behaviour is well-known from studies of Alfvén wave propagation in stratified media [Cally, 2012].

The downward propagating pulse is impeded by the ever-diminishing Alfvén speed in the positive direction. The twist is not reflected due to the smooth equilibrium profile and its propagation comes to a virtual standstill until it is lost to the background plasma as the Alfvén speed approaches 0.

The introduction of a plasma flow yields some interesting results (Figure. 3.4). The initial pulse is launched from within the flux tube and splits into two pulses that propagate in opposite directions, much like what is seen in the static case. The pulse that travels in the positive direction behaves identically to that seen in Figure. (3.3). That is, the propagation of the pulse stalls with the v_θ and b_θ amplitudes decreasing until they are eventually lost to the background.

The pulse that propagates upward in the negative direction behaves somewhat similarly to the pulse in Figure. (3.3). However, unlike the static case, both b_θ and v_θ increase in amplitude as they propagate. As the pulse approaches the critical point, $z = 0$, the propagation virtually ceases with v_θ and b_θ continually amplifying (Figure. 3.4: Middle and Bottom panels). This situation is allowed to arise due to the propagation speed $c_A - u_0$ gradually approaching 0. Using the expressions for the Alfvén and the flow speeds it can be shown that the travel time to $z = 0$,

$$t_A = \int_0^z \frac{dz'}{c_A - u_0}, \tag{3.27}$$

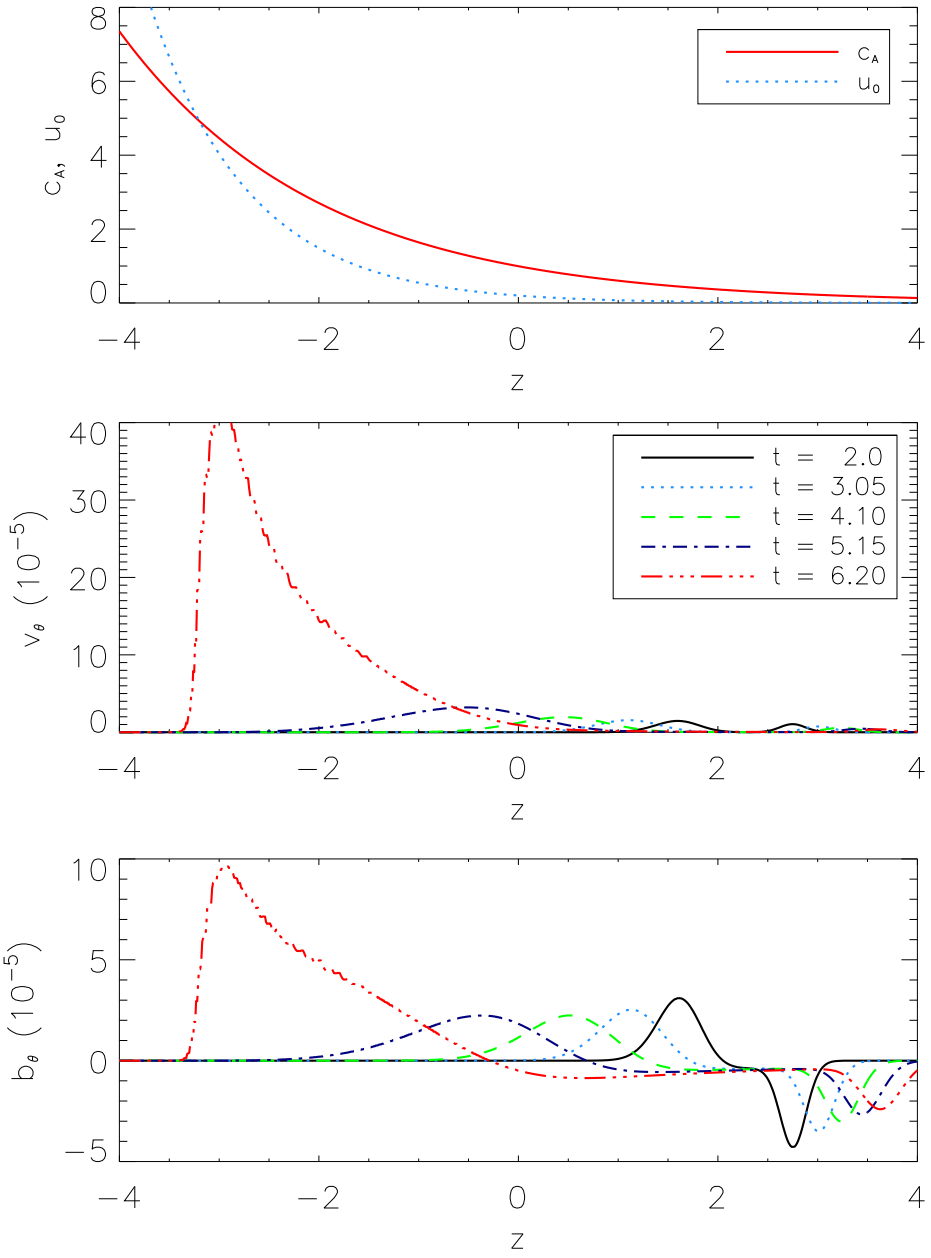

Figure 3.5: Same as Figure. (3.4) but with $u_0(0) = 0.2 \times c_A(0)$.

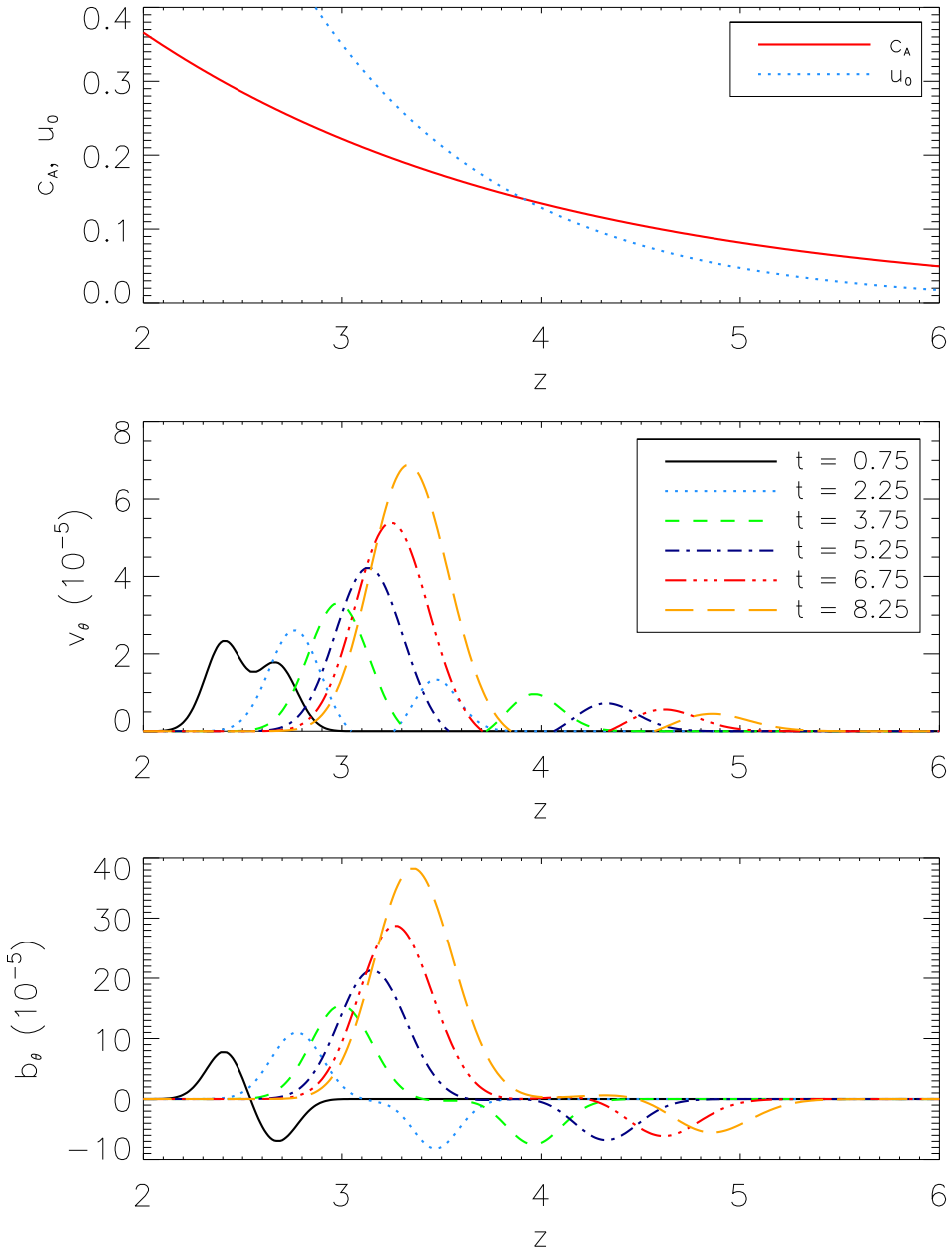

Figure 3.6: Same as Figure. (3.4) but with $u_0(0) = 7 \times c_A(0)$.

is infinite. The pulse propagation does not extend to the super-Alfvénic region and the twist amplification is therefore unaffected by the flow profile in the region above the equipartition height. The pulse amplification in the vicinity of $z = 0$ confirms the instability found in the preceding section.

Figure. (3.5) displays the twist evolution when the downdraft speed is much smaller than the Alfvén speed at $z = 0$. The downward propagating component damps as in the previous cases. It is interesting that the upward propagating b_θ component initially attenuates before it begins to grow in the vicinity of the equipartition height at around $z = -3$. Therefore growth does not occur away from the equipartition height in the sub-Alfvénic region. Nevertheless, the downdraft maintains a twist which is larger than the static case (Figure. 3.3).

In Figure. (3.6), a ratio $u_0(0)/c_A(0)$ of 7 is taken. This is unlikely to occur in the real Sun. However, Figure. (3.6) is still instructive as it shows the spatio-temporal evolution of a twist when the source term is located in the super-Alfvénic region. Both the upward and downward propagating components are swept down towards the sub-Alfvénic region by a strong downdraft. The downward propagating component quickly escapes into the sub-Alfvénic region with subsequent attenuation by the tension force. The upward propagating component, on the other hand, grows as it approaches the equipartition level at around $z = 4$. It never reaches the sub-Alfvénic region because the local propagation speed $u_0 - c_A$ becomes small in the vicinity of $z = 4$. The associated travel time to $z = 0$ is determined analogous to equation (3.27) and it is therefore infinite.

3.6 Energy Considerations and the Physics of Twist Amplification

In fluid dynamics, the process of wave shoaling is well-known [Wiegel, 1992, page 150]. When a tsunami approaches the shallower coastal water the leading edge slows down while the trailing part is still moving rapidly in the deeper water. As a consequence, the wavelength decreases proportionally to the group speed of the

wave. This compression of the tsunami leads to a pileup and growth in the wave height.

The presented mechanism might seem to be a magnetic analogue of the wave shoaling process due to a similar decrease in the propagation speed $c_A - u_0$ when the wave approaches the equipartition level. However, the Fourier analysis applied in §3.4 reveals the presence of an instability ($\Im(\omega) > 0$). According to equations (3.14) and (31; Appendix B), the exponential growth proportional to $\exp(\Im(\omega)t)$ occurs globally in z and not just near the equipartition level.

Similarly, the analysis of the spatio-temporal evolution of a driven pulse carried out in Section 4 shows a reduction in the travel speed as the pulse approaches the equipartition level but no corresponding decrease in the wavelength (Figures. 3.4-3.6). An evanescent tail can be seen to extend into the super-Alfvénic region in Figure. (3.4) and into the sub-Alfvénic region in Figure. (3.6) as the pulse grows in amplitude. Therefore, the physics of wave shoaling is different from that of the twist amplification process presented in this study.

In order to gain a physical insight into the process of amplification and to identify the source of wave energy, we derive the following equation of wave energy (see Appendix B, §5):

$$\frac{\partial W_T}{\partial t} + \frac{\partial F_W}{\partial z} = -\frac{\partial u_0}{\partial z} W_m, \tag{3.28}$$

where W_T is the sum of the kinetic and magnetic energy densities:

$$W_T = W_k + W_m = \frac{\rho_0 v_\theta^2}{2} + \frac{b_\theta^2}{2\mu_0}, \tag{3.29}$$

and

$$F_W = u_0 W_T - \frac{B_0}{\mu_0} v_\theta b_\theta, \tag{3.30}$$

is the total wave energy flux. The second term in equation (3.30) is the energy flux in the absence of a flow, and the first term is the flow contribution. The right hand side of equation (3.28) represents a source term which is present due to the wave-flow coupling. Note that this term is absent when the flow is constant.

The non-linear coupling between the Alfvénic and longitudinal motions due to the magnetic pressure term in the longitudinal momentum equation is well known. Equation (3.28) demonstrates coupling of a decelerating flow ($\partial u_0/\partial z < 0$) to Alfvénic twists. This allows the flow's kinetic energy to be converted into magnetic twists in the linear regime. In this case, the right hand side of equation (3.28) acts as a source of energy. Conversely, in an accelerating flow ($\partial u_0/\partial z > 0$) the right hand side of equation (3.28) acts as a sink of energy.

The evolution of the total energy, W_T is determined by the relative magnitudes of flux divergence and the source term. In regions where the flow speed gradient is small, the twist evolution is determined by the second term in equation (3.28). Flux divergence ($\partial F_W/\partial z > 0$) leads to twist attenuation and loss of energy, W_T. Flux convergence ($\partial F_W/\partial z < 0$), on the other hand, leads to amplification and an energy increase. However, the twist amplification in one region is accompanied by attenuation in a different region. An example of amplification due to flux convergence is the wave shoaling process discussed above. The situation is different in regions where the gradient of the decelerating flow is large enough to determine the evolution through the source term. In this case, the twist growth is not accompanied by shrinking, which is in agreement with the presented results.

Figure. (3.7) is a schematic representation of the wave-flow coupling in a decelerating downdraft: the descending plasma (*red*) amplifies and transfers energy into a twisted field line (*green*). The energy flux is small and the pulse evolution is mainly determined by the source term when the propagation is against the flow. A constant flow will have no effect on the twist except a constant Doppler shift, whereas an accelerating flow will smooth out any perturbations in the magnetic field.

It is possible to show that the total wave energy content grows due to the wave-

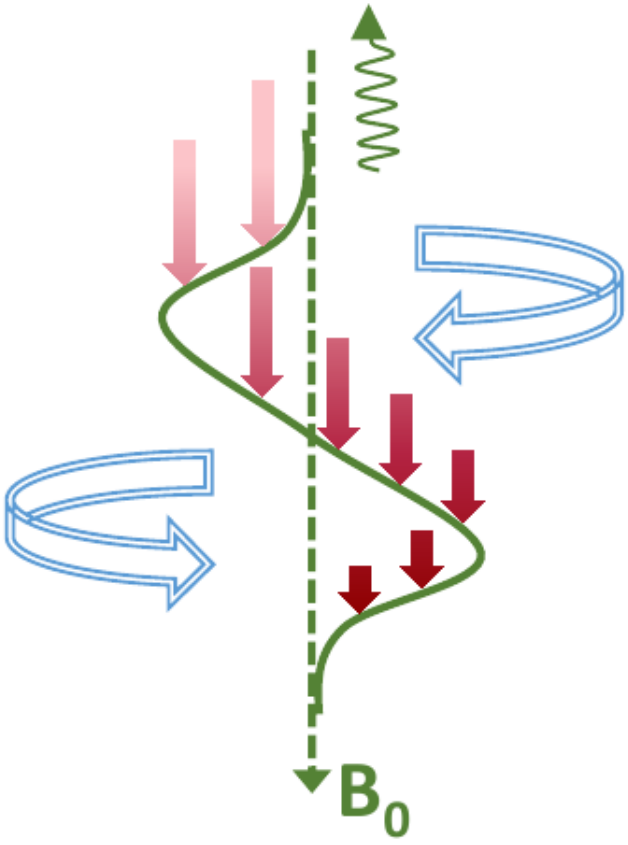

Figure 3.7: Twist amplification due to coupling with a decelerating flow. Propagation is in the direction opposite to the flow. Note, however, that an upward propagating twist will be swept down by the flow in the super-Alfvénic region.

flow coupling. The integral of equation (3.28) is:

$$\frac{\partial E_T}{\partial t} + F_W(\infty) - F_W(-\infty) = -\int_{-\infty}^{\infty} \frac{\partial u_0}{\partial z} W_m dz, \tag{3.31}$$

where

$$E_T = \int_{-\infty}^{\infty} \left[\frac{\rho_0 v_\theta^2}{2} + \frac{b_\theta^2}{2\mu_0} \right] dz. \tag{3.32}$$

Firstly, $F_W(\infty) = 0$ due to vanishing b_θ and v_θ at $z = \infty$. Secondly, the boundary condition we have imposed on v_θ to vanish at $z = -\infty$ implies zero flux at $z = -\infty$: indeed it is easy to check that $u_0 b_\theta^2 = 0$ at $z = -\infty$ and therefore $F_W(-\infty) = 0$.

The integrand on the right hand side of equation (3.31) is finite everywhere. Using equation (39; Appendix B) it is easy to check that it decreases exponentially when $z \to -\infty$. Similarly equation (31; Appendix B) can be used to show that the integrand is bounded by an exponentially decreasing function when $z \to \infty$. Therefore the integral on the right hand side of equation (3.31) is convergent. We obtain:

$$\frac{\partial E_T}{\partial t} = -\int_{-\infty}^{\infty} \frac{\partial u_0}{\partial z} W_m dz > 0. \tag{3.33}$$

Therefore, the total wave energy grows due to coupling with the flow along the tube.

3.7 Conclusions

We have analysed the behaviour of magnetic twists in the presence of intergranular downdrafts. The analysis is carried out in the thin flux tube approximation. It is shown that small twists become amplified if the descending plasma decelerates with depth. The deceleration leads to amplification of the twists as shown in Figure. (3.7). In § 3.3, we argue that the presented mechanism can be thought of as a magnetic analogue of vortex stretching.

A detailed analysis is carried out for an exponential flow profile. Analytical solutions representing a spectrum of unstable modes are constructed. The instability only exists for a negative flow gradient.

The spatio-temporal evolution of the instability is examined and compared for different ratios of $u_0(0)/c_A(0)$. The flow continually amplifies a magnetic twist as its propagation grinds to a halt in the vicinity of the equipartition level. The amplification is caused by the interaction between the twisted magnetic field and the decelerating flow. An upward propagating twist in the sub-Alfvénic region is not affected by the flow profile above the equipartition level. The super-Alfvénic flow may even become sub-Alfvénic above a certain height without affecting the twist evolution. Therefore the process of twist amplification does not require unrealistically high speed flows at high altitudes.

The present study was mainly confined to exponential velocity and density profiles with an arbitrary scale height. There is no reason why the instability should not arise for other smooth profiles. We have shown that the total azimuthal wave energy content grows for arbitrary decelerating flow profiles if there is no wave energy flux through the boundaries. For a given location, the twist dynamics is determined by the competing effects of the flow gradient and the energy flux divergence. The amplification is most efficient in the vicinity of the equipartition level, where the propagation stalls and the dynamics are dominated by the transfer of the flow energy into the twisting motions.

We make some simple estimates to assess the applicability of the presented amplification mechanism. The Alfvén speed can be expressed as $c_A = 2.8 \times 10^{12}\, B_0\, n^{-\frac{1}{2}}$ m s^{-1}, where n denotes the number density in m^{-3} and B is measured in Gauss [Priest, 2014, page 487]. For a photospheric number density of 10^{23} m^{-3} and a field strength of 1 kG we find $c_A = 8.86$ km s^{-1}, which is within the range of downflow speeds mentioned in the Introduction (§ 3.2). Therefore, an equipartition is likely to occur at the photospheric level.

In practice, solar flux tubes are highly inhomogeneous, dynamic and time-varying and these estimates should be taken with caution. A more detailed numerical analysis accounting for the temporal and spatial variability of the downdraft in a realistic convection zone is needed. It is likely that a compressive downdraft which lasts longer than the growth timescale of $z_0/u_0(0)$ will produce vortex motions. A short-lived downdraft, on the other hand, will have the effect of drawing a bowstring: the twists will be amplified and will begin to propagate up along the field lines upon release.

In turbulence dynamics, the enhancement of vorticity by stretching is argued to be the most important mechanism by which energy is transferred to small scales. Based on the analogy we have drawn between the vortex stretching and the magnetic twist amplification effects it is tempting to argue that the presented mechanism may play an important role in the energy transfer to small scales with subsequent heating in the solar atmosphere. However, a detailed analysis is required before any conclusions can be made.

3.8 The Non-Linear Evolution of an Alfvén Wave in a Downflow

As we are now moving to a non-linear study, it is necessary to transition from LCPFCT to a more robust library such as VAC. If the reader recalls in the previous chapter (§2), LCPFCT has issues with steep gradients or discontinuities and Gibbs' oscillations would arise under such circumstances. It is expected that as the Alfvén waves amplify sufficiently to become non-linear that the torsional variables will couple to the longitudinal variables and produce shocks. For the benefit of the reader, the governing 1.5-D MHD equations are shown once again below, though the extra source terms that describe gravity are now included so that:

$$\frac{\partial \rho}{\partial t} + \frac{\partial}{\partial z}\left(v_z \rho\right) = 0, \tag{3.34}$$

$$\frac{\partial}{\partial t}\left(\rho v_z\right) + \frac{\partial}{\partial z}\left(v_z \rho v_z\right) = -\frac{\partial}{\partial z}\left(p_{tot}\right) + \rho \mathbf{g}, \tag{3.35}$$

$$\frac{\partial}{\partial t}\left(\rho v_\theta\right) + \frac{\partial}{\partial z}\left(v_z \rho v_\theta\right) = \frac{B_z}{\mu_0}\frac{\partial}{\partial z}\left(B_\theta\right), \tag{3.36}$$

$$\frac{\partial e}{\partial t} + \frac{\partial}{\partial z}\left(v_z e\right) = \frac{B_z}{\mu_0}\frac{\partial}{\partial z}\left(v_z B_z + B_\theta v_\theta\right) - \frac{\partial}{\partial z}\left(v_z p_{tot}\right) + \rho \mathbf{g} \cdot \mathbf{v}, \tag{3.37}$$

$$\frac{\partial B_\theta}{\partial t} + \frac{\partial}{\partial z}\left(v_z B_\theta\right) = \frac{B_z}{\mu_0}\frac{\partial}{\partial z}\left(v_\theta\right), \tag{3.38}$$

where

$$p_{tot} = \frac{1}{2}\mathbf{B}^2 + p, \tag{3.39}$$

and

$$p = (\gamma - 1)\left(e - \frac{1}{2}\rho \mathbf{v}^2 - \frac{1}{2}\mathbf{B}^2\right). \tag{3.40}$$

Again, it is worth noting that $\mathbf{B} = B_z\mathbf{e_z} + B_\theta \mathbf{e}_\theta$, $\mathbf{v} = v_z\mathbf{e_z} + v_\theta \mathbf{e}_\theta$, and $\mathbf{g} = g_z\mathbf{e_z} + g_\theta \mathbf{e}_\theta = \{1, 0\}$.

3.8.1 Issues With Gravity and Boundary Conditions

In this subsection, the issues encountered due to boundary regions and gravity are discussed. Initially, due to the variables ρ, v_z and p being non-constant and the implementation of non-optimal boundary conditions, the flow profile is destroyed by mass movement. This is minimised for the top boundary using the fixed1 condition, which is specified in the VAC manual [Tóth, 1997] as taking the initial gradient and then fixing the ghost cells to this value. However, there are a couple of issue with this. The first issue is, this does not constrain the perturbation seen near the bottom boundary, which propagates up the flux tube and decimates the downflow (Figure 3.8). The other issue would arise if any non-linear waves were introduced near the boundary: they would become reflected as if a Dirichlet-type boundary were employed.

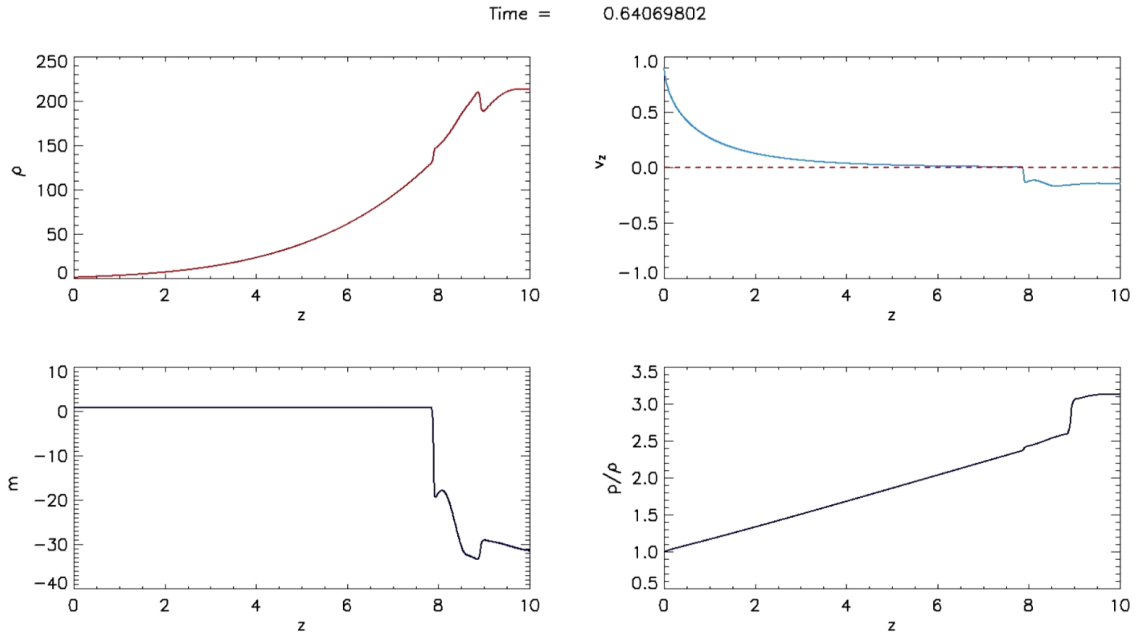

Figure 3.8: Panels (*clockwise*) show density, velocity, temperature, and momentum. This shows that the fixed1 boundary type constrains the flow profile at $z = 0$ from altering, and how the momentum is perturbed at the bottom, $z = 10$ boundary, which eventually decimates the flow.

In an attempt to combat these issues, gravity is smoothed at the two boundary regions by using the cubic function so that:

$$g(z) = \begin{cases} 0, & \text{if } 0 \leq z \leq z(0) \text{ or } z(\chi) \leq z \leq 10 \\ \frac{g}{2} + \frac{g}{4} \times \left(\frac{2z - z(\delta)}{z(\delta) - z(0)}\right) \left[3 - \left(\frac{2z - z(\delta)}{z(\delta) - z(0)}\right)^2\right], & \text{if } z(0) < z < z(\delta) \\ 1, & \text{if } z(\delta) \leq z \leq z(\sigma) \\ \frac{g}{2} - \frac{g}{4} \times \left(\frac{2z - z(\chi)}{z(\chi) - z(\sigma)}\right) \left[3 - \left(\frac{2z - z(\chi)}{z(\chi) - z(\sigma)}\right)^2\right], & \text{if } z(\sigma) \leq z \leq z(\chi) \end{cases} \tag{3.41}$$

where $z(0) = 0.15$, $z(\delta) = 0.5$, $z(\sigma) = 9.5$, and $z(\chi) = 9.85$. This allows the use of open boundary conditions at the two boundary locations as VAC will numerically adjust an analytical profile to be constant in the regions of zero gravity, with any perturbations propagating out of the modelled flux tube. Thus, any analytical equilibrium that satisfies the VAC MHD equations should be conserved during advection (where $g(z) = 1$) and any twist perturbation that reaches these regions will merely propagate out of the modelled flux tube.

However, whilst a downflow profile is obtained from this method, the initial conditions provided to VAC are not perfectly conserved. The flow gradient in the region of interest becomes small with the maximum speed being unrealistically low for processes such as convective collapse. That said, such a profile still provides valuable insight as to what might occur under similar conditions.

3.8.2 Generating Equilibria

To obtain a flow profile which satisfies both the energy and momentum equations within VAC, we use Newton's method for root finding to solve the desired profile,

$$\frac{X^2}{2} - \frac{v_0^2}{2} + \frac{1}{(\gamma - 1)} \left[\left(\frac{v_0}{X}\right)^{\gamma - 1} - 1\right] - \frac{z}{\lambda}, \tag{3.42}$$

where $\lambda = c_s^2(0) \;/\; g$. For this, we provide an initial guess as to the flow magnitude at $z = 0$ of v_0. The method then finds the root(s) of the equation, X using successively better approximations. The value of the root is then taken as the ini-

tial guess for the next gridpoint until all values of z have a corresponding root, X.

The profile obtained is then used to calculate the density and pressure profiles by:

$$\rho = \frac{\rho\left(0\right) v_z\left(0\right)}{v_z}, \tag{3.43}$$

and

$$p = p\left(0\right)\left(\frac{v_z\left(0\right)}{v_z}\right)^{\gamma}, \tag{3.44}$$

where $\rho\left(0\right) = 1$ and $p\left(0\right) = \frac{c_s^2(0)\rho(0)}{\gamma}$. These are then fed into VAC as initial conditions and allowed to adjust into a stable state. This is then taken as the basis of the employed equilibrium by normalising the flow profile so that:

$$v_z = A\frac{v_z^*}{v_z^*\left(0\right)}, \tag{3.45}$$

where v_z^* is the steady state flow obtained numerically and A is the desired amplitude. This new flow profile is allowed to settle once again and forms the equilibrium used for this study. This may allow the flow to obtain larger speeds than originally obtained for v_z^*, yet, if A is chosen such that $v_z \approx c_s$ then an upward propagating shock ensues.

In addition to this equilibrium, an exponential profile is generated to coincide with the linear model constructed using LCPFCT, where a source term is added to the momentum (3.35) and energy (3.37) equations in order to satisfy both. The equilibrium is defined through:

$$v_z = v_z\left(0\right)\,\exp\left(-\frac{z}{z_0}\right), \tag{3.46}$$

$$\rho = \rho\left(0\right)\,\exp\left(\frac{z}{z_0}\right), \tag{3.47}$$

and

$$p = p\left(0\right)\,\left(\frac{v_z\left(0\right)}{\rho v_z}\right). \tag{3.48}$$

The gravitational source terms are manipulated to incorporate the required source term so that $\rho(F+g)$ and $\rho(F+g)\cdot v$, where F is given by:

$$F+g=\frac{v_z}{z_0}\,c_s(0)\,, \tag{3.49}$$

and $c_s(0)$ is the sound speed at the bottom boundary and $g=1$. The force (3.49) is smoothed to 0 at the top and bottom boundaries using a cubic function, much like equation (3.41). VAC numerically adjusts the profiles (3.46) - (3.48) into a steady-state to offset the reduction of force (3.49) to 0. One particular issue with this equilibrium is that a shallow profile must be employed by taking larger values for z_0 in order to ensure numerical stability.

3.8.3 Alfvén Wave Shoaling

The results from the two equilibria discussed previously do not differ, and as such, we will focus on those obtained for the equilibrium that uses Newton's method of root finding (Figure 3.9). A driver which generates an Alfvén wave is introduced through equation (3.26) where $z_{min}=3$, $z_{max}=3.6$, and $t_{max}-t_{min}=2$. The amplitude, A is adjusted so that the generated wave may be considered linear. The Alfvén wave splits into upward and downward propagating waves. Here, the downward propagating wave propagates out of the modelled flux tube. However, the only similarity the upward propagating wave exhibits with the one in the linear study is that the wave stalls as it approaches the equipartition level (Figure 3.10).

However, in this case, the amplification is not the same as that obtained previously. Instead, the amplification is more similar to the wave shoaling seen in tsunamis. As the leading edge of the Alfvén wave reaches the equipartition level it begins to stall but the tail-end of the wave continues to propagate unhindered until it too approaches the equipartition level. As such, the perceived amplification is merely the Alfvén wave being 'squashed' by the equipartition level (Figure 3.11).

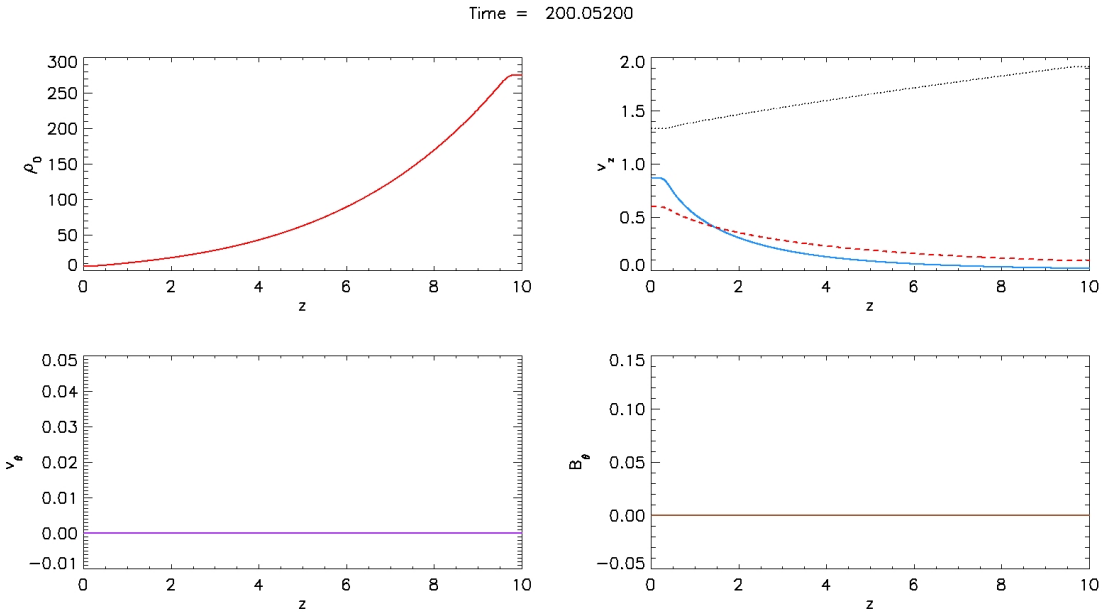

Figure 3.9: Plots showing the equilibrium obtained from Newton's root finding method for (*clockwise*) density, longitudinal velocity, torsional velocity, and torsional magnetic field. In the upper-right panel, the dotted line is sound speed, the solid blue line shows the downflow, and the Alfvén speed is shown with the dashed red line.

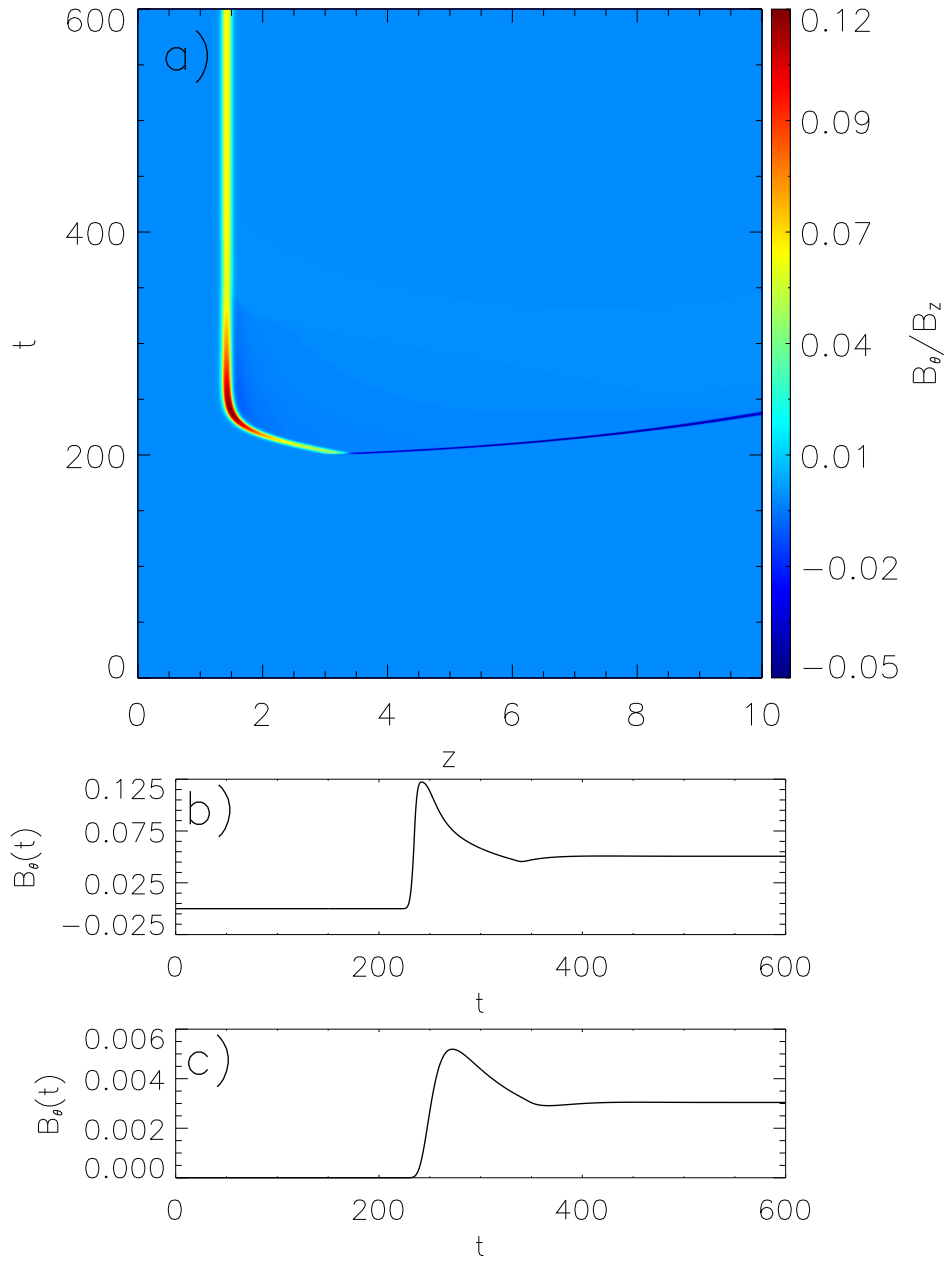

Figure 3.10: **a)** A time-distance plot for the B_θ component of the Alfvén wave. This shows at $t = 200$ that a wave is generated at $z = 3-3.6$, which splits into upward and downward propagating components. The downward propagating wave propagates out of the simulated flux tube at $t = 240$. The upward propagating wave is seen to stall and amplify initially as it reaches the equipartition level before it begins to attenuate. Panels **b)** and **c)** show the temporal evolutions at $z = 1.48$ and $z = 1.3$, respectively.

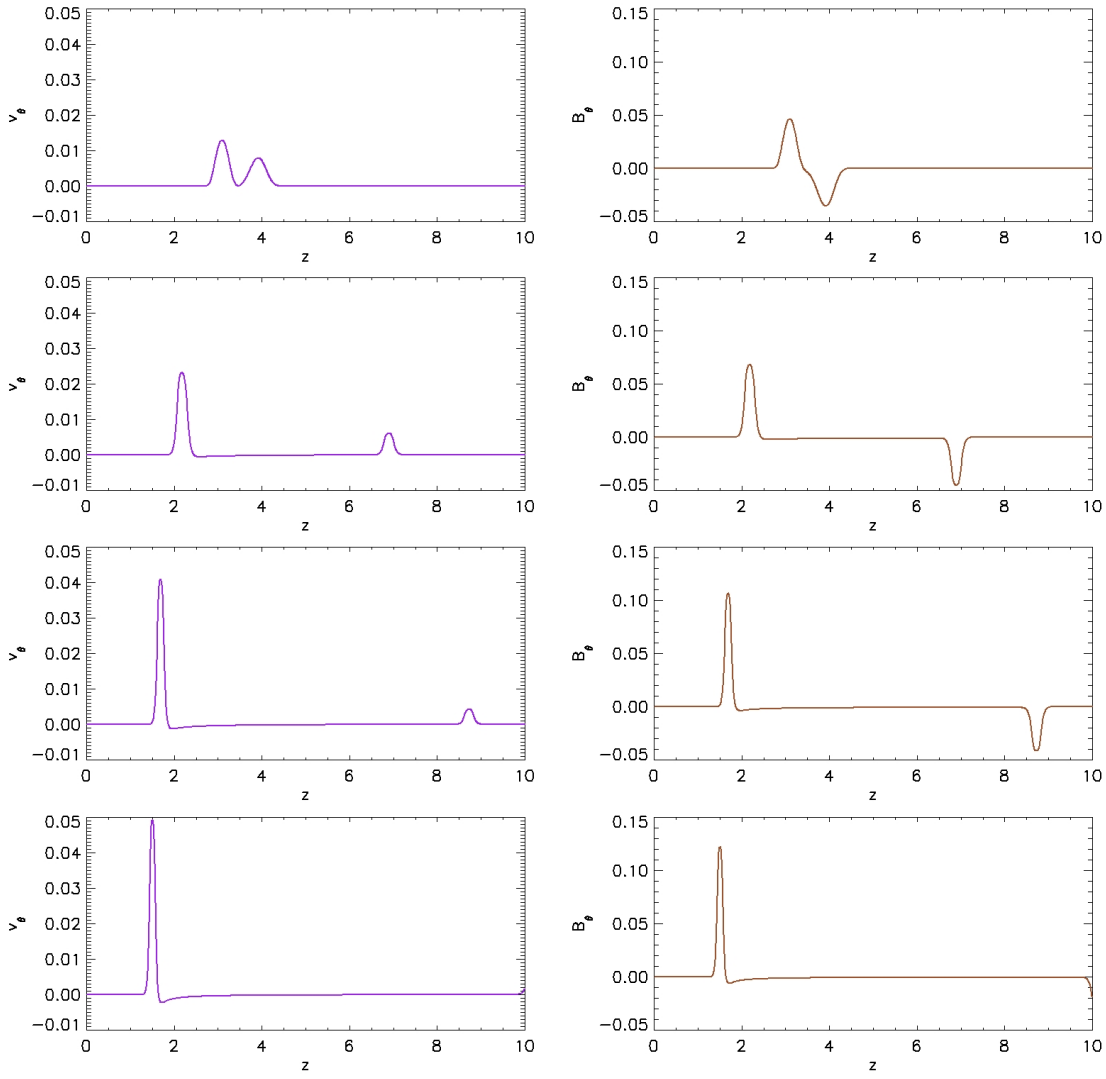

Figure 3.11: Image shows the evolution of B_θ in the first column and v_θ in the second column, where time increases down the rows. The snapshots are from times: $t = 202.65, 214.67, 226.69, 238.71$. This clearly shows that both components of the Alfvén wave exhibit shoaling, *i.e.* as the amplitude increases, the wavelength decreases.

3.8.4 Summary of the Non-Linear Case

The instability witnessed in the linear regime whereby Alfvén waves may become amplified through interaction with a negative flow gradient should exist in the non-linear regime. However, that is not what is seen in this case. This is most likely due to the difficulty of the problem and VAC's inability to accurately resolve it. It seems that solving a system which contains non-constant flow and density profiles in the presence of gravity is too strenuous a task; much like how LCPFCT struggled to resolve the shocktube problem within a sunspot (§2).

The equilibria obtained within VAC could be the reason behind the wave shoaling seen. That is, the gradients could be too small for the wave-flow coupling (3.33) to overcome the numerical diffusion that VAC employs for stability. Another factor which may contribute to this is the close proximity of the critical point to the region where artificial smoothing of the gravity profile begins.

Unfortunately, this study will have to be revisited at a later date using a more robust library that can handle the geometry at hand. It will be interesting to see how the non-linearity of the Alfvén wave amplification effects the downflowing plasma and how it relates to vortex motions such as Bonet et al. [2008, 2010].

Chapter 4

Formation of a Dense Flux Rope by a Siphon Flow

The work presented in this chapter has been submitted to the Astrophysical Journal and has been deemed to merit publication pending amendments.

4.1 Abstract

The interaction of a siphon flow with an initially linear Alfvén wave within an isolated chromospheric loop is investigated. The loop is modelled using 1.5-D magnetohydrodynamics (MHD). The siphon flow undergoes a hydrodynamic (HD) shock, which allows the Alfvén instability to amplify the propagating waves as they interact with the shock and loop footpoints. The amplification leads to non-linear processes strongly altering the loop equilibrium. Azimuthal twists of 50 $\mathrm{km\,s^{-1}}$ are generated and the loop becomes globally twisted with an azimuthal magnetic field of $B_\theta \approx 5 \times B_z$. The siphon flow is accelerated to ≈ 70 $\mathrm{km\,s^{-1}}$ in the $+z$ direction due to the propagating shock waves that form. Near the end of the simulation, where the non-linear processes are strongest, flow reversal is seen within the descending leg of the loop, generating upflows up to 28 $\mathrm{km\,s^{-1}}$. This flow reversal leads to photospheric material being 'pulled' into the loop and spreading along its entirety. Within about 2.5 h the density increases by a factor of about 30 its original value.

4.2 Introduction

Prominences are common magnetic structures within the solar atmosphere observed on the limb. On the disk they appear as dark structures called filaments. These structures are classified based on the region they form. If they form above the polarity inversion line or PIL, they are quiescent prominences and if they form above sunspot regions they are active region prominences. Prominences/filaments are thought to be suspended against gravity by magnetic forces and the fine threads that form them have been shown to be filled with cool plasma that is $\approx 100\times$ denser and cooler than the surrounding corona [Tandberg-Hanssen, 1995; Vršnak et al., 1988].

Prominences are magnetic structures that display flows, and as such are highly dynamical. Berger et al. [2008] show that quiescent prominences exhibit upward propagating waves comparable to the sound speed of a $10^4\ K$ plasma as well as turbulent upflows. The upflows rise with speeds $\approx 20 km s^{-1}$, reaching a maximum of $\approx 50\, km\, s^{-1}$, and emanate from the base to heights of $\approx 10-20\, Mm$, spanning widths of $170-700\ km$. Some of the vertical filament prominences experience downflows, turbulence, oscillatory motions, and vortices of speeds $\approx 10\ km\ s^{-1}$, which is slower than gravitational free-fall. These downflows were previously detected in lower resolution, and subsequently less detail [Schmieder and Mein, 1989; Schmieder et al., 1991]. Other studies show the high variability of the flows within prominences, with both the horizontal and vertical motions falling within $10-70\ km\ s^{-1}$ [Chae et al., 2008; Engvold, 1976; Okamoto et al., 2007; Zirker et al., 1998].

Chae [2010] show that hedgerow prominences are magnetically supported against gravity, and most prominently by the magnetic dips. The results agree with previous work [Berger et al., 2008; van Ballegooijen and Cranmer, 2010]. They find vertical fields dominate the horizontal fields outside the current sheet whilst van Ballegooijen and Cranmer [2010] found tangled fields in a vertical current sheet on either side of the sheet.

Prominences have been modelled/interpreted as structures embedded within twisted flux tubes (or flux ropes) in numerous studies, *e.g.* Filippov et al. [2015]; Keppens and Xia [2014]; Okamoto et al. [2009]; Priest et al. [1989]; van Ballegooijen and Martens [1989]; Wang and Stenborg [2010]; Yang et al. [2016]. Wang and Stenborg [2010] observe transverse motions of $5-10\,km\,s^{-1}$ within cavities where the spin direction aligns with the strongest to weakest magnetic field of the footpoints across the polarity inversion line (PIL). They interpret this asymmetry as a siphon flow before the cavity and adjacent streamer loops become 'pinched' to form a flux rope.

Work by van Ballegooijen and Martens [1989] demonstrates that helical field lines, which arise due to flux cancellation in a sheared magnetic field, are capable of supporting prominence plasma. They find that the resulting field is stable against perturbations. Priest et al. [1989] show that twisting by Coriolis forces can create a 'dip' when B_θ exceeds a certain condition. In turn, these dips in the twisted field lines allow thermal condensation to occur and thus the plasma to accumulate at the dips, forming the prominence. They also show that as a prominence migrates polewards it becomes twisted further, where it undergoes reconnection and changes from normal polarity to inverse polarity.

SOHO observations have been used to study the photospheric magnetic field of active region *NOAA* 8668 during the formation of a reverse S-shaped active filament [Chae et al., 2001]. The authors postulate that the filament formation may be part of a bigger magnetic structure that may consist of a flux rope and overlaying sheared arcade. More recently, *SDO* observations of active region *NOAA* 11884 have detailed the formation of an inverse-S shaped filament. The filament erupted, with Yan et al. [2016] suggesting it may have been a twisted structure. Török and Kliem [2005] investigate the helical kink instability for a MHD flux rope model. The model replicates the behaviour of a confined filament eruption (2002-05-27) and by modifying the magnetic field to decrease more rapidly, an ejective eruption which agrees with a CME observation (2001-05-15). They state that the helical kink instability for a twisted flux rope is a mechanism capable of driving solar eruptions. For detailed reviews on prominences, see Arregui et al.

[2012]; Parenti [2014].

Prominences are often thought of as twisted, loop-like structures. A property of a loop structure is that it may exhibit a siphon flow. These siphon flows have long been studied in context of the solar environment and were first studied in magnetic flux tubes in relation to the Evershed effect in sunspots [Meyer and Schmidt, 1968]. Subsequently, numerous studies have since investigated these siphon flows within magnetic flux tubes *e.g.* Bethge et al. [2012]; Cargill and Priest [1980]; Grappin et al. [2005]; Montesinos and Thomas [1997]; Orlando et al. [1995a,b]; Taroyan [2009]; Thomas [1988].

In loops, a siphon flow may occur when there is a pressure gradient between the footpoints. This pressure gradient allows photospheric material to rise along the ascending leg of the loop until it reaches the loop apex. At this point, gravity aids the acceleration of the mass movement, which often leads to supersonic flow and the possibility of shocks arising in the descending leg. Orlando et al. [1995a] developed a model of equilibrium conditions for siphon flows within coronal loops using and comparing two independent numerical codes. This, combined with analytical derivations allow them to accurately explore the solution space in proximity of critical points. They determined there are four solutions: subsonic, supersonic, critical, and unphysical. For the first two of these solutions, they derived scaling laws, whilst supersonic solutions may only exist for negative heat flux at the base of the loop (positive direction of coordinate, S). Orlando et al. [1995b] build upon this by introducing a parametrised heating term. This allows them to study stationary (adiabatic and isothermal) shocks within coronal loops for supersonic and critical siphon flows. The authors show that the volumetric heating rate of the loop determines the location of the stationary shock. It is also demonstrated that there exists a range of volumetric heating rates for which a shock can form in two alternative locations, with isothermal shocks for critical flows being the exception.

In this chapter we present a mechanism associated with siphon flows which could play an important role in prominence formation. An initial loop of high inclina-

tion is assumed. The footpoints of the loop reside in/near the photosphere and a siphon flow is employed between them. Following from previous studies [Orlando et al., 1995b; Williams et al., 2016], the supersonic flow becomes subsonic as it passes through a hydrodynamic (HD) shock. A small amplitude magnetic twist is introduced to the system and it becomes amplified through the Alfvén instability discussed in previous work [Taroyan, 2008, 2009, 2011, 2015; Taroyan and Williams, 2016; Williams et al., 2016]. We trace the evolution and the nonlinear consequences of the amplifying twists. The main result is the formation of a flux rope with enhanced density as a result of the amplification process. The final configuration is reminiscent to the initial flux rope seen in Török and Kliem [2005] and Titov and Démoulin [1999]. In work by Török and Kliem [2005] the flux rope becomes subject to the kink instability. Our model describes a process that may allow untwisted loops to form structures that lead to the twisted flux ropes that are prone to kink instability and prominence eruptions.

In §4.3 we discuss the model used for the study and the results of which are presented in §4.4 and discussed in §4.5 with reference to current literature. Concluding remarks are made in Section §4.6.

4.3 Numerical Method

In previous work [Williams et al., 2016], one end of the flux tube was rooted in the photosphere and the other was open ended. This allowed us to model the Evershed effect in sunspots. However, in this study we wish to study the Alfvén instability in a highly inclined loop. The high inclination means that gravity may be neglected. Another implication is that both ends of the flux tube are now rooted in the photosphere. The footpoints are treated in such a way that they are allowed to bend in response to plasma and wave motion within the flux tube.

We impose a Dirichlet-like boundary condition for the azimuthal momentum ($\rho v_\theta|_{z=0,L} = 0$) at each end of the flux tube. All other boundary types (ρ, ρv_z, e, B_θ, and B_z) are Neumann boundary conditions where $\frac{\partial}{\partial z}|_{z=0,L} = 0$. The Dirichlet boundary conditions represent magnetic field lines anchored in a dense

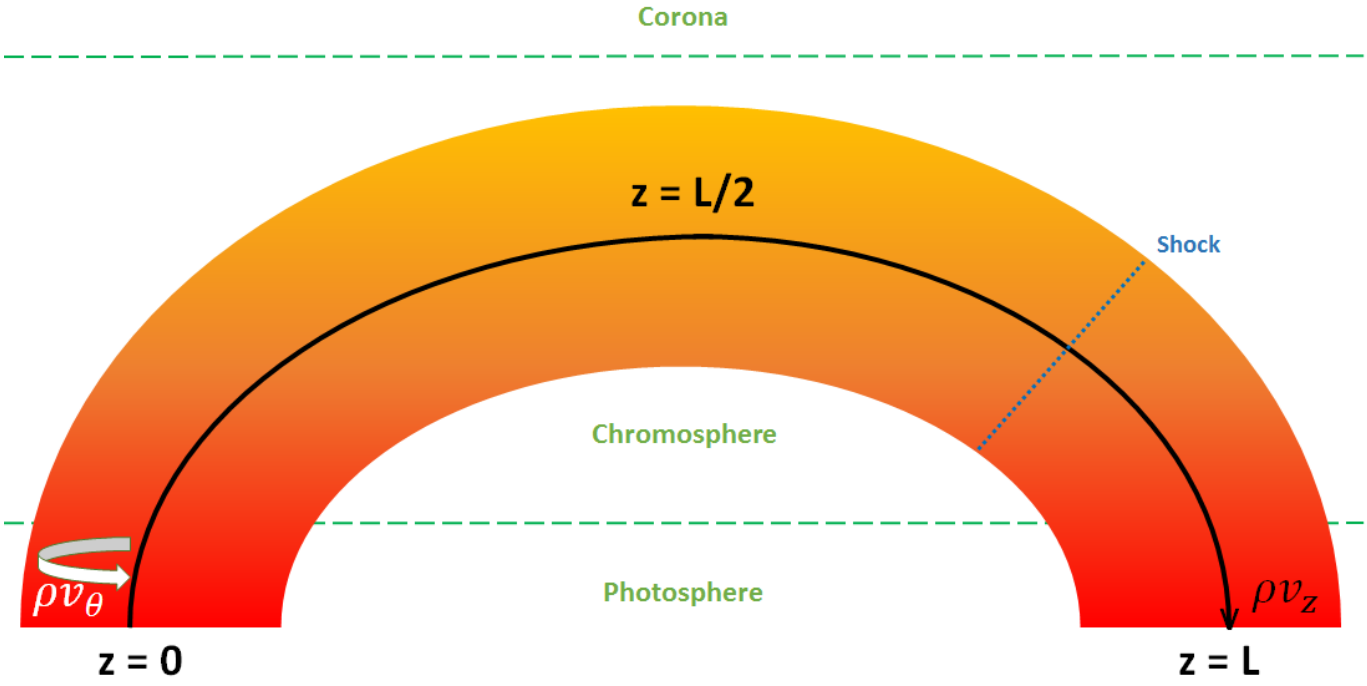

Figure 4.1: A schematic showing the geometry of the model employed during the study. The flow propagates from $z = 0$ to $z = L$ and undergoes a HD shock in the descending leg of the loop. Both footpoints are situated in the dense photosphere. Subsequently, any azimuthal perturbations are reflected back into the chromospheric loop upon interaction with the loop footpoints.

photosphere, and allow magnetic cavities to form and trap the propagating waves within the loop structure. In our model this boundary condition is imposed by setting the ghost cells boundary type to asymmetric. This copies and multiplies the nearest two-mesh cells by -1. This ensures any perturbation interacting with the boundary changes sign upon reflection as opposed to being 'squashed' and 'skipping' off the photosphere. This prevents a non-physical, continual twist in one direction or the other. These boundary conditions are discussed in more detail in Williams et al. [2016, §2.4].

Taroyan and Williams [2016] have recently demonstrated that the total magnetic energy along an infinite tube increases when there is no azimuthal energy flux through the boundaries and when the azimuthal magnetic flux along the tube remains constant. The amplification is due to the wave-flow coupling everywhere along the infinite tube which is expressed through the source term s_θ. In the present context, we have selected photospheric line-tying as boundary conditions.

A supersonic flow that is sub-Alfvénic is introduced and undergoes a shock that is located in the descending leg of the loop so as to be consistent with Orlando et al. [1995b] and to replicate what would likely occur to the flow within the loop if gravity were included in the simulations. This is because gravity would aid the acceleration of the flow in the descending leg of the loop, which may lead to supersonic flows steepening into a HD shock.

The numerical code used to model our loop is VAC (*Versatile Advection Code*; Tóth, 1997). Fourth order central differencing method (CD4) is used in combination with the minmod limiter and TVDLF (*Total Variance Diminishing Lax-Friedrich*) predictor step.

The model presented in this paper is a 1.5-D axisymmetric magnetic shocktube, which was introduced by Hollweg et al. [1982] and subsequently employed by Kudoh and Shibata [1999]; Matsumoto and Shibata [2010]; Sterling and Hollweg [1988]; and others. It is discussed by Hollweg [1981] that a single field-line is modelled which resides close to but not on the axis of symmetry, such that for

typical cylindrical coordinates, $r \neq 0$ at any point. The equations used in these models may describe torsional and shear Alfvén waves in the non-linear regime depending on whether the chosen geometry is cylindrical or Cartesian (Priest, 2014, §4.3). A consequence of the geometry employed is that θ denotes the azimuthal direction, where it is assumed that $\frac{\partial}{\partial \theta} = 0$.

The 1.5-D model consists of 3000 gridpoints of uniform spacing, and the ideal-MHD equations solved are given by Hollweg [1992]:

$$\frac{\partial \rho}{\partial t} + \frac{\partial}{\partial z}\left(v_z \rho\right) = 0, \tag{4.1}$$

$$\frac{\partial}{\partial t}\left(\rho v_z\right) + \frac{\partial}{\partial z}\left(v_z \rho v_z\right) = -\frac{\partial}{\partial z}\left(p_{tot}\right), \tag{4.2}$$

$$\frac{\partial}{\partial t}\left(\rho v_\theta\right) + \frac{\partial}{\partial z}\left(v_z \rho v_\theta\right) = \frac{B_z}{\mu_0}\frac{\partial}{\partial z}\left(B_\theta\right), \tag{4.3}$$

$$\frac{\partial e}{\partial t} + \frac{\partial}{\partial z}\left(v_z e\right) = \frac{B_z}{\mu_0}\frac{\partial}{\partial z}\left(v_z B_z + B_\theta v_\theta\right) - \frac{\partial}{\partial z}\left(v_z p_{tot}\right), \tag{4.4}$$

$$\frac{\partial B_\theta}{\partial t} + \frac{\partial}{\partial z}\left(v_z B_\theta\right) = \frac{B_z}{\mu_0}\frac{\partial}{\partial z}\left(v_\theta\right), \tag{4.5}$$

where

$$p_{tot} = \frac{1}{2}\mathbf{B}^2 + p, \tag{4.6}$$

and

$$p = (\gamma - 1)\left(e - \frac{1}{2}\rho \mathbf{v}^2 - \frac{1}{2}\mathbf{B}^2\right). \tag{4.7}$$

For brevity, $\mathbf{B} = B_z \mathbf{e_z} + B_\theta \mathbf{e}_\theta$, and $\mathbf{v} = v_z \mathbf{e_z} + v_\theta \mathbf{e}_\theta$. The plasma density, longitudinal and azimuthal velocities, internal energy, as well as the longitudinal and azimuthal magnetic field components are given by: ρ, v_z, v_θ, e, b_z, and b_θ, respectively.

The non-linear coupling between the azimuthal and longitudinal variables is given by p_{tot} in equations (4.2) and (4.4). As is the case with Williams et al. [2016],

the conservation of energy can be expressed through combining equations (4.4), (4.6), and (4.7), which yields:

$$\frac{\partial}{\partial t}\left[\frac{p}{\gamma-1}+\frac{1}{2}\rho\mathbf{v}^2+\frac{1}{2}B_\theta^2\right] + \frac{\partial}{\partial z}\left(v_z\left[\frac{\gamma p}{\gamma-1}+\frac{1}{2}\rho\mathbf{v}^2\right]\right) + \frac{\partial}{\partial z}\left(v_z B_\theta^2 - v_\theta B_\theta B_z\right)=0. \quad (4.8)$$

The thermal, kinetic, and magnetic energy densities are given in the temporal derivative of equation (4.8).

Equation (4.8) describes the evolution of the total energy. In Appendix C we derive the following equation for the azimuthal (twist) component of energy:

$$\frac{\partial W_\theta}{\partial t}+\frac{\partial F_\theta}{\partial z}=-\frac{\partial v_z}{\partial z}\frac{b_\theta^2}{2\mu_0}. \quad (4.9)$$

The left hand side of equation (4.9) contains the time derivative of the azimuthal energy density and the spatial derivative of the azimuthal energy flux. The right hand side (RHS) of equation (4.9) contains a source term. It shows that an accelerating (decelerating) flow corresponding to $dv_z/dz > 0$ ($dv_z/dz < 0$) leads to the possibility of energy transfer between the longitudinal and transverse motions even in the linear regime. This wave-flow coupling plays a key role in the amplification of small amplitude twists, the consequences of which we study here.

We use the energy equations (4.8) and (4.9) to define the following terms:

$$W_\theta = W_{\theta k} + W_{\theta m}, \quad (4.10)$$

$$W_z = W_{zk} + W_{th}, \quad (4.11)$$

and

$$s_\theta = -\frac{\partial v_z}{\partial z} W_{\theta m}. \tag{4.12}$$

Here, W_θ, $W_{\theta k}$, and $W_{\theta m}$ are the azimuthal components of total energy, kinetic energy, and magnetic energy. W_z is the total longitudinal energy, where W_{zk}, and W_{th} represent the z-component of the kinetic energy, and the thermal energy of the plasma. The source term that describes how kinetic energy of the flow is converted into magnetic twist is denoted as s_θ, and is derived in Taroyan and Williams [2016] for a linear system. In Appendix C, we have shown that the terms remain valid for this non-linear study.

Integrating equation (4.9) between 0 and L and rearranging yields:

$$\frac{\partial W_{\theta T}}{\partial t} = F_\theta(0) - F_\theta(L) - \int_0^L \frac{\partial v_z}{\partial z} \frac{b_\theta^2}{2\mu_0}, \tag{4.13}$$

where $W_{\theta T}$ is the total azimuthal energy along the loop. $F_\theta(0)$ and $F_\theta(L)$ are the azimuthal energy fluxes at the footpoints, $z = 0$ and $z = L$, respectively. The last term on the RHS of (4.13) describes the total contribution of wave-flow coupling, s_θ along the entirety of the loop. The azimuthal component of the energy flux, F_θ in equation (4.9) is defined as:

$$F_\theta = v_z W_\theta - \frac{B_z^2}{\mu_0} v_\theta B_\theta. \tag{4.14}$$

4.3.1 The Loop Model

The loop is situated between the two footpoints at $z = 0$ and $z = L$, with the loop apex situated at $z = L/2$ (Figure 4.1). A supersonic flow emanates from within the photosphere and propagates along the loop until it undergoes a HD shock at $z = 0.8\,L$. The shock is described in terms of the Rankine-Hugoniot jump conditions:

$$v_{z2} = v_{z1} \frac{\rho_1}{\rho_2}, \tag{4.15}$$

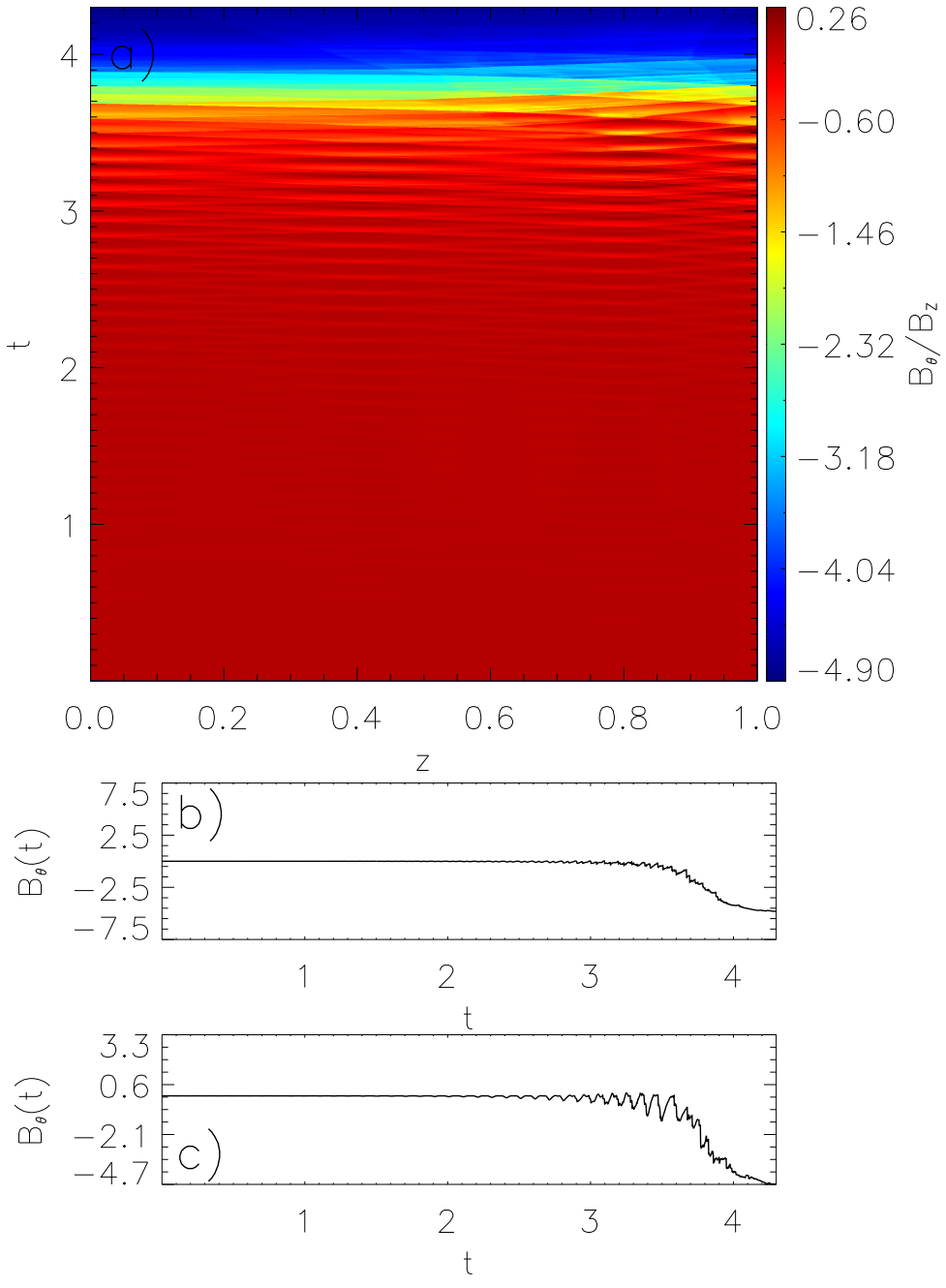

Figure 4.2: Time-distance plot for B_θ is shown in **a)** with the associated colour bar. Panels **b)** and **c)** show the magnetic twist for the entire simulation at positions $z = 0.167\,L$, and $z = 0.834\,L$, respectively.

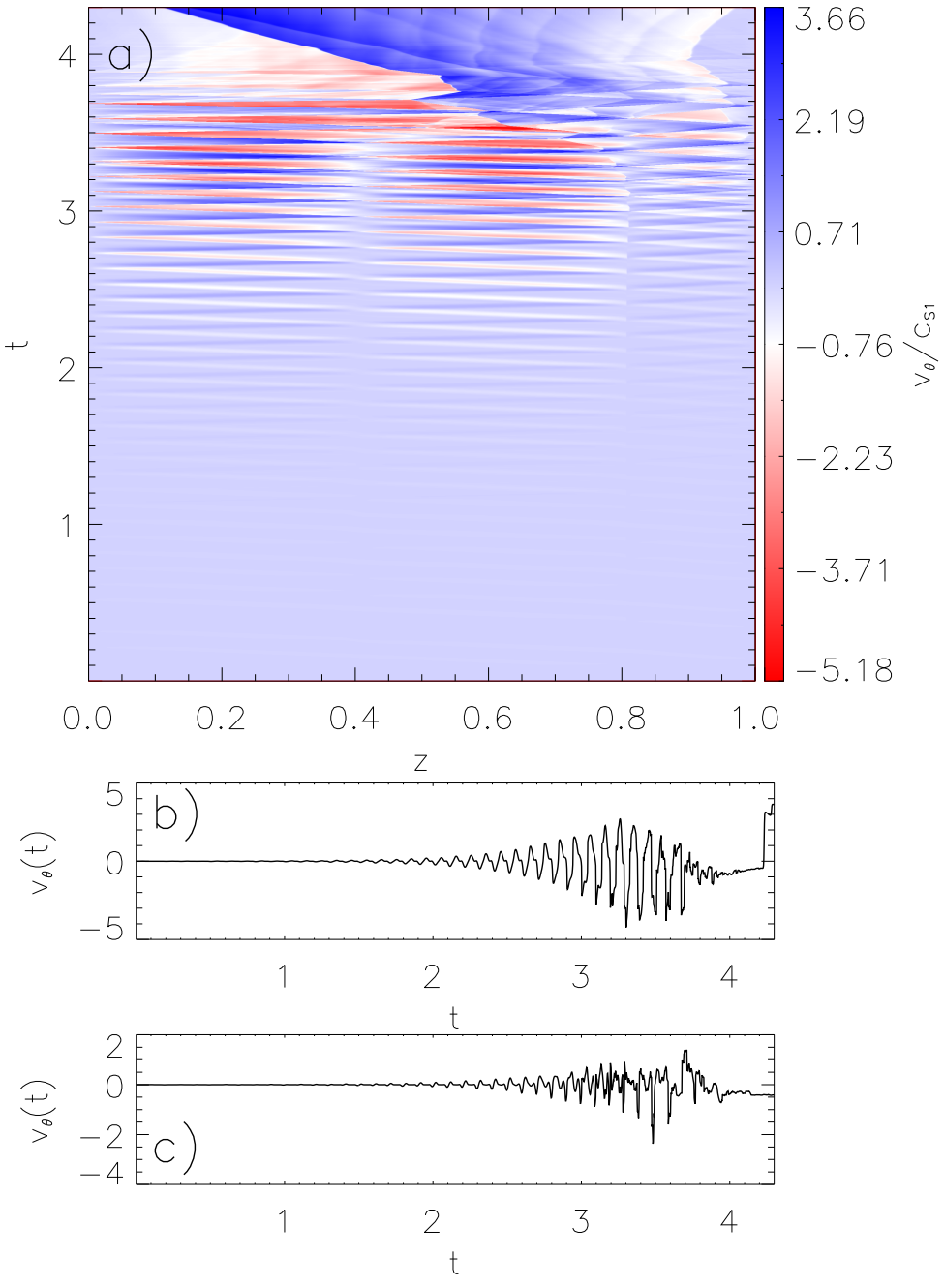

Figure 4.3: Time-distance plot for v_θ is shown in **a)** with the associated colour bar. Panels **b)** and **c)** show the azimuthal twist velocity for the entire simulation at positions $z = 0.167\,L$, and $z = 0.834\,L$, respectively.

$$\rho_2 = \rho_1 \frac{v_{z1}}{v_{z2}}, \tag{4.16}$$

$$p_2 = p_1 - \rho_2 v_{z2}^2 + \rho_1 v_{z1}^2, \tag{4.17}$$

$$e_2 - e_1 = \frac{1}{2}\left(v_{z1}^2 - v_{z2}^2\right) + \frac{p_1\rho_2 - p_2\rho_1}{\rho_1\rho_2}, \tag{4.18}$$

where

$$v_{z1} = M_{c1} c_{S1}, \tag{4.19}$$

and

$$c_{S1} = \sqrt{\frac{\gamma P_1}{\rho_1}} = \sqrt{\frac{\gamma R T_1}{\xi}}. \tag{4.20}$$

Here, the sound speed is given by c_S, whilst subscripts 1 and 2 denote the plasma upstream and downstream of the shock. $M_{c1} = 3$ is the sonic Mach number of the upstream plasma. $\gamma = 1.2$ is the adiabatic index, and is chosen to represent a partially ionised chromosphere, such as is discussed in **?**, p.118-119. R is the molar gas constant, ξ is the molar mass, and T is the plasma temperature. The Alfvén speed within the loop is, $c_A = 9\, c_S$. Using the definition of Alfvén speed, $c_A = \frac{B}{\sqrt{\mu_0 \rho}}$, and given that $\rho_1 = 1$, and the normalisation of B and μ_0 is done so that $\mu_0 = 1$ within VAC, c_A can be used to infer the magnetic field strength, $B = 9$. Pressure, $p_1 = 0.833$ at the $z = 0$ boundary is calculated from equation (4.20).

We provide some example values that can be obtained through parametrisation of these variables to make the model consistent with the solar atmosphere, however, all results shown are normalised quantities. Assuming a sound speed of $c_{S1} = 10$ km s^{-1} within the loop yields flow, and Alfvén speeds of $v_{z1} = 30$ km s^{-1} and $c_{A1} = 90$ km s^{-1}, respectively. Similarly, given the Alfvén speed and taking $\rho_1 = 1.5 \times 10^{-12}$ g cm^{-3}, the magnetic field strength can be deduced to be, $B_{z(1,2)} = 39.1$ G. Using equation (4.20) and the values obtained for c_{S1}, and ρ_1, pressure within the loop is, $p_1 \approx 1.25$ dyn cm^{-3}. The length of the loop is 20 Mm with a resolution of ≈ 6.67 km. As the loop is highly inclined, the eleva-

tion remains below 2 Mm, i.e., within the chromosphere of a conventional model atmosphere. The total simulation time equates to: 2 h 23 m 24 s with one unit time, $L/c_{S1} = 33$ m 20 s.

4.3.2 Alfvén Wave Driver

A single Alfvénic pulse is launched near the $z = 0$ boundary by adding a source term (4.21) as ρF in the momentum equation (4.3) and as $\rho F \cdot v$ in the energy equation (4.4):

$$\rho F = A \sin^2\left(\pi \frac{t - t_{min}}{t_{max} - t_{min}}\right) \sin^2\left(\pi \frac{z - z_{min}}{z_{max} - z_{min}}\right). \tag{4.21}$$

$A = 10$, is the amplitude, $t_{min} = 0$, and $t_{max} = t_{min} + 0.05\ L/c_{S1}$. The driver is active between $z_{min} = 0$, and $z_{max} = 0.025\ L$ and between t_{min} and t_{max}. A simplistic schematic is shown in Figure 4.1.

4.4 Results and Analysis

A highly-inclined loop is modelled, as is shown in Figure 4.1. A supersonic flow emanates from the $z = 0$ footpoint, which propagates in the $+z$ direction and undergoes a HD shock at $z = 0.8\ L$. This follows the coronal loop set-up in the work by Orlando et al. [1995b], where a shock forms due to gravity accelerating the siphon flow in the descending leg. It will become evident throughout this section that this shock is of great importance during the amplification process of the Alfvén waves.

The simulation begins when a single azimuthal pulse that is determined by expression (4.21) is launched from the footpoint at $z = 0$, $t = 0$. The pulse propagates along the loop until it interacts with the stationary shock. The Alfvén wave is partially transmitted through the shock from the upstream plasma into the downstream plasma, with the rest of the wave being over-reflected by the shock

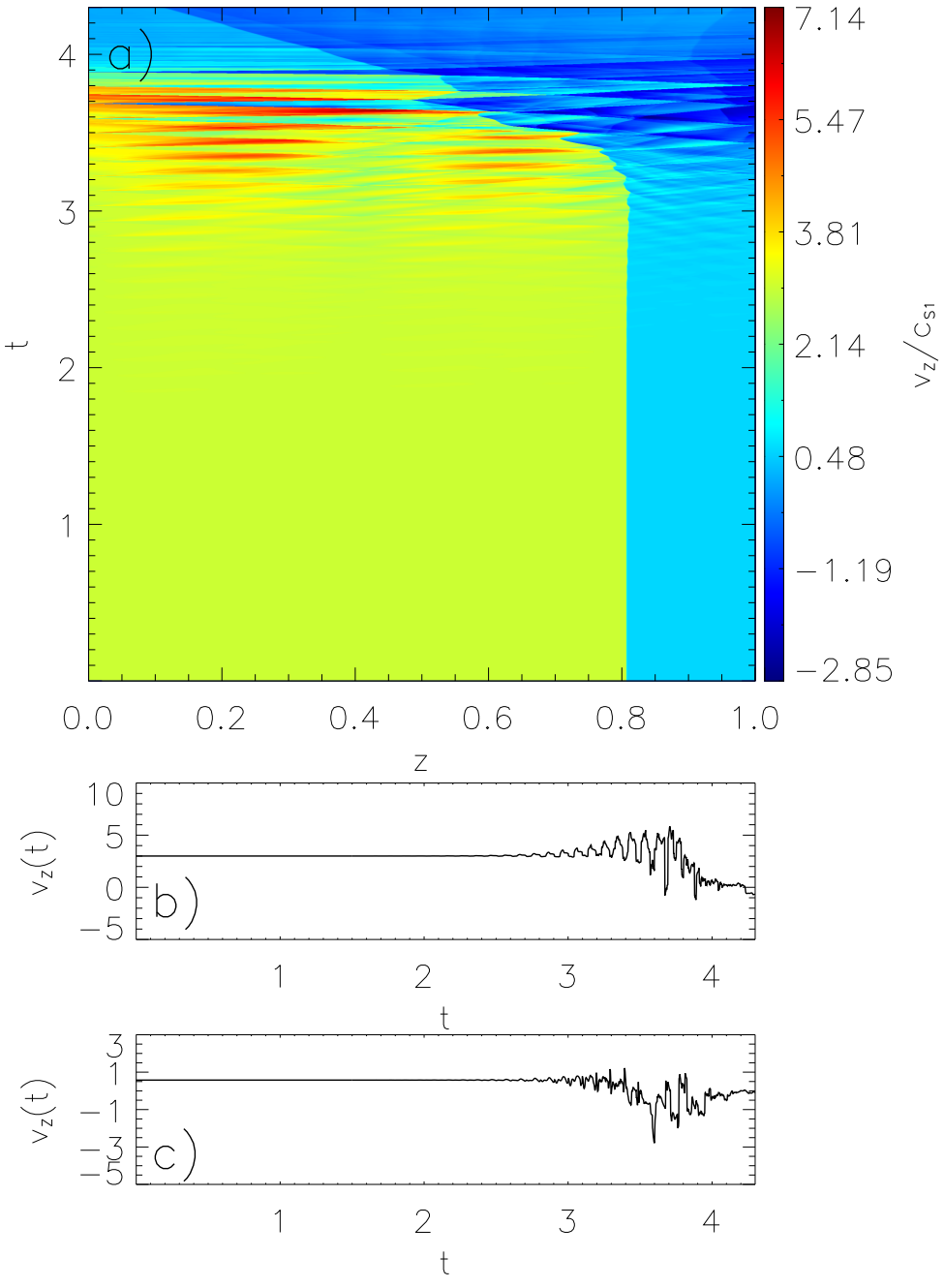

Figure 4.4: Time-distance plot for v_z is shown in **a)** with the associated colour bar. Panels **b)** and **c)** show the flow velocity for the entire simulation at positions $z = 0.167\,L$, and $z = 0.834\,L$, respectively.

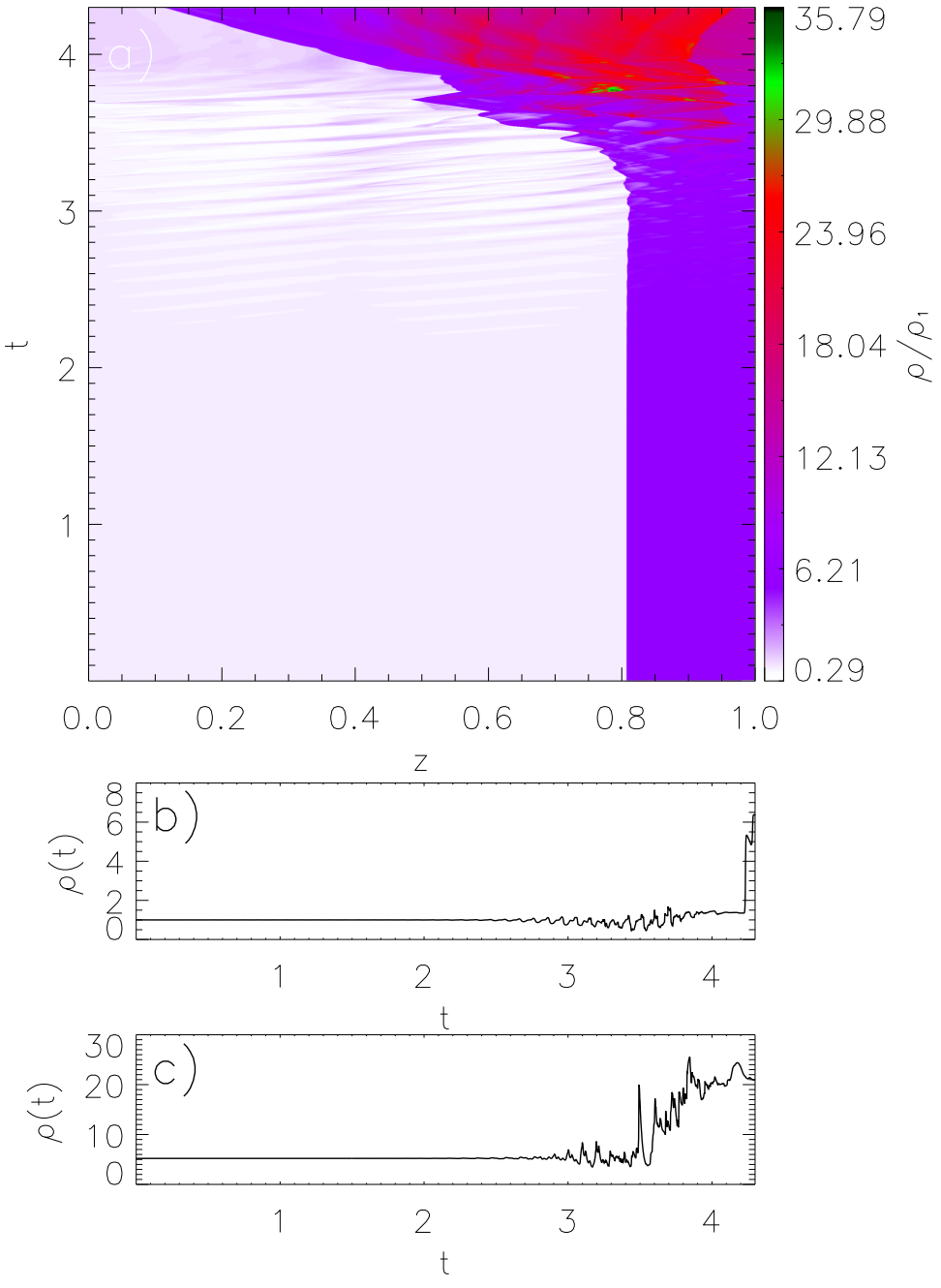

Figure 4.5: Time-distance plot for ρ is shown in **a)** with the associated colour bar. Panels **b)** and **c)** show the density for the entire simulation at positions $z = 0.167\,L$, and $z = 0.834\,L$, respectively.

[Acheson, 1976; Williams et al., 2016] and propagating back towards the $z = 0$ boundary. Once the reflected pulse reaches and interacts with the $z = 0$ footpoint, it is reflected back up and along the flux tube for the process to repeat until the wave becomes non-linear.

The portion of the Alfvén wave that is partially transmitted through the stationary shock propagates out of the simulated flux tube in our previous study [Williams et al., 2016]. However, as we are now simulating a loop, whose footpoints are embedded within the photosphere, the wave is now reflected and partially transmitted at $z = L$.

When the wave propagates in the $-z$ direction after reflection from the photosphere ($z = L$), it again interacts with the shock where it is both partially transmitted into the upstream plasma and reflected back towards $z = L$. The portion of the Alfvén wave that passes through the shock into the upstream plasma is free to merge with the Alfvén wave trapped between the shock and $z = 0$, and potentially accelerate the amplification process further (Supplementary Movie 3).

Similarly, each time the Alfvén wave in region 1 is partially transmitted through the shock into region 2, it also aides the amplification of the Alfvén wave trapped between the HD shock and $z = L$. This continual feedback between the two regions either side of the shock is not possible in Williams et al. [2016] due to one end of the flux tube being open. The magnetic energy of the Alfvén wave is free to escape through the boundary in that study, but this is no longer the case with both ends now being firmly rooted into the photosphere.

The azimuthal time-distance plots (Figures 4.2 and 4.3) show that the amplification process takes until $t \approx 2.3\, L/c_{S1}$ for the Alfvénic perturbations to begin forming strong gradients. Around this time, the non-linear coupling becomes apparent, and secondary, fast and slow-mode waves can be seen in v_z (Figure 4.4) and ρ (Figure 4.5). The fast- and slow-magnetoacoustic waves propagate with phase speeds of c_A, and c_S in a static medium [Priest, 2014]. In our case we have a flowing plasma, thus the phase speeds are $c_A \pm v_z$ and $c_S \pm v_z$, where the $+$ $(-)$

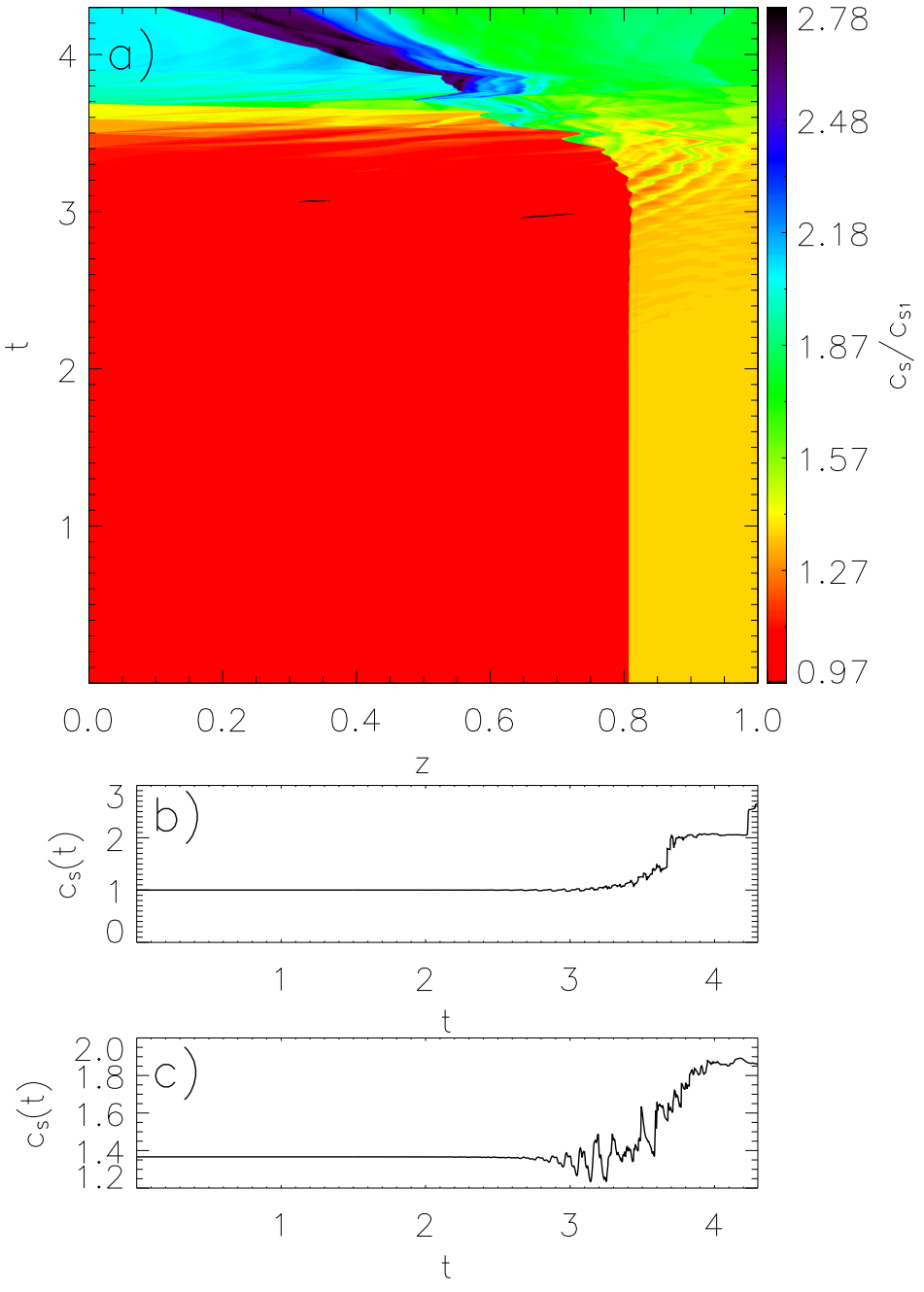

Figure 4.6: Time-distance plot for c_S is shown in **a)** with the associated colour bar. Panels **b)** and **c)** show the sound speed for the entire simulation at positions $z = 0.167\,L$, and $z = 0.834\,L$, respectively.

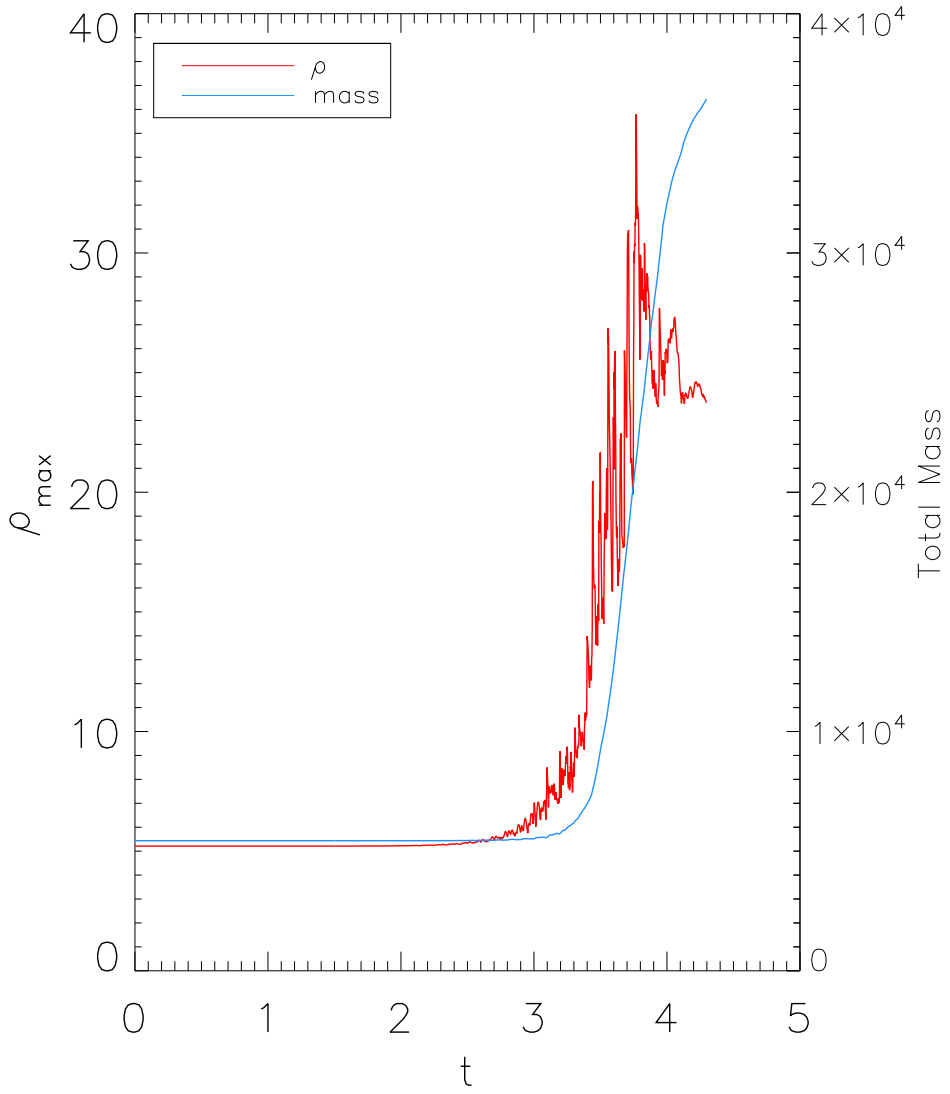

Figure 4.7: Maximum density (*red*) within the loop as a function of time is shown. The maximum can be seen to increase by a factor of 6.87. The total mass within the loop is also plotted (*blue*).

sign denotes wave propagation with (against) the flow.

The amplification of the twist velocity continues until it reaches a maximum of $v_{\theta\,max} \approx 5\,c_{S1}$. This maximum corresponds to the Alfvén wave trapped between the $z = 0$ footpoint and the HD shock. The associated magnetic twist, B_θ begins to form a global twist between $t = 3 - 3.6\,L/c_{S1}$, which can be seen in panel a) of Figure 4.2. The magnetic field twisting appears strongest during the period where the Alfvén waves disturb the HD shock the greatest.

Around this time, it can be seen that there is localised acceleration in the upstream plasma (Figure 4.4), which also leads to regions of decreased density (Figure 4.5). Between $t = 3.5 - 3.8\,L/c_{S1}$, there is also localised deceleration present, which subsequently leads to localised density increases in region 1. These localised variations are the result of fast-mode waves that are coupled to the Alfvén waves, which steepen into propagating shocks as the Alfvén waves continue to amplify.

The Alfvén waves behave somewhat differently in the upstream plasma when compared with the downstream counterparts. Figure 4.5 shows that there is an accumulation of mass in the downstream plasma. This coincides with the Alfvén waves extracting kinetic energy sufficiently enough that the downstream plasma becomes quasi-static. Eventually, due to the non-linear coupling in the momentum (4.2) and energy (4.4) equations, the Alfvén waves incite an inflow from the $z = L$ boundary, which can be seen clearly in Figure 4.4. The decrease in the mass outflux and the subsequent influx through the $z = L$ footpoint are responsible for the mass accumulation.

The time-distance plot for c_S (Figure 4.6) shows us that, prior to the HD shock being disturbed and propagating to the $z = 0$ footpoint, there is a decrease in the sound speed of the downstream plasma before it increases rapidly. This rapid increase suggests that there is a strong increase in pressure, leading to shock heating, and an imbalance of the initial conditions (4.15) - (4.20). This increase in sound speed coincides with the flow reversal at the $z = L$ footpoint.

As is discussed by Williams et al. [2016], this pressure imbalance leads to the HD shock propagating. Between $t = 3.4 - 3.8\, L/c_{S1}$ there is a sudden increase in the sound speed in region 1. This halts the propagation of the shock in the negative z direction, and 'pushes' it back along the loop in the positive z direction. However, this sudden change in upstream plasma pressure appears to invoke a region of larger pressure immediately downstream. This could be a consequence of the flow reversal as there are now two, oppositely propagating flows colliding into one another. This pressure increase leads to a localised region of sound speed that is comparable with the initial supersonic flow along the loop. Once again, this imbalance forces the HD shock to propagate in the negative z direction towards the $z = 0$ footpoint.

In addition to these variations in the thermal pressure either side of the HD shock, there is also a discontinuity that forms in the magnetic pressure. This is caused by the presence of a slow shock forming at the stationary shock location (Supplementary Movie 4; Figure 4.3 at $t \approx 3$, $z \approx 0.8\, L$). This means there is an imbalance in magnetic pressure either side of the HD shock, which aids the aforementioned process by which the stationary shock is disturbed into propagating. In other words, the right hand side of equation (4.2) becomes negative at the shock leading to plasma acceleration in the negative z direction.

Figure 4.7 shows the maximum density within the loop as a function of time with the total mass overplotted. It reveals that the Alfvén waves generate localised accumulation of mass, which precede the increase in total mass of the loop. As these localised events die down ($t \approx 4\, L/c_{S1}$), the mass continues to increase. This may be explained by the $z = L$ footpoint becoming a region of inflow. Thus, the accumulation of mass is a result of a mass flux decrease and subsequent reversal at the $z = L$ footpoint.

4.4.1 The Critical Evolution Period

In this subsection we focus on the period deemed to be pivotal in the system evolution. This period is between $t = 3\, L/c_{S1}$ and $t = 3.6\, L/c_{S1}$. This is where

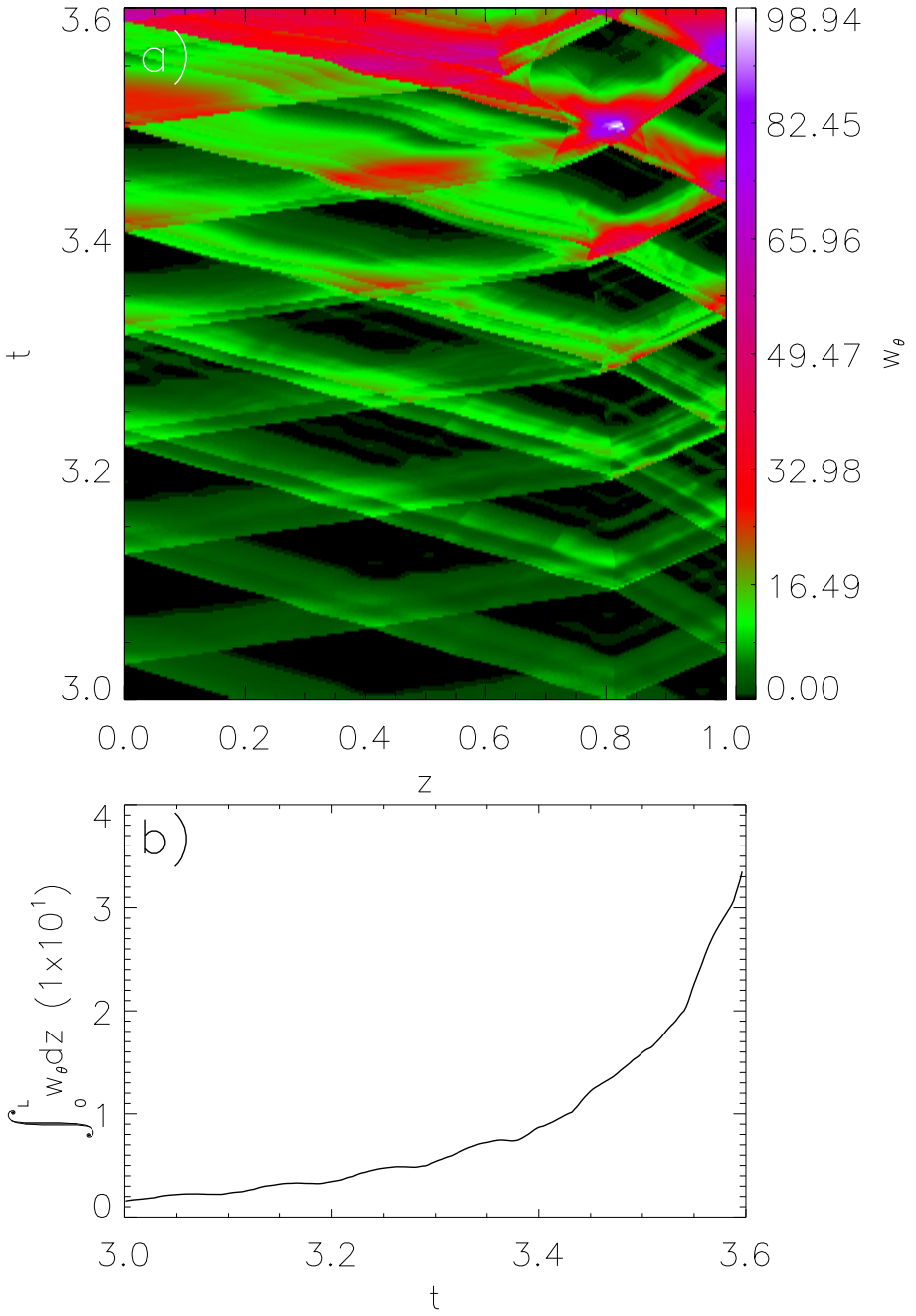

Figure 4.8: Time-distance plot for the θ-energy component, given by equation (4.10) in panel a). Panel b) shows the total W_θ within the loop.

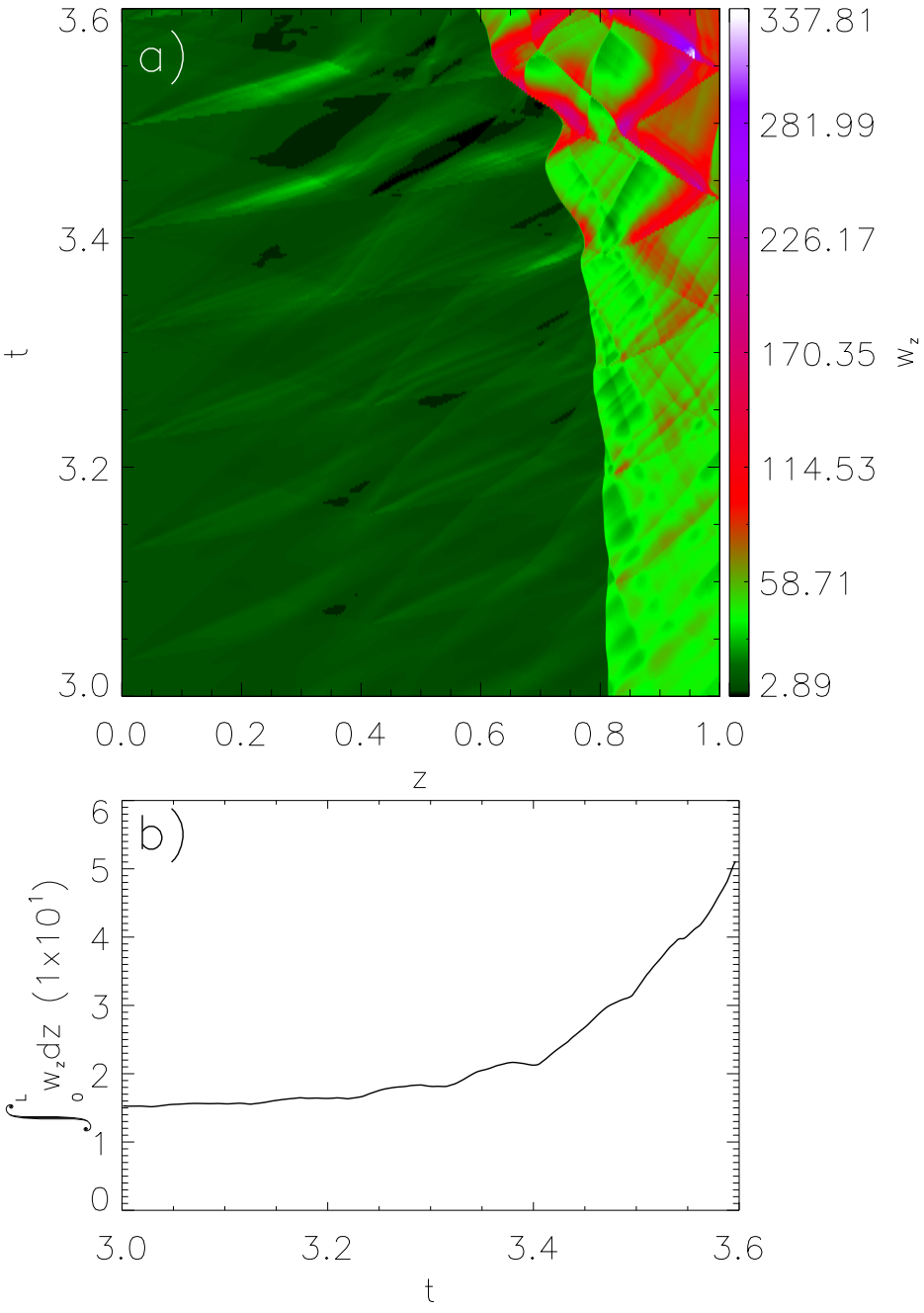

Figure 4.9: Panel a) shows the time-distance plot for the total longitudinal energy given by equation (4.11). The corresponding integral along the length of the loop is shown in panel b).

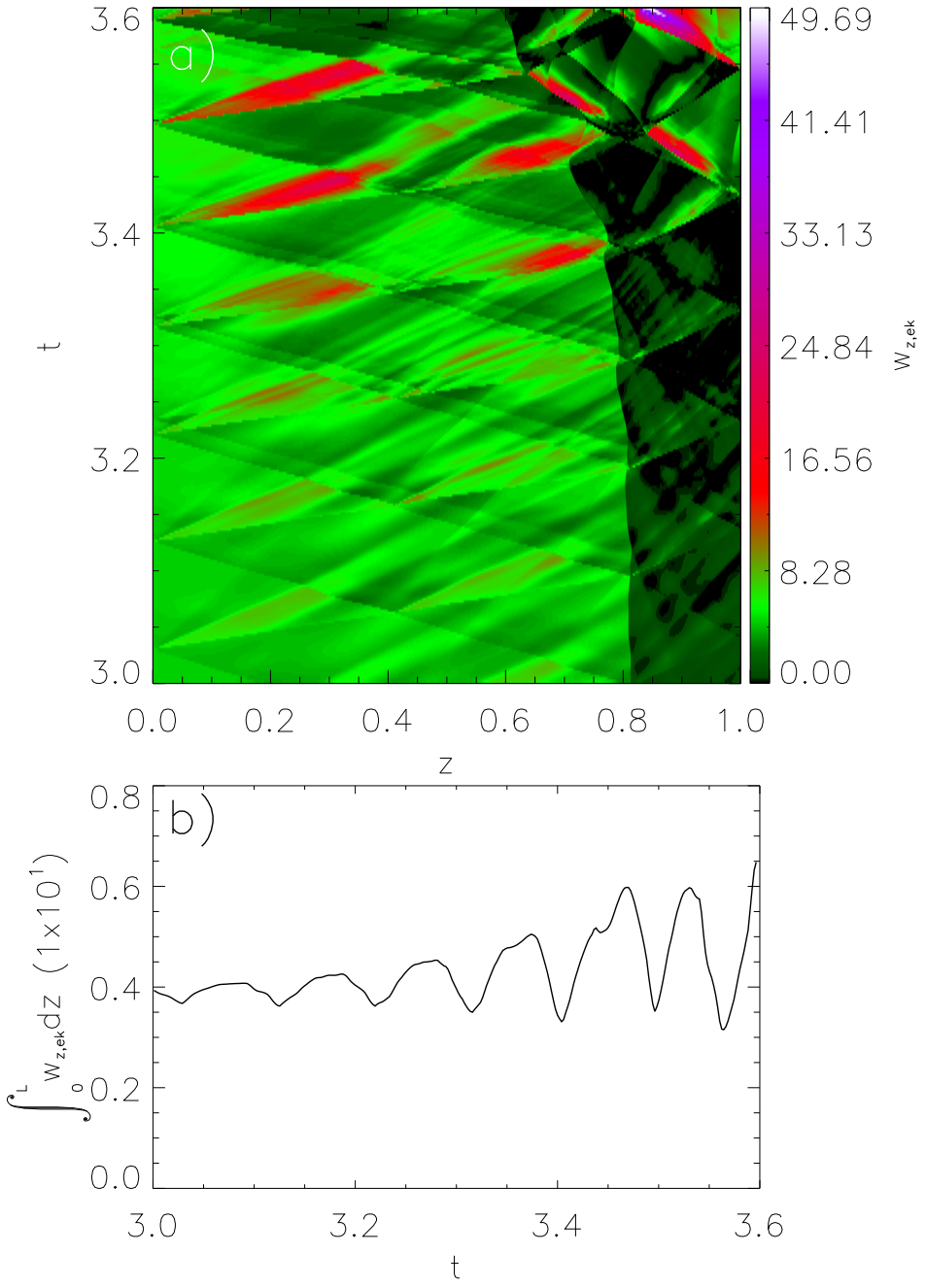

Figure 4.10: a) Time-distance plot of the first term on the RHS of equation (4.11), W_{zk}. The corresponding integral from $0 - L$ is shown in panel b).

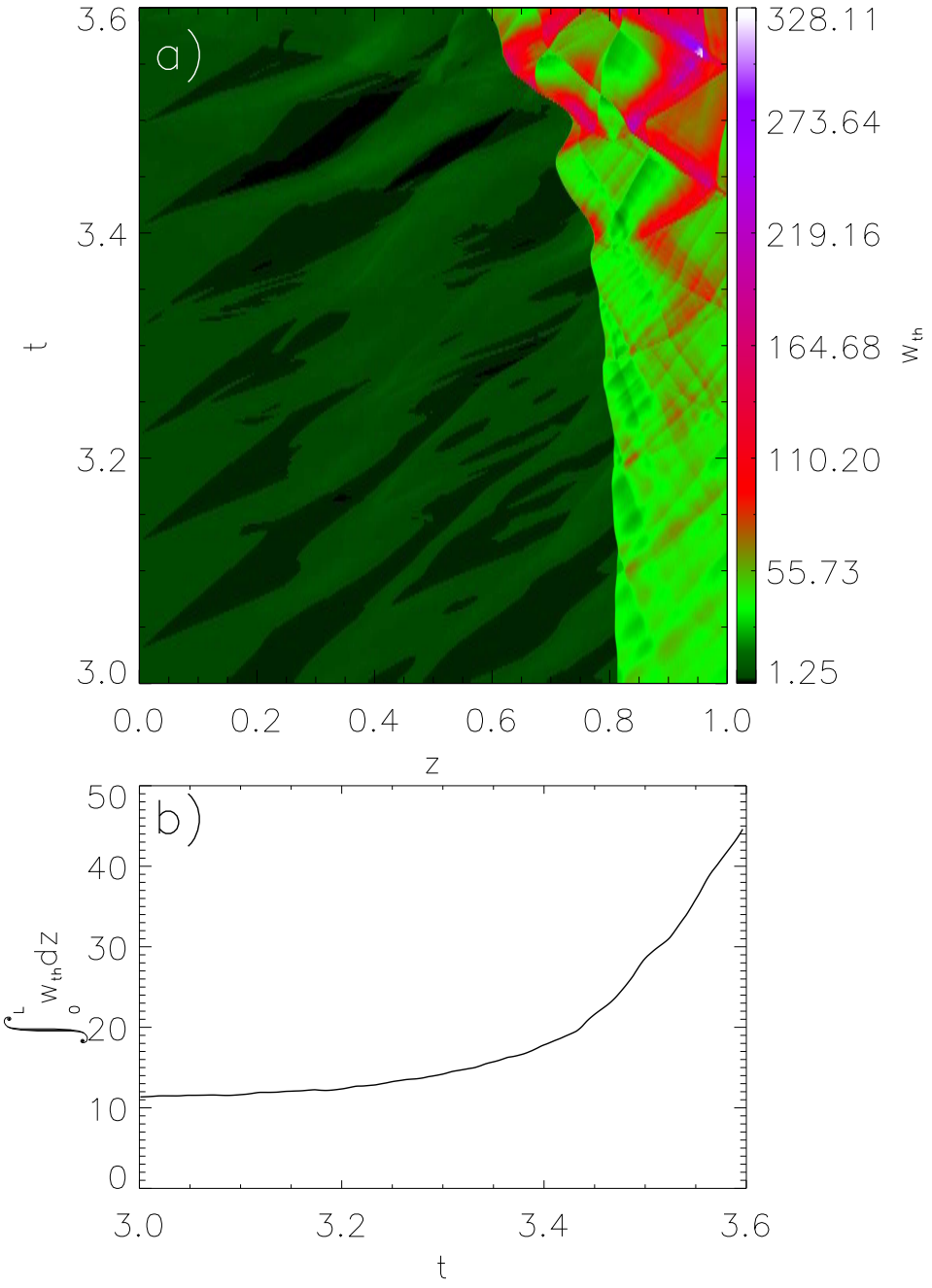

Figure 4.11: The same as Figure 4.10 but for the second term on the RHS of equation (4.11), W_{th}.

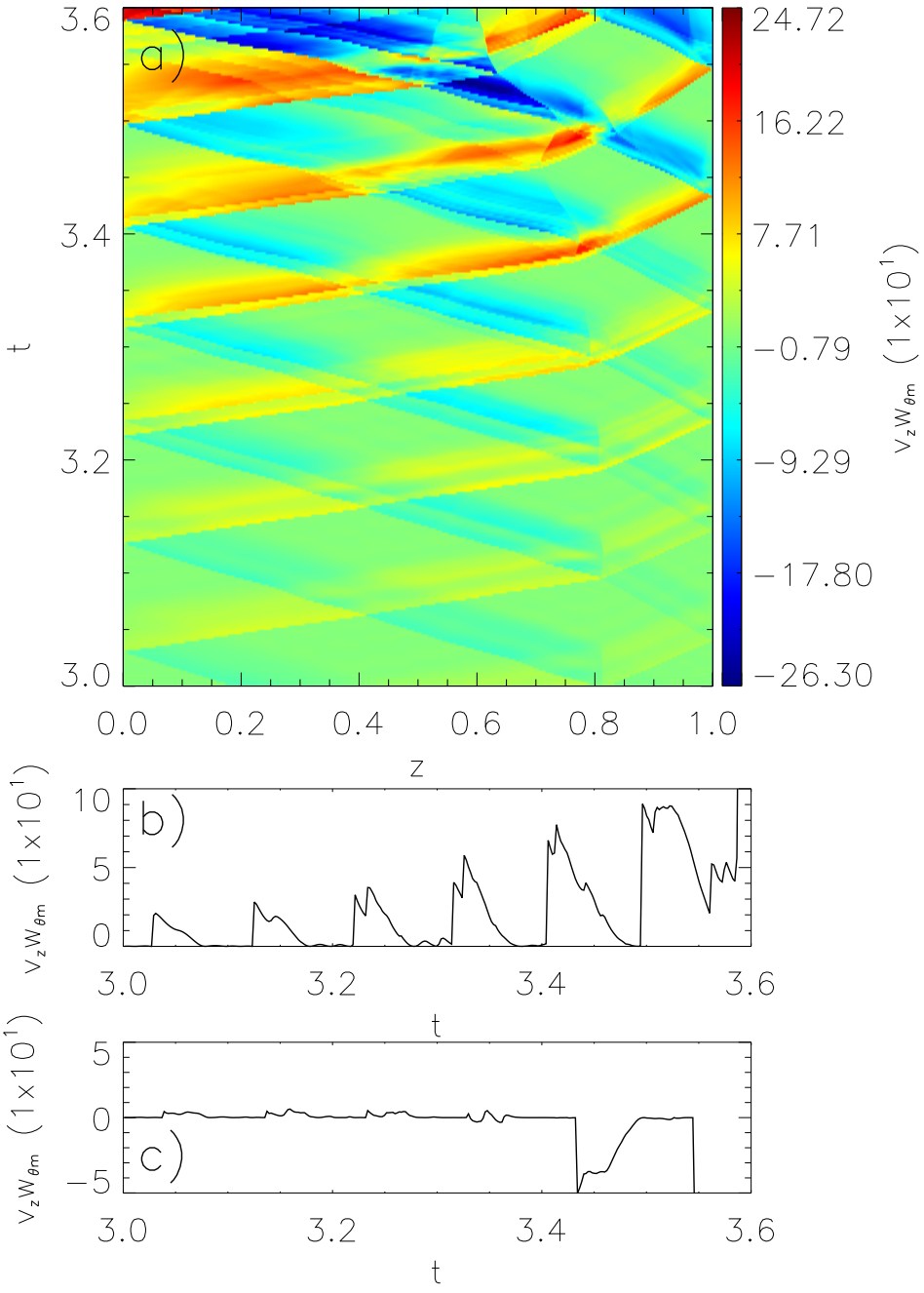

Figure 4.12: a) Time-distance plot for the magnetic flux, $v_z W_{\theta m}$. The flux at $z = 0.167\,L$ and $z = 0.834\,L$ are shown in panels b) and c).

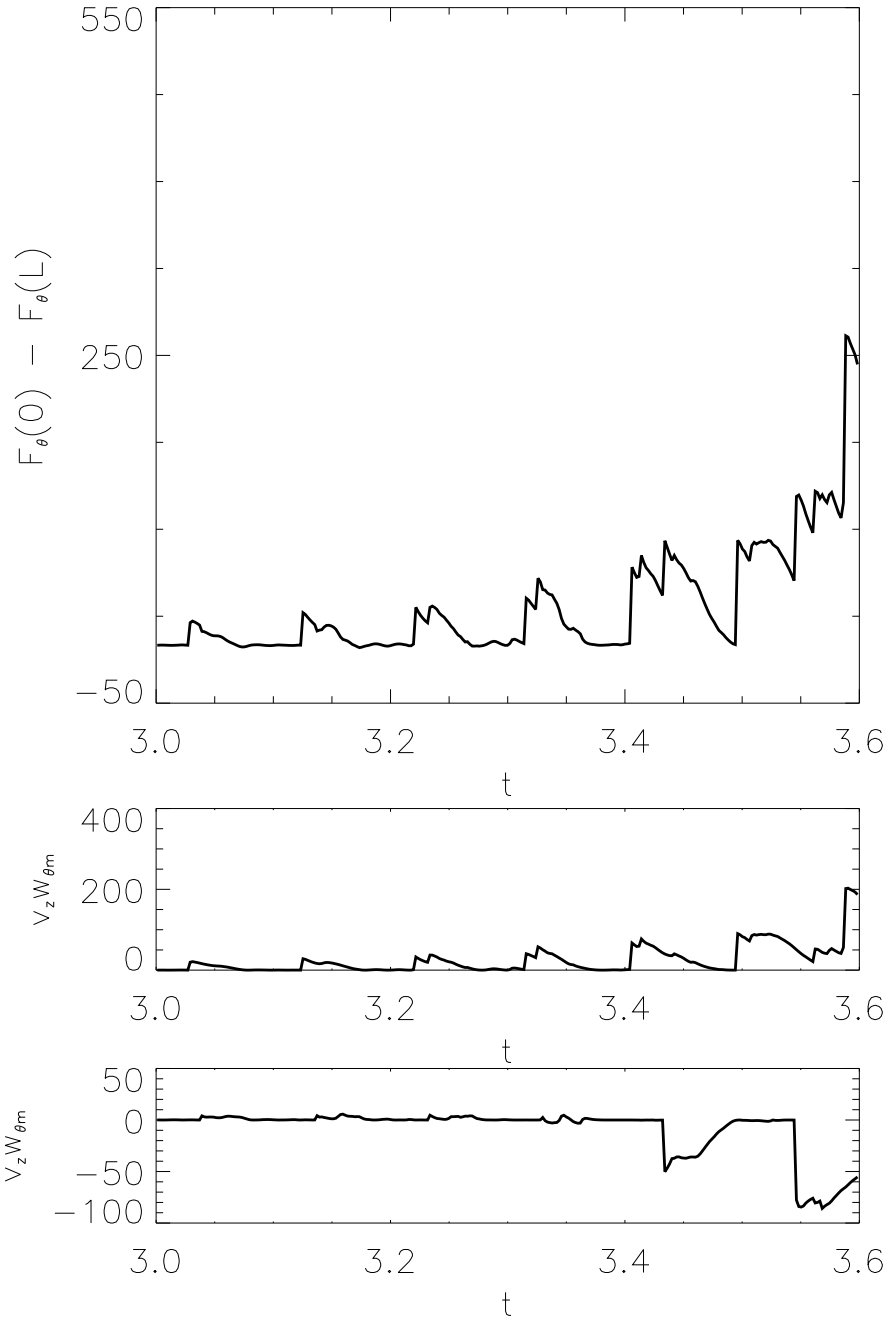

Figure 4.13: *Top*: the difference in magnetic flux between the two footpoints. *Middle*: magnetic flux at the $z = 0$ footpoint. *Bottom*: magnetic flux at the $z = L$ footpoint.

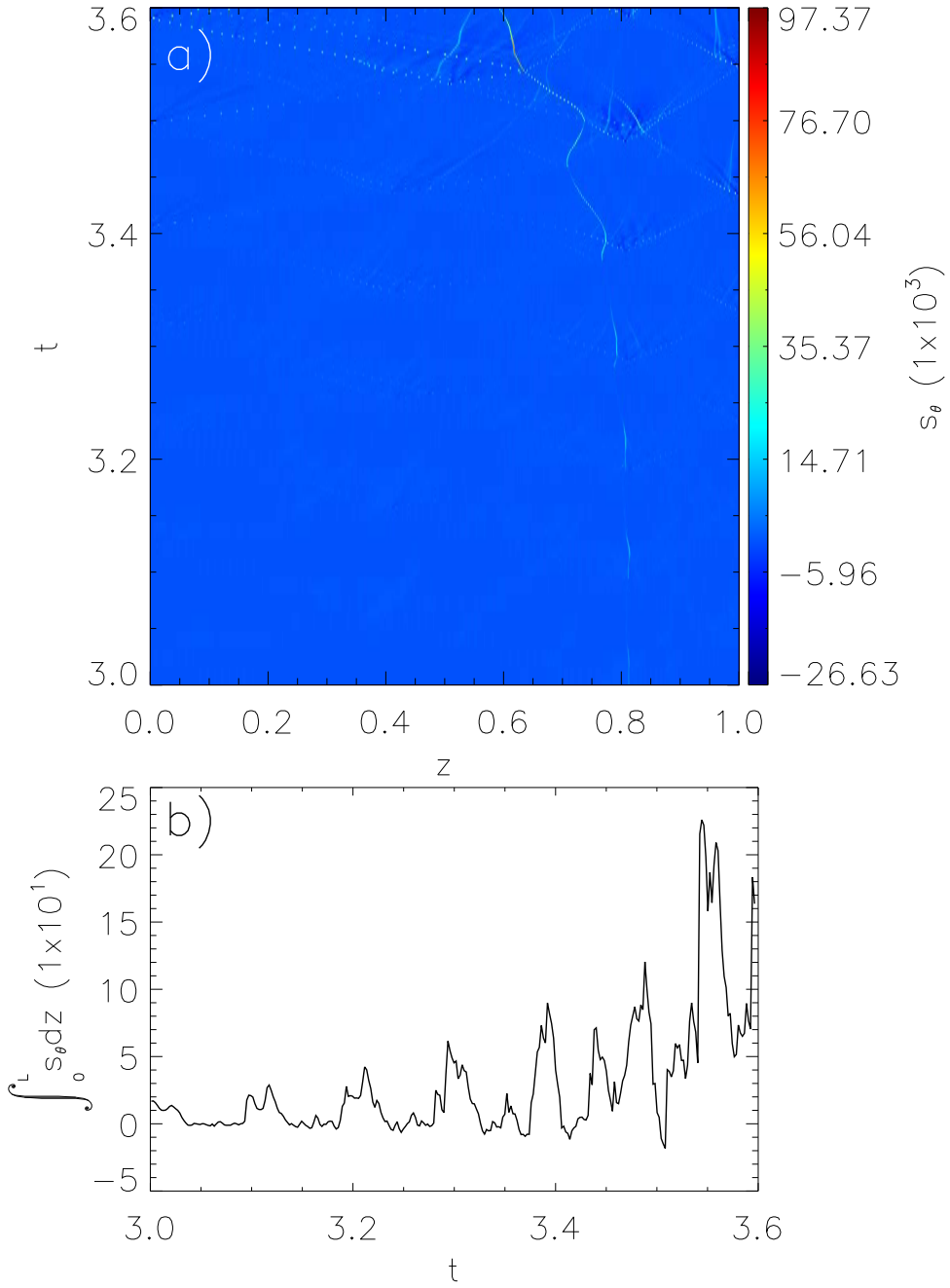

Figure 4.14: Panel a) shows the time distance plot of the source term (4.12). The integral along the length of the loop for s_θ is shown in b).

the non-linear process most drastically alters the flux tube and requires a more rigorous analysis. For this, the expressions (4.10) - (4.13) are used to generate several time-distance plots (Figures 4.8 - 4.14).

Figure 4.8 shows that the total azimuthal energy increases in an exponential manner during $t = 3 - 3.6\ L/c_{S1}$. The top panel shows that the propagating waves amplify upon interaction with the HD shock as well as the two footpoints at $z = 0$, and $z = L$. There is also amplification in W_θ when two waves propagating in opposite directions interact with each other. The azimuthal energy sees its greatest magnitudes in the downstream plasma (both immediately after the shock, and at the $z = L$ footpoint). The propagating sound waves/shocks that form as a consequence of the Alfvén waves lead to periodic increases in W_z in the upstream plasma as they are reflected from the $z = 0$ footpoint (Figure 4.9). Figure 4.10 shows that the kinetic energy term of equation (4.11) dominates in the upstream plasma, whilst Figure 4.11 shows that the thermal energy dominates W_z in the downstream plasma.

Around $t = 3.3 - 3.4\ L/c_{S1}$, the Alfvén waves interact with the downstream plasma, converting kinetic energy (Figure 4.10) into azimuthal energy (kinetic and magnetic; Figure 4.8) and thermal energy (Figure 4.11). As the waves interact with the $z = L$ boundary, the footpoint alternates between being a region of outflow and inflow. A large wave propagates through the HD shock at $t \approx 3.35\ L/c_{S1}$, which sufficiently disturbs the pressure balance either side of the stationary shock and causes it to move slowly towards $z = 0$. As the pulse is reflected at $z = L$, the non-linear coupling is sufficient to turn the outflow to a strong inflow at the boundary. This reaches a maximum of $-2.85\ c_{S1}$.

This conversion of an outflow to an inflow leads to an increase in ρ. As this strong pulse reaches the HD shock, another Alfvénic shock reaches the stationary shock. The three interact and somewhat quell the two Alfvénic shocks. The Alfvénic shock propagating in the positive direction converts the kinetic energy of the flow to magnetic energy. This conversion gradually leads to the $z = L$ footpoint becoming a region of permanent influx, matching $z = 0$. In turn, this additional

influx from $z = L$ is what leads to the accumulation of mass downstream of the HD shock. The flow reversal also leads to enhanced influx of azimuthal magnetic energy through the two footpoints (equation 4.9).

If we look at the azimuthal energy flux at the two footpoints, which is given as $v_z W_{\theta m}$, it becomes clear that the net influx seen in Figures 4.12, and 4.13 arises due to the presence of the HD shock. From Supplementary Movie 4, B_θ is approximately the same at $z = 0$ and $z = L$, but v_z is not. This means the difference in azimuthal energy flux, i.e., the larger influx at $z = 0$ than outflux at $z = L$, is caused by the presence of the stationary shock. If there was no classical shock, and given that gravity is not present, the flow would travel at the same speed along the entire loop. Thus, there would be no net energy flux as the total influx and outflux at the footpoints would be equivalent and therefore the azimuthal energy density would remain constant.

Now consider the induction equation (4.5) and integrate it over the length of the loop, 0 to L:

$$\frac{\partial}{\partial t}\left(\int_0^L B_\theta \, dz\right) + \int_0^L \frac{\partial}{\partial z}\left(v_z B_\theta\right) \, dz = \int_0^L B_\theta \frac{B_0}{\mu_0}\frac{\partial v_\theta}{\partial z} \, dz. \tag{4.22}$$

Applying the limits yields:

$$\frac{\partial B_{\theta T}}{\partial t} + \left[v_z B_\theta\right]_0^L = \left[\frac{B_0}{\mu_0} v_\theta\right]_0^L, \tag{4.23}$$

where $B_{\theta T}$ denotes the total azimuthal magnetic flux. A consequence of the pure reflection imposed by the Dirichlet boundaries is that $v_\theta = 0$ at $z = 0$ and $z = L$. Thus, the RHS is 0, and the expression can be rearranged and expanded to:

$$\frac{\partial B_{\theta T}}{\partial t} = v_z\left(0\right) B_\theta\left(0\right) - v_z\left(L\right) B_\theta\left(L\right). \tag{4.24}$$

It can be seen from the time-distance plot (Figure 4.2) and the Supplementary Movie 4 that $B_{\theta T}$ increases along the entirety of the loop as the simulation develops. It follows from equation (4.24) that as the LHS increases, the RHS must also

be positive and increasing. Again, this means there is a net azimuthal magnetic influx between the two footpoints, and the net influx is responsible for the continual twisting of the magnetic field. The corresponding increase in the azimuthal magnetic energy can be seen in Figure 4.8.

Whilst we have seen that the footpoints are a source of amplification for the Alfvén waves and subsequently the non-linear processes, it is important to note that the role of the HD shock is more important than merely providing the conditions for asymmetric flux to arise. If we consider the source term described by equation (4.12) and its subsequent plot (Figure 4.14) then it is clear that there is amplification at the shock front too. This can be seen in Figure 4.14 as the brightenings in panel a) when the Alfvén waves interact with the shock. This happens due to the flow having a negative gradient at the shock front. This means s_θ will be large at the shock when a twist is present. As the magnetic twists become more prevalent, s_θ becomes significant within the loop where Alfvénic waves propagate into one another. The source term is notably a region of localised amplification, i.e., it only becomes prominent in regions of strong, negative flow gradients. If the gradient is positive, then s_θ would convert magnetic energy into kinetic energy.

If we compare the net energy flux caused by the asymmetry of the siphon flow between the two footpoints (Figure 4.13) with s_θ (Figure 4.14), then it becomes clear that both play a major role in the amplification of the Alfvén waves. That is, neither one or the other provide more energy to the Alfvén waves. However, it is important to remember that without the presence of the flow gradient, neither mechanism would operate.

4.5 Discussion

In this chapter we have demonstrated the effects of the Alfvén instability within a highly-inclined loop. As with our previous study [Williams et al., 2016], the Alfvén wave gains magnetic energy from the conversion of kinetic energy of the flow and from the net influx of azimuthal energy through the footpoints. This process is somewhat reminiscent of Fermi acceleration (1^{st} order), or diffusive

shock acceleration. That is, where charged particles undergo acceleration through repeated reflection by a magnetic mirror. It is thought to be the primary mechanism by which particles gain non-thermal energies in astrophysical shock waves. In our case, the classical shock acts as a magnetic mirror, allowing constant amplification of the Alfvén waves upon reflection.

The introduction of a second Dirichlet boundary means the conditions for amplification are no longer restricted to an instability criterion [Taroyan, 2008; Williams et al., 2016, for example]. This allows for almost any $\frac{v_z}{c_A}$ ratio to generate an instability leading to amplification of an Alfvén wave or wave-train.

As is common with siphon flows, our model exhibits asymmetric flux between the $z = 0$ and $z = L$ footpoints. This asymmetry arises due to the difference in flow speed between the two footpoints and is a consequence of the hydrodynamic shock in the descending leg of the loop. If we consider equation (4.13), it can be seen that for the azimuthal energy to increase, the RHS has to be positive. This means amplification may occur due to a net influx of azimuthal energy between the footpoints,

$$F_\theta(0) - F_\theta(L) > 0,$$

or through wave-flow coupling,

$$s_\theta = -\int_0^L \frac{\partial v_z}{\partial z}\frac{b_\theta^2}{2\mu_0} > 0.$$

In the presence of negative flow gradients, s_θ is positive - in this case, at the shock interface. This means the Alfvén wave extracts kinetic energy from the flow and converts it to magnetic energy as it interacts with the shock. The energy provided by the net influx at the footpoints and wave-flow coupling at the shock interface are approximately equal. As such, it is impossible to say one source is more important than the other during the amplification process.

The non-linear coupling between the θ-components and z-components in equations (4.3) and (4.4) allows the formation of propagating waves, both fast- and

slow-mode. These steepen into shock waves as the Alfvén waves amplify further.

A consequence of the non-linear Alfvén waves is the conversion of the footpoint at $z = L$ from an outflow to a source of inflow. This upflow reaches similar velocities, ≈ 20 km s^{-1} as those observed by Berger et al. [2008]. Subsequently, this new source of inflow 'pulls' photospheric plasma through the footpoint into the loop. This leads to the mass accumulation seen where $\rho_{max} \approx 6.87 \times \rho_{max}|_{t=0}$. This influx, along with the Alfvén waves, alters the magnetic and thermal pressures to the point where the classical shock propagates towards the $z = 0$ footpoint. The initial upstream plasma ($z = 0$ to $z = 0.8\,L$) sees a density increase of $\times 30$ as the downstream plasma spreads along the loop due to the shock propagation.

During the simulation it can be seen that a twist velocity that exceeds 35 km s^{-1} and reaches a maximum greater than 50 km s^{-1} within the simulated loop. This leads to $B_\theta \approx 4.9 \times B_z$, meaning that the magnetic field strength within the loop increases from 39.1 G to $\approx$ 231 G. However, in a multidimensional study, the twist is unlikely to reach these levels of amplification as it is likely some form of eruption would occur - possibly due to the loop becoming kink unstable such as in Török and Kliem [2005]. Reducing the Alfvén speed would allow for a weaker initial B-field, meaning the induced magnetic twist would also be smaller, and more similar to that seen in prominences.

The inclusion of gravity would allow the study of a loop structure that is not highly-inclined. This would mean that the simulated loop would be gravitationally stratified, and the Alfvén speed would increase along the ascending leg of the loop towards the apex where it would reach a maximum. The Alfvén speed would then decrease along the descending leg (in the $+z$ direction) back towards the photosphere. Conversely, the flow speed would decelerate in the ascending leg of the loop but increase in the descending leg. The effects of stratification on the Alfvén speed, along with gravity acting with/against the flow in the descending/ascending leg of the loop require study. Depending on the ratio of the flow/Alfvén speed, and the position at which a HD shock forms, the inclusion of gravity could either accelerate or hinder the amplification process.

4.6 Conclusion

Using our 1.5-D MHD model of an isolated, highly-inclined loop, we have shown that the Alfvén instability may amplify Alfvén waves in the presence of a supersonic flow. The Alfvén waves amplify upon reflection at the footpoints due to the asymmetric flux caused by the siphon flow. The Alfvén waves also amplify upon interaction and reflection with the stationary shock due to the wave-flow coupling. It is shown that the asymmetric flux through the footpoints and wave-flow coupling at the shock provide the Alfvén waves with comparable energy for amplification.

The non-linear coupling of equations (4.2) and (4.4) becomes prominent as the Alfvén waves continue to bounce and amplify between the shock and footpoints. The coupling leads to secondary fast- and slow-mode waves being generated within the loop. These lead to increased flow speeds of up to $\approx 50 - 70$ km s^{-1}.

The twist velocities within the simulated loop reach up to $\approx$ 50 km s^{-1}, and continually twist the magnetic field in the same direction. This behaviour is similar to the rotation/swirls seen in prominence tornadoes [Li et al., 2012]. The result is a global magnetic twist where $B_\theta \approx 4.9 \times B_z$, which increases the field strength from 39.1 G to $\approx$ 231 G.

As these magnetic twists reach the $z = L$ footpoint, they convert the region from a source of outflow to inflow. This conversion of flow direction leads to upflows of $\approx$ 20 km s^{-1}, matching observational upflows [Berger et al., 2008]. Subsequently, the Alfvén waves/plasma flow 'pull' photospheric material into the loop, leading to mass accumulation. The density increases by a factor of 30 as a result of the non-linear coupling. The examined novel mechanism for the formation of a twisted flux tube with enhanced density may play an important role in prominence formation. However, multidimensional studies with the inclusion of gravity combined with spectral observations of prominence formation are required for conclusive evidence.

Chapter 5

Concluding Remarks and Future Work

Flux tubes form the basis of many structures within the Sun and its atmosphere. In the photosphere, these flux tubes have been witnessed in sunspot regions, granules, and intergranular lanes. Chromospheric examples include spicules, jets, and magnetic swirls often dubbed as solar/prominence tornadoes. Filaments, prominences, and loops are some examples of flux tube structures in the corona.

Observations have shown that the solar atmosphere is highly dynamic due to the constant motion of plasma. This means short- and long-lived structures often exhibit flows. In the photosphere this can be seen in sunspots through the Evershed effect and is often interpreted as a siphon flow that emanates from the deep penumbra and travels radially outwards to the outer penumbra. The siphon flow model has also been suggested as a mechanism for plasma flows within large structures such as coronal loops. In the chromosphere many transient, vertical structures exhibit flows along the magnetic field lines (*e.g.* Type-I/Type-II spicules) where the structures reach coronal heights but display chromospheric properties such as temperature and density. In addition to this upward plasma flow, spicules are seen to sway back and forth and display simultaneous red and blue-shifts, leading to non-thermal broadening of spectral lines. This suggests spicules may play a key role in energy transport between the photosphere and corona due to the presence of Alfvén waves and their ability to carry large quantities of energy along magnetic field lines.

All that said, the study of Alfvén waves within flowing plasma is not well documented in the current literature. Many numerical studies focus on flows generated by the Alfvén waves for a flux tube structure that is in hydrostatic equilibrium. This thesis aims to fill the void and investigates what may happen to Alfvén waves when a plasma flow already exists within a flux tube. Numerical codes VAC, and LCPFCT have been implemented to model the behaviour of the wave-flow interaction in MHD systems.

For a flux tube with an ever-present flow, this thesis has shown that an instability exists whereby Alfvén waves may become amplified by harnessing the kinetic energy of the flow and converting it into magnetic twist. This instability caused by the flowing plasma can amplify minute Alfvén waves from small, linear perturbations into large amplitude waves that drastically perturb the plasma through non-linear coupling of the MHD equations. The work presented is split into three main constituents and a brief overview of each chapter follows.

The first topic models a nearly horizontal flux tube with a supersonic yet sub-Alfvénic flow propagating along its length. The geometry of this problem is akin to the Evershed flow within sunspot penumbrae. The flow is subject to a classical shock, which is set-up using the Rankine-Hugoniot jump conditions. A single Alfvén wave is launched from the photosphere and becomes trapped between the dense-photosphere and shock. Here, it continually amplifies upon interaction with the classical shock, where it converts kinetic energy of the flow into magnetic twist. This is the first numerical example of Alfvén wave amplification due to their interaction with a classical shock. The non-linear processes disturb the pressure balance around the shock as the wave amplifies, creating slow and fast shock waves. Interestingly, part of the Alfvén wave is transmitted through the shock upon each interaction and as it propagates through the downstream plasma, partially converts some of its magnetic energy back into kinetic energy of the flow. This shows that Alfvén waves can act as a mode of energy transport between two regions and also generate a globally twisted flux rope where $B_\theta \approx B_z$.

A parameter study is conducted to investigate how the flow speed effects the amplification process (provided it satisfies the inequality given in §2.6). It is found that the rate of amplification and subsequently, the maximum twist amplitude seen, increases as $v_z \to c_A$. Alfvén waves with larger periods of oscillation are shown to increase the amplification rate but do not yield larger values for $|v_\theta|_{max}$ or $B_{\theta\,max}$.

The second topic is a linear study that investigates Alfvén wave amplification within an intergranular downflow. The key result here is that it is shown, both numerically and analytically, that Alfvén waves are amplified globally by the existence of decelerating downflows. If the Alfvén and flow speeds vary at alternate rates such that there becomes a location where the two are equal as the flow goes from super- to sub-Alfvénic speeds, then an instability may arise. That is, an Alfvén wave that is propagating against the flow will amplify indefinitely. This is regardless of where its point of origin is as it will either propagate until it grinds to a halt, or it will be swept to the critical point by the flow. This continuous twisting is a magnetic analogy of vortex motions seen in granular lanes.

Once again, a parameter study is conducted. Here, the rate of flow is altered such that the equipartition level is placed at various depths, z. This allows the study of flow rate on the amplification process to be conducted. It is shown that the Alfvén wave amplifies for flow speeds as small as $u_0\,(0) = 0.2\,c_S$ as well as for unrealistically large flow speeds ($u_0\,(0) = 7\,c_S$). It is seen that the initial amplification rate is quicker when the flow speed is larger at the equipartition level. Launching the Alfvén wave from the super-Alfvénic region as opposed to the sub-Alfvénic region leads to the wave being unable to propagate upwards against the flow ($c_A < u_0$). Subsequently, the wave is swept back down the flux tube to the equipartition level whilst simultaneously undergoing amplification.

The linear model presented may be considered a magnetic analogy to vortices seen in intergranular lanes and magnetoconvection simulations. In the non-linear regime it is believed that this mechanism will perturb the longitudinal variables due to the coupling of the MHD equations. This could lead to small Alfvén waves

being amplified to non-linear Alfvénic pulses which then get released into the upper atmosphere. This could be due to the flow being transient or because the wave-flow coupling decreases the flow speed sufficiently that the Alfvénic pulse may freely propagate vertically. The upward propagating swirl could behave like a solar tornado or it could incite an upflow as it propagates through the chromosphere and result in a spicule-like structure being formed.

The final piece of work is an extension of the first topic. Here, rather than having an open-ended flux tube, a highly inclined loop is now studied. Both ends of the flux tube are firmly rooted in the dense-photosphere. A supersonic yet sub-Alfvénic flow propagates from the $z = 0$ to $z = L$ footpoint and undergoes a classical shock in the descending leg of the loop.

An implication of the $z = L$ footpoint being rooted in the dense-photosphere is that any ratio of v_z/c_A leads to an instability by which Alfvén waves are amplified. Thus, the criterion required for instability to occur in the sunspot model is no longer required. The only prerequisite on the flow speed is that it is supersonic and undergoes a shock. Otherwise, the flow can have any speed, even super-Alfvénic speeds should result in amplification.

In this model, the amplification is much stronger than the sunspot model. This is because there is now asymmetric flux as well as the wave-flow coupling at the shock interface. These two mechanisms yield a global twist generation of $B_\theta \approx 5B_z$. In the downstream plasma it can be seen that the non-linear coupling between the Alfvénic pulse and flow gradually converts the $z = L$ footpoint from a region of outflow to one of inflow. This twisting and subsequent flow reversal leads to mass loading along the loop where the initial density sees an increase of $\rho \approx 30 \times \rho_{t=0}$.

These three studies clearly show that coupling between Alfvén waves and flowing plasmas, in both the linear and non-linear regimes, exists. This coupling leads to amplification (repression) of Alfvén waves when a negative (positive) flow gradient is present. This coupling and a negative flow gradient is what leads to

amplification when Alfvén waves interact with a classical shock in the sunspot and prominence models. It also explains amplification of Alfvén waves propagating against a decelerating downflow in the linear model. When the coupling leads to large amplitude waves in the non-linear regime, fast- and slow-mode waves which steepen into shocks become coupled to the propagating Alfvénic pulses. These perturb the original plasma properties of the flux tube, leading to shock destabilisation and global twist generation. This twist leads to a flux rope being formed.

In the prominence model the level of twist generated is $B_\theta \approx 5B_z$ compared to $B_\theta \approx B_z$ in the sunspot model. This increase in twist results in flow reversal at the $z = L$ footpoint, which is not present in the sunspot model. The flow reversal leads to mass loading along the flux tube. This is an implication of the $z = L$ end of the flux tube being rooted in the photosphere, *i.e.* becoming a reflective boundary compared to an open boundary. As such, the background flow becomes akin to the siphon flow model and asymmetric flux is generated between the two footpoints. This asymmetric flux is another source of amplification in the prominence model and allows for greater twist amplitudes to form as less energy leaves the modelled flux tube. The amount of amplification generated by the asymmetric flux is proportional to that generated by the wave-flow coupling as the Alfvén waves over-reflect at the shock interface.

Further work is required on the coupling of Alfvén waves and flowing plasma. The large twist generated by the models presented in this thesis suggest that in multidimensional studies, an eruptive event would occur but in 1.5-D the magnetic field may twist indefinitely. This is especially true with the prominence model. In addition to this, the intergranular downflow model has shown that stratification can lead to non-constant plasma flows that amplify Alfvén waves. The inclusion of gravity for a fully non-linear system is needed. This would allow the study of near-vertical structures and possibly provide an insight on whether flows may play a role in the energy transport between the photosphere and corona. Additionally, other complexities will need investigating such as how the wave-flow interactions alter when the flow is transient, or when ion-neutral damping is in-

cluded in the MHD equations to simulate a partially ionised chromosphere. In the sunspot model it is seen that a large quantity of flux is generated, which could potentially heat the solar atmosphere. It would be interesting to see how this generation of flux upholds for vertical, stratified structures and whether the mechanism can overcome radiative losses.

Appendix A

Reduction of the VAC MHD Equations

In this section, the simplification of the default VAC MHD equations to the ones employed in the simple, 1.5-D model is shown. A flux tube of constant radius, which does not have gravitational stratification or a varying magnetic field is considered. It is assumed that the longitudinal magnetic field strength, B_x is strong enough to withstand any contraction or expansion of the flux tube cross-sectional area. The default MHD equations (1.1) - (1.4) within VAC are given by:

$$\frac{\partial \rho}{\partial t} + \nabla \cdot (\mathbf{v}\rho) = 0, \tag{1.1}$$

$$\frac{\partial}{\partial t}(\rho \mathbf{v}) + \nabla \cdot (\mathbf{v}\rho\mathbf{v} - \mathbf{B}\mathbf{B}) + \nabla \mathrm{p}_{\mathrm{tot}} = -(\nabla \cdot \mathbf{B})\,\mathbf{B}, \tag{1.2}$$

$$\frac{\partial e}{\partial t} + \nabla \cdot (\mathbf{v}\mathrm{e} - \mathbf{B}\mathbf{B} \cdot \mathbf{v} + \mathbf{v}\mathrm{p}_{\mathrm{tot}}) = -(\nabla \cdot \mathbf{B})\,\mathbf{B} \cdot \mathbf{v} + \nabla \cdot (\mathbf{B} \times \eta\mathbf{J}), \tag{1.3}$$

$$\frac{\partial \mathbf{B}}{\partial t} + \nabla \cdot (\mathbf{v}\mathbf{B} - \mathbf{B}\mathbf{v}) = -(\nabla \cdot \mathbf{B})\,\mathbf{v} - \nabla \times (\eta\mathbf{J}). \tag{1.4}$$

The starting point here will be the continuity equation (1.1). For a Cartesian

coordinate system,

$$\nabla \cdot \mathbf{F} = \frac{\partial X}{\partial x} + \frac{\partial Y}{\partial y} + \frac{\partial Z}{\partial z}, \tag{1}$$

where $\mathbf{F} = X\mathbf{e_x} + Y\mathbf{e_y} + Z\mathbf{e_z}$. However, as the system modelled employs 1.5-D geometry, equation (1) simply becomes:

$$\nabla \cdot \mathbf{F} = \frac{\partial X}{\partial x}, \tag{2}$$

as there is no dependency on y or z. This means the continuity equation (1.1) for 1.5-D simplifies to:

$$\frac{\partial \rho}{\partial t} + \frac{\partial}{\partial x}(\rho v_x) = 0. \tag{2.27}$$

For the momentum equation (1.2), the term $(\nabla \cdot \mathbf{B})\,\mathbf{B} = 0$ as B_x remains constant in space and time, *i.e.* $\frac{\partial B_x}{\partial t} = \frac{\partial B_x}{\partial x} = 0$. Thus, equation (1.2) becomes:

$$\frac{\partial}{\partial t}(\rho \mathbf{v}) + \nabla \cdot (\mathbf{v}\rho\mathbf{v} - \mathbf{B}\mathbf{B}) + \nabla \mathrm{p_{tot}} = 0. \tag{3}$$

The second term can be split into two parts:

$$\frac{\partial}{\partial t}(\rho \mathbf{v}) + \nabla \cdot (\mathbf{v}\rho\mathbf{v}) - \nabla \cdot (\mathbf{B}\mathbf{B}) + \nabla \mathrm{p_{tot}} = 0. \tag{4}$$

The first term of equation (4) can be expanded to the following:

$$\frac{\partial}{\partial t}(\rho \mathbf{v}) = \frac{\partial}{\partial t}(\rho v_x)\,\mathbf{e_x} + \frac{\partial}{\partial t}(\rho v_y)\,\mathbf{e_y}. \tag{5}$$

The divergence of a dyadic product can be solved using the following identity:

$$\nabla \cdot (\mathbf{A}\mathbf{B}) = (\nabla \cdot \mathbf{A})\,\mathbf{B} + \mathbf{A} \cdot (\nabla \mathbf{B}), \tag{6}$$

which is used to solve terms 2 and 3 of equation (4).

$$\nabla \cdot (\mathbf{v}\rho\mathbf{v}) = (\nabla \cdot \mathbf{v}\rho)\,\mathbf{v} + \rho\mathbf{v} \cdot (\nabla \mathbf{v}) = (\nabla \cdot \mathbf{v})\,\rho\mathbf{v} + (\rho\mathbf{v} \cdot \nabla)\,\mathbf{v}. \tag{7}$$

Equation (7) is split into x and y components to give:

$$(\nabla \cdot \mathbf{v})\,\rho\mathbf{v} + (\rho\mathbf{v} \cdot \nabla)\,\mathbf{v} = \left(\frac{\partial v_x \rho}{\partial x}\right)\mathbf{v} + \left(v_x \frac{\partial}{\partial x}\right)\rho\mathbf{v}$$
$$= \frac{\partial v_x \rho}{\partial x} v_x \mathbf{e_x} + \frac{\partial v_x \rho}{\partial x} v_y \mathbf{e_y} + \rho v_x \frac{\partial v_x}{\partial x}\mathbf{e_x} + \rho v_x \frac{\partial v_y}{\partial x}\mathbf{e_y}. \quad (8)$$

Similarly, the third term of equation (4) can be split into x and y components:

$$\nabla \cdot (\mathbf{BB}) = (\nabla \cdot \mathbf{B})\,\mathbf{B} + \mathbf{B} \cdot (\nabla \mathbf{B}) = (\mathbf{B} \cdot \nabla)\,\mathbf{B} = B_x \frac{\partial B_x}{\partial x}\mathbf{e_x} + B_x \frac{\partial B_y}{\partial x}\mathbf{e_y}, \quad (9)$$

and as B_x is constant, this simply becomes:

$$B_x \frac{\partial B_x}{\partial x}\mathbf{e_x} + B_x \frac{\partial B_y}{\partial x}\mathbf{e_y} = B_x \frac{\partial B_y}{\partial x}\mathbf{e_y}. \quad (10)$$

The fourth and final term of equation (4) yields:

$$\nabla p_{tot} = \frac{\partial p_{tot}}{\partial x}\mathbf{e_x}. \quad (11)$$

An expression for total momentum can be obtained by substituting terms (5), (8), (10), and (11) into equation (4) to yield:

$$\frac{\partial}{\partial t}(\rho v_x)\,\mathbf{e_x} + \frac{\partial}{\partial t}(\rho v_y)\,\mathbf{e_y} + \frac{\partial v_x \rho}{\partial x} v_x \mathbf{e_x} + \frac{\partial v_x \rho}{\partial x} v_y \mathbf{e_y} + \rho v_x \frac{\partial v_x}{\partial x}\mathbf{e_x}$$
$$+ \rho v_x \frac{\partial v_y}{\partial x}\mathbf{e_y} - B_x \frac{\partial B_y}{\partial x}\mathbf{e_y} + \frac{\partial p_{tot}}{\partial x}\mathbf{e_x} = 0. \quad (12)$$

The $\mathbf{e_x}$ and $\mathbf{e_y}$ terms in equation (12) can now be collated to yield expressions for momentum in x and y:

$$\frac{\partial}{\partial t}(\rho v_x) + \frac{\partial}{\partial x}(v_x \rho v_x) = -\frac{\partial p_{tot}}{\partial x}, \quad (2.28)$$

$$\frac{\partial}{\partial t}\left(\rho v_y\right) + \frac{\partial}{\partial x}\left(v_x \rho v_y\right) = B_x \frac{\partial}{\partial x}\left(B_y\right). \tag{2.29}$$

Similarly for the energy equation (1.3), the terms on the RHS all reduce to 0 as $\nabla \cdot \mathbf{B} = 0$, the plasma resistivity, $\eta = 0$, and current density, $\mathbf{J} = 0$. Each of the divergence terms can be split to give:

$$\frac{\partial e}{\partial t} + \nabla \cdot (\mathbf{v}e) - \nabla \cdot (\mathbf{B}\mathbf{B} \cdot \mathbf{v}) + \nabla \cdot (\mathbf{v}p_{tot}) = 0. \tag{13}$$

The second term of equation (13) becomes:

$$\nabla \cdot (\mathbf{v}e) = \frac{\partial}{\partial x}\left(v_x e\right), \tag{14}$$

as there is no y coordinate. In the same way it can be shown that the third term of equation (13) becomes:

$$\nabla \cdot (\mathbf{B}\mathbf{B} \cdot \mathbf{v}) = \nabla \cdot [\mathbf{B}\left(\mathbf{B} \cdot \mathbf{v}\right)] = \nabla \cdot [B_x\left(B_x v_x + B_y v_y\right) + B_y\left(B_x v_x + B_y v_y\right)], \tag{15}$$

and due to there being no y coordinate and B_x being constant, this simply yields:

$$\nabla \cdot [B_x\left(B_x v_x + B_y v_y\right) + B_y\left(B_x v_x + B_y v_y\right)] = B_x \frac{\partial}{\partial x}(B_x v_x + B_y v_y). \tag{16}$$

The final term of equation (13) simplifies to:

$$\nabla \cdot (\mathbf{v}p_{tot}) = \frac{\partial}{\partial x}\left(v_x p_{tot}\right). \tag{17}$$

Substituting expressions (14), (16), and (17) into equation (13) yields the employed energy equation:

$$\frac{\partial}{\partial t}\left(e\right) + \frac{\partial}{\partial x}\left(v_x e\right) = B_x \frac{\partial}{\partial x}\left(v_x B_x + B_y v_y\right) - \frac{\partial}{\partial x}\left(v_x \mathrm{p_{tot}}\right). \tag{2.30}$$

The final equation to reduce is the induction equation (1.4). In much the same

way as with the previous equations, the divergence term can be split to give:

$$\frac{\partial \mathbf{B}}{\partial t} + \nabla \cdot (\mathbf{vB}) + \nabla \cdot (\mathbf{Bv}) = 0, \tag{18}$$

which expands to:

$$\frac{\partial \mathbf{B}}{\partial t} + (\nabla \cdot \mathbf{v})\,\mathbf{B} + \mathbf{v} \cdot (\nabla \mathbf{B}) - (\nabla \cdot \mathbf{B})\,\mathbf{v} - \mathbf{B} \cdot (\nabla \mathbf{v}) = 0, \tag{19}$$

and as $\nabla \cdot \mathbf{B} = 0$, this gives:

$$\frac{\partial \mathbf{B}}{\partial t} + (\nabla \cdot \mathbf{v})\,\mathbf{B} + \mathbf{v} \cdot (\nabla \mathbf{B}) - \mathbf{B} \cdot (\nabla \mathbf{v}) = 0. \tag{20}$$

Separating the vectors of equation (20) into their components results in:

$$\begin{aligned}\frac{\partial B_x}{\partial t}\mathbf{e_x} + \frac{\partial B_y}{\partial t}\mathbf{e_y} + \frac{\partial v_x}{\partial x}B_x\mathbf{e_x} + \frac{\partial v_x}{\partial x}B_y\mathbf{e_y} + v_x\frac{\partial B_x}{\partial x}\mathbf{e_x} \\ + v_x\frac{\partial B_y}{\partial x}\mathbf{e_y} - B_x\frac{\partial v_x}{\partial x}\mathbf{e_x} - B_x\frac{\partial v_y}{\partial x}\mathbf{e_y} = 0.\end{aligned} \tag{21}$$

This simplifies due to cancelling terms and B_x being constant to give:

$$\frac{\partial B_y}{\partial t}\mathbf{e_y} + \frac{\partial v_x}{\partial x}B_y\mathbf{e_y} + v_x\frac{\partial B_y}{\partial x}\mathbf{e_y} - B_x\frac{\partial v_y}{\partial x}\mathbf{e_y} = 0. \tag{22}$$

The second and third terms of equation (22) combine through the chain rule, which results in the following induction equation:

$$\frac{\partial}{\partial t}(B_y) + \frac{\partial}{\partial x}(v_x B_y) = B_x\frac{\partial}{\partial x}(v_y)\,. \tag{2.31}$$

Appendix B

Analytical Solutions

In the sub-Alfvénic region ($z > 0$), equation (3.16) can be transformed into the modified Bessel's equation when $\nu \neq -1$ [Polyanin and Zaitsev, 2002, page 242]:

$$\frac{d^2y}{dx^2} + \frac{1}{x}\frac{dy}{dx} - \left(1 + \frac{\nu^2}{x^2}\right) y = 0, \tag{23}$$

where

$$y = x^{-\nu} w, \tag{24}$$

and

$$x = (\nu + 1)\sqrt{\tau - 1}. \tag{25}$$

The solutions to equation (23) are expressed in terms of the modified Bessel functions [Abramowitz and Stegun, 1972, page 374]. When $\Re(\nu) \leq 0$ and $\nu \neq -1$ the corresponding general solution to equation (3.13) is:

$$\hat{b}_\theta = x^\nu y\tau = (\nu+1)^\nu \left(\exp\left(\frac{z}{z_0}\right) - 1\right)^{\frac{\nu}{2}} \exp\left(\frac{z}{z_0}\right)$$
$$\times \quad \left[C_1 I_{-\nu}\left((\nu+1)\sqrt{\exp\left(\frac{z}{z_0}\right) - 1}\right) + C_2 K_{-\nu}\left((\nu+1)\sqrt{\exp\left(\frac{z}{z_0}\right) - 1}\right)\right], \tag{26}$$

where C_1 and C_2 are arbitrary constants. Using the limiting forms of the modified Bessel functions [Olver and Maximon, 2010, 10.30.1, 10.30.2] and assuming that

$\nu \neq 0$, we obtain:

$$\hat{b}_\theta \sim (\nu+1)^\nu \left(\exp\left(\frac{z}{z_0}\right)-1\right)^{\frac{\nu}{2}} \exp\left(\frac{z}{z_0}\right) \times \left[C_1 \left(\frac{\nu+1}{2}\right)^{-\nu} \Gamma(1-\nu) \left(\exp\left(\frac{z}{z_0}\right)-1\right)^{-\frac{\nu}{2}} + C_2 \left(\frac{\nu+1}{2}\right)^{\nu} \frac{\Gamma(-\nu)}{2} \left(\exp\left(\frac{z}{z_0}\right)-1\right)^{\frac{\nu}{2}}\right], \tag{27}$$

when $z \to 0^+$, which will remain finite only when $C_2 = 0$. A similar result is obtained when $\nu = 0$ [Olver and Maximon, 2010, 10.30.3]. We also require the solution to remain finite when $z \to \infty$. A finite $\hat{b}_\theta$ is equivalent to the magnetic energy density being finite. However, the solution (26) with $C_2 = 0$ is unbounded when $z \to \infty$ because $I_{-\nu}$ increases exponentially [Olver and Maximon, 2010, 10.30.4, 10.30.5, and 10.45.5]:

$$I_{-\nu}\left((\nu+1)\sqrt{\exp\left(\frac{z}{z_0}\right)-1}\right) \sim \frac{\exp\left((\nu+1)\sqrt{\exp\left(\frac{z}{z_0}\right)-1}\right)}{\sqrt{2\pi\left((\nu+1)\sqrt{\exp\left(\frac{z}{z_0}\right)-1}\right)}} \quad \text{when} \quad -1 < \Re(\nu) \leq 0, \tag{28}$$

$$I_{-\nu}\left((\nu+1)\sqrt{\exp\left(\frac{z}{z_0}\right)-1}\right) \sim \frac{\exp\left(-(\nu+1)\sqrt{\exp\left(\frac{z}{z_0}\right)-1}\right)}{\sqrt{2\pi\left((\nu+1)\sqrt{\exp\left(\frac{z}{z_0}\right)-1}\right)}} \quad \text{when} \quad \Re(\nu) < -1. \tag{29}$$

We conclude that equation (3.13) only has a trivial solution when $\Re(\nu) \leq 0$ and $\nu \neq -1$. For $\nu = -1$ the general solution to equation (3.13) is:

$$\hat{b}_\theta = \frac{1}{u_0}\left[C_1 + \frac{C_2}{\sqrt{\exp\left(\frac{z}{z_0}\right)-1}}\right]. \tag{30}$$

It will remain finite at $z = 0$, and $z = \infty$ only if $C_1 = C_2 = 0$. Therefore, only a trivial solution exists when $\nu = -1$.

Next we consider the case when $\Re(\nu) > 0$. The general solution to equation (23) represents a linear combination of I_ν and K_ν. The behaviour of I_ν is still determined by an estimate similar to (28) when $z \to \infty$ and, therefore, the corresponding coefficient must be set to zero to satisfy the requirement of finite energy density. The solution to equation (3.13) is therefore expressed in terms of the modified Bessel function K_ν:

$$\hat{b}_\theta = C \exp\left(\frac{z}{z_0}\right)\left((\nu+1)\sqrt{\exp\left(\frac{z}{z_0}\right)-1}\right)^{\nu} \times K_\nu\left((\nu+1)\sqrt{\exp\left(\frac{z}{z_0}\right)-1}\right). \quad (31)$$

An important asymptotic property of the modified Bessel function K_ν is the exponential decay at infinity [Olver and Maximon, 2010, 10.25.3]. Thus the solution (31) vanishes when $z \to \infty$ and the requirement of a finite magnetic energy density is satisfied. Using equation (3.2) it is easy to show that the kinetic energy density, $\rho_0 \hat{v}_\theta^2$ also remains finite as $z \to \infty$.

We note that as $z \to 0^+$ the behaviour of the function K_ν is determined by:

$$K_\nu\left((\nu+1)\sqrt{\exp\left(\frac{z}{z_0}\right)-1}\right) \sim \frac{\Gamma(\nu)}{2}\left(\frac{\nu+1}{2}\right)^{-\nu}\left(\exp\left(\frac{z}{z_0}\right)-1\right)^{-\frac{\nu}{2}}, \quad (32)$$

where $\Re(\nu) > 0$ [Olver and Maximon, 2010, 10.30.2]. This gives the following estimate for $\hat{b}_\theta$ near $z = 0$:

$$\hat{b}_\theta \sim C 2^{\nu-1}\Gamma(\nu)\exp\left(\frac{z}{z_0}\right), \quad (33)$$

for small z. Hence, the solution (31) is finite near $z = 0$ if $\Re(\nu) > 0$. The constant coefficient, C is determined from expression (33):

$$C = \frac{\hat{b}_\theta(0)}{2^{\nu-1}\Gamma(\nu)}. \tag{34}$$

The growth rate is determined by the expression:

$$\Im(\omega) = -\frac{1+\Re(\nu)}{2}\left[\frac{du_0}{dz}\right]_{z=0}, \tag{35}$$

where the ratio $-u_0(0)/z_0$ has been replaced by the flow derivative at $z = 0$.

For $-\infty < z < 0$ $(0 < \tau < 1)$ equation (3.16) is transformed into Bessel's equation:

$$\frac{d^2\tilde{y}}{d\tilde{x}^2} + \frac{1}{\tilde{x}}\frac{d\tilde{y}}{d\tilde{x}} + \left(1 - \frac{\nu^2}{\tilde{x}^2}\right)\tilde{y} = 0, \tag{36}$$

where

$$\tilde{y} = \tilde{x}^{-\nu}w = \frac{\tilde{x}^{-\nu}\hat{b}_\theta}{\tau}, \tag{37}$$

and

$$\tilde{x} = (\nu+1)\sqrt{1-\tau}. \tag{38}$$

The solution to equation (36) is expressed in terms of the Bessel functions. The corresponding general solution to equation (3.13) is:

$$\hat{b}_\theta = \tilde{x}^\nu\tilde{y}\tau = (\nu+1)^\nu\left(1-\exp\left(\frac{z}{z_0}\right)\right)^{\frac{\nu}{2}}\exp\left(\frac{z}{z_0}\right)$$
$$\times\left[C_1 J_\nu\left((\nu+1)\sqrt{1-\exp\left(\frac{z}{z_0}\right)}\right) + C_2 Y_\nu\left((\nu+1)\sqrt{1-\exp\left(\frac{z}{z_0}\right)}\right)\right]. \tag{39}$$

For $z \to 0^-$ we have [Olver and Maximon, 2010, 10.7.3, 10.7.4]:

$$\hat{b}_\theta \sim (\nu+1)^\nu \left(1-\exp\left(\frac{z}{z_0}\right)\right)^{\frac{\nu}{2}} \exp\left(\frac{z}{z_0}\right) \times\left[\frac{C_1}{\Gamma(\nu+1)}\left(\frac{\nu+1}{2}\right)^\nu \left(1-\exp\left(\frac{z}{z_0}\right)\right)^{\frac{\nu}{2}} - \frac{C_2\Gamma(\nu)}{\pi}\left(\frac{\nu+1}{2}\right)^{-\nu}\left(1-\exp\left(\frac{z}{z_0}\right)\right)^{-\frac{\nu}{2}}\right]. \tag{40}$$

Therefore, the solution remains finite near $z = 0$, and the coefficient C_2 is determined by:

$$C_2 = -\frac{\pi \hat{b}_\theta(0)}{2^\nu \Gamma(\nu)}. \tag{41}$$

The coefficient, C_1 can be determined by imposing a boundary condition at $z = -\infty$. Any perturbation in the super-Alfvénic region should be swept in the positive z direction, so there should be no propagation in the negative z direction. We therefore require the perturbations $\hat{b}_\theta$ and $\hat{v}_\theta$ to vanish when $z \to -\infty$. The variable $\hat{b}_\theta$ automatically vanishes due to the presence of the factor τ in the expression (39). The same is not true for $\hat{v}_\theta$. Using equations (3.2) and (3.3) the following relationship can be derived:

$$B_0 \frac{\partial v_\theta}{\partial t} + u_0 \frac{\partial b_\theta}{\partial t} = u_0 \frac{\partial}{\partial z}\left[\left(\frac{c_A^2}{u_0^2} - 1\right) u_0 b_\theta\right], \tag{42}$$

which allows us to express $\hat{v}_\theta$ in terms of $w = \hat{b}_\theta/\tau$:

$$\frac{B_0 \hat{v}_\theta}{u_0(0)} = \frac{2}{1+\nu}\left[(\tau-1)\frac{dw}{d\tau} + \frac{1-\nu}{2} w\right]. \tag{43}$$

Using the formulae for the derivatives of the Bessel functions we have [Abramowitz and Stegun, 1972, page 361]:

$$\frac{B_0\hat{v}_\theta}{u_0(0)} = (\nu+1)^\nu \left(1-\exp\left(\frac{z}{z_0}\right)\right)^{\frac{\nu+1}{2}} \times \left[C_1 J_{\nu-1}\left((\nu+1)\sqrt{1-\exp\left(\frac{z}{z_0}\right)}\right) + C_2 Y_{\nu-1}\left((\nu+1)\sqrt{1-\exp\left(\frac{z}{z_0}\right)}\right)\right] + \frac{1-\nu}{(1+\nu)^{1-\nu}}\left(1-\exp\left(\frac{z}{z_0}\right)\right)^{\frac{\nu}{2}} \times \left[C_1 J_{\nu}\left((\nu+1)\sqrt{1-\exp\left(\frac{z}{z_0}\right)}\right) + C_2 Y_{\nu}\left((\nu+1)\sqrt{1-\exp\left(\frac{z}{z_0}\right)}\right)\right]. \tag{44}$$

Firstly, using equation (44) and a similar expression for $\hat{v}_\theta$ in the region $z > 0$ it can be shown that $\hat{v}_\theta$ is continuous across $z = 0$. Secondly, the condition on $\hat{v}_\theta$ to vanish when $z \to -\infty$ determines the coefficient, C_1:

$$C_1 = \frac{(\nu-1)Y_\nu(\nu+1) - (\nu+1)Y_{\nu-1}(\nu+1)}{(\nu-1)J_\nu(\nu+1) - (\nu+1)J_{\nu-1}(\nu+1)}C_2. \tag{45}$$

Energy equation

We multiply equation (3.1) by v_θ, and equation (3.2) by b_θ/μ_0:

$$\rho_0 v_\theta \frac{\partial v_\theta}{\partial t} + u_0\rho_0 v_\theta \frac{\partial v_\theta}{\partial z} = \frac{B_0}{\mu_0} v_\theta \frac{\partial b_\theta}{\partial z}, \tag{46}$$

$$\frac{b_\theta}{\mu_0}\frac{\partial b_\theta}{\partial t} + \frac{u_0 b_\theta}{\mu_0}\frac{\partial b_\theta}{\partial z} = \frac{B_0}{\mu_0} b_\theta \frac{\partial v_\theta}{\partial z} - \frac{b_\theta^2}{\mu_0}\frac{\partial u_0}{\partial z}. \tag{47}$$

Adding equations (46) and (47), we obtain

$$\frac{\partial}{\partial t}\left[\frac{\rho_0 v_\theta^2}{2} + \frac{b_\theta^2}{2\mu_0}\right] = \frac{B_0}{\mu_0}\frac{\partial}{\partial z}(v_\theta b_\theta) - \frac{\rho_0 u_0}{2}\frac{\partial v_\theta^2}{\partial z} - u_0\frac{\partial}{\partial z}\left[\frac{b_\theta^2}{2\mu_0}\right] - \frac{b_\theta^2}{\mu_0}\frac{\partial u_0}{\partial z}, \tag{48}$$

where the density, ρ_0 has been taken inside the square brackets as it does not depend on time. Equation (48) can be rewritten in the following form:

$$\frac{\partial}{\partial t}\left[\frac{\rho_0 v_\theta^2}{2}+\frac{b_\theta^2}{2\mu_0}\right]=\frac{B_0}{\mu_0}\frac{\partial}{\partial z}\left(v_\theta b_\theta\right)-u_0\frac{\partial}{\partial z}\left[\frac{\rho_0 v_\theta^2}{2}+\frac{b_\theta^2}{2\mu_0}\right]+\frac{u_0}{2}\frac{\partial \rho_0}{\partial z}v_\theta^2-\frac{\partial u_0}{\partial z}\frac{b_\theta^2}{\mu_0}, \quad (49)$$

where we have used the equality:

$$-\frac{\rho_0 u_0}{2}\frac{\partial v_\theta^2}{\partial z}=-u_0\frac{\partial}{\partial z}\left(\frac{\rho_0 v_\theta^2}{2}\right)+\frac{u_0}{2}\frac{\partial \rho_0}{\partial z}v_\theta^2. \quad (50)$$

The condition of mass conservation, $\rho_0 u_0 = \text{const}$ can be used to reduce equation (49) to:

$$\frac{\partial}{\partial t}\left[\frac{\rho_0 v_\theta^2}{2}+\frac{b_\theta^2}{2\mu_0}\right]=\frac{B_0}{\mu_0}\frac{\partial}{\partial z}\left(v_\theta b_\theta\right)-u_0\frac{\partial}{\partial z}\left[\frac{\rho_0 v_\theta^2}{2}+\frac{b_\theta^2}{2\mu_0}\right]-\frac{\partial u_0}{\partial z}\left[\frac{\rho_0 v_\theta^2}{2}+\frac{b_\theta^2}{2\mu_0}\right]-\frac{\partial u_0}{\partial z}\frac{b_\theta^2}{2\mu_0}, \quad (51)$$

or

$$\frac{\partial W_T}{\partial t}+\frac{\partial F_W}{\partial z}=-\frac{\partial u_0}{\partial z}W_m, \quad (52)$$

where W_T is the sum of the kinetic and magnetic energy densities:

$$W_T = W_k + W_m = \frac{\rho_0 v_\theta^2}{2}+\frac{b_\theta^2}{2\mu_0}, \quad (53)$$

and

$$F_W = u_0 W_T - \frac{B_0}{\mu_0}v_\theta b_\theta. \quad (54)$$

Appendix C

Derivation of the Energy Equation

The chain rule can be applied to the θ-momentum equation (4.3) so that it becomes:

$$\rho\frac{\partial v_\theta}{\partial t} = -\rho v_z\frac{\partial v_\theta}{\partial z} + \frac{B_0}{\mu_0}\frac{\partial b_\theta}{\partial z}. \tag{55}$$

We multiply the θ-components of the momentum (55) and induction (4.5) equations by v_θ and b_θ/μ_0, correspondingly:

$$\rho v_\theta\frac{\partial v_\theta}{\partial t} = -\rho v_\theta v_z\frac{\partial v_\theta}{\partial z} + v_\theta\frac{B_0}{\mu_0}\frac{\partial b_\theta}{\partial z}, \tag{56}$$

and

$$\frac{b_\theta}{\mu_0}\frac{\partial b_\theta}{\partial t} = \frac{b_\theta}{\mu_0}\left(-v_z\frac{\partial b_\theta}{\partial z} - \frac{\partial v_z}{\partial z}b_\theta + B_0\frac{\partial v_\theta}{\partial z}\right). \tag{57}$$

By taking the sum of the above two equations we obtain the time derivative of the θ-component of the energy density, W_θ:

$$\begin{aligned}\frac{\partial W_\theta}{\partial t} &= \frac{\partial}{\partial t}\left(\frac{\rho v_\theta^2}{2} + \frac{b_\theta^2}{2\mu_0}\right) = \\ &= \frac{v_\theta^2}{2}\frac{\partial\rho}{\partial t} - \rho v_z v_\theta\frac{\partial v_\theta}{\partial z} + \frac{B_0}{\mu_0}v_\theta\frac{\partial b_\theta}{\partial z} - \frac{v_z b_\theta}{\mu_0}\frac{\partial b_\theta}{\partial z} - \frac{\partial v_z}{\partial z}\frac{b_\theta^2}{\mu_0} + \frac{B_0}{\mu_0}b_\theta\frac{\partial v_\theta}{\partial z} = \\ &= \frac{v_\theta^2}{2}\frac{\partial\rho}{\partial t} + \frac{B_0}{\mu_0}\frac{\partial}{\partial z}(v_\theta b_\theta) - v_z\frac{\partial}{\partial z}\left(\frac{\rho v_\theta^2}{2} + \frac{b_\theta^2}{2\mu_0}\right) + \frac{v_z v_\theta^2}{2}\frac{\partial\rho}{\partial z} - \frac{\partial v_z}{\partial z}\frac{b_\theta^2}{\mu_0}.\end{aligned} \tag{58}$$

From the continuity equation (4.1) we have:

$$\frac{v_z v_\theta^2}{2}\frac{\partial \rho}{\partial z} = -\frac{v_\theta^2}{2}\left(\frac{\partial \rho}{\partial t} + \rho\frac{\partial v_z}{\partial z}\right). \tag{59}$$

Substituting equation (59) into (58) and rearranging the terms, we obtain the equation of azimuthal energy:

$$\frac{\partial W_\theta}{\partial t} = \frac{\partial}{\partial z}\left(\frac{B_0}{\mu_0} v_\theta b_\theta - v_z W_\theta\right) - \frac{\partial v_z}{\partial z}\frac{b_\theta^2}{2\mu_0}, \tag{60}$$

or

$$\frac{\partial W_\theta}{\partial t} + \frac{\partial F_\theta}{\partial z} = -\frac{\partial v_z}{\partial z}\frac{b_\theta^2}{2\mu_0}, \tag{61}$$

where $F_\theta = v_z W_\theta - \frac{B_0}{\mu_0} v_\theta b_\theta$ is the azimuthal component of the energy flux.

Bibliography

Abramowitz, M and I A Stegun (1972), *Handbook of Mathematical Functions*. Washington, D.C. 145, 150

Acheson, D J (1976), "On over-reflexion." *Journal of Fluid Mechanics*, 77, 433–472. 20, 116

Alfvén, H (1942), "Existence of electromagnetic-hydrodynamic waves." *Nature*, 150, 405–406. 6

An, C H, Z E Musielak, R L Moore, and S T Suess (1989), "Reflection and trapping of transient alfvén waves propagating in an isothermal atmosphere with constant gravity and uniform magnetic field." *The Astrophysical Journal*, 345, 597–605. 73

Arregui, I, R Oliver, and J L Ballester (2012), "Prominence oscillations." *Living Reviews in Solar Physics*, 9, 1–109. 102

Aschwanden, M J (2005), *Physics of the Solar Corona: An Introduction with Problems and Solutions*. Springer. 16, 36

Ballester, J L (2006), "Solar corona seismology." *Lecture Notes and Essays in Astrophysics*, 2, 91–110. 5

Ballester, J L, R Erdélyi, A W Hood, J W Leibacher, and V M Nakariakov (2007), "Preface: A topical issue in honor of professor bernard roberts." *Solar Physics*, 246, 1–2. 5

Banerjee, D, R Erdelyi, R Oliver, and E OShea (2007), "Present and future observing trends in atmospheric magnetoseismology." *Solar Physics*, 246, 3–29. 5

Baranov, V B, A A Barmin, and E A Pushkar (1996), "On the interaction of interplanetary shock waves with a stationary shock wave in the solar wind: Oblique magnetohydrodynamic interaction." *Astronomy Letters*, 22, 555–561. 21

Beckers, J M (1968), "Solar spicules." *Solar Physics*, 3, 367–433. 19

Beckers, J M (1972), "Solar spicules." *Annual Review of Astronomy and Astrophysics*, 10, 73. 19

Berger, T E, R A Shine, G L Slater, T D Tarbell, T J Okamoto, K Ichimoto, Y Katsukawa, Y Suematsu, S Tsuneta, B W Lites, et al. (2008), "Hinode sot observations of solar quiescent prominence dynamics." *The Astrophysical Journal Letters*, 676, L89. 101, 132, 133

Bethge, C, C Beck, H Peter, and A Lagg (2012), "Siphon flow in a cool magnetic loop." *Astronomy & Astrophysics*, 537, A130. 103

Biskamp, D (1997), *Nonlinear magnetohydrodynamics*, volume 1. Cambridge University Press. 9

Bonet, J A, I Márquez, J Sánchez Almeida, I Cabello, and V Domingo (2008), "Convectively driven vortex flows in the sun." *The Astrophysical Journal Letters*, 687, L131. 20, 67, 99

Bonet, J A, I Márquez, J Sánchez Almeida, J Palacios, V M Pillet, S K Solanki, J C del Toro Iniesta, V Domingo, T Berkefeld, W Schmidt, et al. (2010), "Sunrise/imax observations of convectively driven vortex flows in the sun." *The Astrophysical Journal Letters*, 723, L139. 20, 67, 99

Book, D L, C Li, G Patnaik, and F F Grinstein (1991), "Quantifying residual numerical diffusion in flux-corrected transport algorithms." *Journal of scientific computing*, 6, 323–343. 26

Boris, J P and D L Book (1973), "Flux-corrected transport. i. shasta, a fluid transport algorithm that works." *Journal of Computational Physics*, 11, 38–69. 22

Boris, J P, A M Landsberg, E S Oran, and J H Gardner (1993), "Lcpfct-a flux-corrected transport algorithm for solving generalized continuity equations." Technical report, DTIC Document. 22, 80

Borrero, J M, A Lagg, S K Solanki, and M Collados (2005), "On the fine structure of sunspot penumbrae-ii. the nature of the evershed flow." *Astronomy & Astrophysics*, 436, 333–345. 21

Brandt, P N, G B Scharmert, S Ferguson, R A Shine, T D Tarbell, A M Title, et al. (1988), "Vortex flow in the solar photosphere." *nature*, 335, 238–240. 20

Bushby, P J, S M Houghton, M R E Proctor, and N O Weiss (2008), "Convective intensification of magnetic fields in the quiet sun." *Monthly Notices of the Royal Astronomical Society*, 387, 698–706. 66

Cally, P S (2012), "Alfvén reflection and reverberation in the solar atmosphere." *Solar Physics*, 280, 33–50. 73, 81

Cargill, P J and E R Priest (1980), "Siphon flows in coronal loops: I. adiabatic flow." *Solar Physics*, 65, 251–269. 103

Carroll, B W and D A Ostlie (2006), *An Introduction to Modern Astrophysics and Cosmology*. Springer. 1

Centeno, R, M Collados, and J T Bueno (2009), "Wave propagation and shock formation in different magnetic structures." *The Astrophysical Journal*, 692, 1211. 21

Chae, J (2010), "Dynamics of vertical threads and descending knots in a hedgerow prominence." *The Astrophysical Journal*, 714, 618. 101

Chae, J, K Ahn, E-K Lim, G S Choe, and T Sakurai (2008), "Persistent horizontal flows and magnetic support of vertical threads in a quiescent prominence." *The Astrophysical Journal Letters*, 689, L73. 101

Chae, J, H Wang, J Qiu, P R Goode, L Strous, and H S Yun (2001), "The formation of a prominence in active region noaa 8668. i. soho/mdi observations of magnetic field evolution." *The Astrophysical Journal*, 560, 476. 102

Courant, R and D Hilbert (1966), *Methods of mathematical physics*, volume 1. New York 1966. 75

Cranmer, S R and A A Van Ballegooijen (2005), "On the generation, propagation, and reflection of alfvén waves from the solar photosphere to the distant heliosphere." *The Astrophysical Journal Supplement Series*, 156, 265. 42

Danilovic, S, M Schüssler, and S K Solanki (2010), "Magnetic field intensification: comparison of 3d mhd simulations with hinode/sp results." *Astronomy & Astrophysics*, 509, A76. 66

De Moortel, I and V M Nakariakov (2012), "Magnetohydrodynamic waves and coronal seismology: an overview of recent results." *Philosophical Transactions of the Royal Society of London A: Mathematical, Physical and Engineering Sciences*, 370, 3193–3216. 5

De Pontieu, B, M Carlsson, L H M R van der Voort, R J Rutten, V H Hansteen, and H Watanabe (2012), "Ubiquitous torsional motions in type ii spicules." *The Astrophysical Journal Letters*, 752, L12. 19, 63

De Pontieu, B, R Erdélyi, and S P James (2004), "Solar chromospheric spicules from the leakage of photospheric oscillations and flows." *Nature*, 430, 536–539. 19

De Pontieu, B, S W McIntosh, M Carlsson, V H Hansteen, T D Tarbell, C J Schrijver, R A Shine, S Tsuneta, Y Katsukawa, K Ichimoto, et al. (2007), "Chromospheric alfvénic waves strong enough to power the solar wind." *Science*, 318, 1574–1577. 4, 19, 62

De Pontieu, B, L H M R van der Voort, S W McIntosh, T M D Pereira, M Carlsson, V Hansteen, H Skogsrud, J Lemen, P Boerner, N Hurlburt, et al. (2014), "On the prevalence of small-scale twist in the solar chromosphere and transition region." *Science*, 346, 1255732. 19, 62, 67

de Wijn, A G, J O Stenflo, S K Solanki, and S Tsuneta (2009), "Small-scale solar magnetic fields." *Space Sci Rev*, 144, 275–315. 66

Díaz, A J, R Oliver, J L Ballester, and R Soler (2011), "Twisted magnetic tubes with field aligned flow-i. linear twist and uniform longitudinal field." *Astronomy & Astrophysics*, 533, A95. 62, 64

Engvold, O (1976), "The fine structure of prominences." *Solar Physics*, 49, 283–295. 101

Erdélyi, R and M Goossens (2011), "Magnetohydrodynamic waves and seismology of the solar atmosphere." *Space Science Reviews*, 158, 167–168. 6

Erdélyi, R and S P James (2004), "Can ion-neutral damping help to form spicules? ii. random driver." *Astronomy and Astrophysics*, 427, 1055–1064. 19, 20, 31, 63

Fainshtein, V G and Ya I Egorov (2015), "Initiation of cmes associated with filament eruption, and the nature of cme related shocks." *Advances in Space Research*, 55, 798–807. 21

Farahani, S V, V M Nakariakov, E Verwichte, and T Van Doorsselaere (2012), "Nonlinear evolution of torsional alfvén waves." *Astronomy & Astrophysics*, 544, A127. 14

Fedun, V, S Shelyag, G Verth, M Mathioudakis, and R Erdélyi (2011), "Mhd waves generated by high-frequency photospheric vortex motions." *Annales Geophysicae-Atmospheres Hydrospheresand Space Sciences*, 29, 1029. 20

Ferraro, V C A (1954), "On the reflection and refraction of alfven waves." *The Astrophysical Journal*, 119, 393. 72, 73

Ferriz-Mas, A, M Schüssler, and V Anton (1989), "Dynamics of magnetic flux concentrations-the second-order thin flux tube approximation." *Astronomy and Astrophysics*, 210, 425–432. 70

Filippov, B, O Martsenyuk, A K Srivastava, and W Uddin (2015), "Solar magnetic flux ropes." *Journal of Astrophysics and Astronomy*, 36, 157–184. 102

Fischer, C E, A G de Wijn, R Centeno, B W Lites, and C U Keller (2009), "Statistics of convective collapse events in the photosphere and chromosphere observed with the hinode sot." *Astronomy & Astrophysics*, 504, 583–588. 66

Foster, J and F B Richards (1991), "The gibbs phenomenon for piecewise-linear approximation." *American Mathematical Monthly*, 47–49. 26

Georgakilas, A A, E B Christopoulou, A Skodras, and S Koutchmy (2003), "Chromospheric evershed flow." *Astronomy & Astrophysics*, 403, 1123–1133. 21

Grappin, R, J Léorat, and S R Habbal (2005), "Siphon flows and oscillations in long coronal loops due to alfvén waves." *Astronomy & Astrophysics*, 437, 1081–1092. 103

Grygorov, K, L Přech, J Šafránková, Z Němeček, and O Goncharov (2014), "The far magnetotail response to an interplanetary shock arrival." *Planetary and Space Science*, 103, 228–237. 21

Hollweg, J V (1978), "Alfvén waves in the solar atmosphere." *Solar Physics*, 56, 305–333. 73

Hollweg, J V (1981), "Alfven waves in the solar atmosphere." *Solar Physics*, 70, 25–66. 34, 40, 106

Hollweg, J V (1986), "Transition region, corona, and solar wind in coronal holes." *Journal of Geophysical Research: Space Physics (1978–2012)*, 91, 4111–4125. 40

Hollweg, J V (1992), "Alfvenically driven slow shocks in the solar chromosphere and corona." *The Astrophysical Journal*, 389, 731–738. 19, 21, 37, 50, 59, 63, 107

Hollweg, J V, S Jackson, and D Galloway (1982), "Alfvén waves in the solar atmosphere." *Solar Physics*, 75, 35–61. 3, 19, 34, 50, 63, 70, 106

Hugoniot, H (1889), "Memoir on the propagation of movements in bodies, especially perfect gases (second part)." *J. de lEcole Polytechnique*, 58, 1–125. 16, 21

James, S P, R Erdélyi, and B De Pontieu (2003), "Can ion-neutral damping help to form spicules?" *Astronomy & Astrophysics*, 406, 715–724. 3, 19, 20, 31, 63

Jess, D B, M Mathioudakis, R Erdélyi, P J Crockett, F P Keenan, and D J Christian (2009), "Alfvén waves in the lower solar atmosphere." *Science*, 323, 1582–1585. 19

Jess, D B, R J Morton, G Verth, V Fedun, S D T Grant, and I Giagkiozis (2015), "Multiwavelength studies of mhd waves in the solar chromosphere." *Space Science Reviews*, 1–59. 19

Keppens, R and C Xia (2014), "The dynamics of funnel prominences." *The Astrophysical Journal*, 789, 22. 102

Khomenko, E, A Kosovichev, M Collados, K Parchevsky, and V Olshevsky (2009), "Theoretical modeling of propagation of magnetoacoustic waves in magnetic regions below sunspots." *The Astrophysical Journal*, 694, 411. 41

Kitiashvili, I N, A G Kosovichev, N N Mansour, S K Lele, and A A Wray (2012b), "Vortex tubes of turbulent solar convection." *Physica Scripta*, 86, 018403. 67

Kitiashvili, I N, A G Kosovichev, N N Mansour, and A A Wray (2012a), "Dynamics of magnetized vortex tubes in the solar chromosphere." *The Astrophysical Journal Letters*, 751, L21. 67

Klimchuk, J A (2012), "The role of type ii spicules in the upper solar atmosphere." *Journal of Geophysical Research: Space Physics (1978–2012)*, 117. 4

Kudoh, T and K Shibata (1999), "Alfvén wave model of spicules and coronal heating." *The Astrophysical Journal*, 514, 493. 3, 19, 31, 34, 63, 64, 106

Laplace, P S de (1816), "Sur la vitesse du son dans lair et dans leau." *Ann. de Chim. et de Phys*, 3, 1816. 21

Leighton, R B (1960), "Preview on granulation: observational studies." *IAU Symposia*, 12, 321–327. 5

Li, X, H Morgan, D Leonard, and L Jeska (2012), "A solar tornado observed by aia/sdo: Rotational flow and evolution of magnetic helicity in a prominence and cavity." *The Astrophysical Journal Letters*, 752, L22. 20, 62, 63, 67, 133

Lin, Y, O Engvold, L H M R van der Voort, J E Wiik, and T E Berger (2005), "Thin threads of solar filaments." *Solar Physics*, 226, 239–254. 19

Lin, Y, O Engvold, and J Wiik (2003), "Counterstreaming in a large polar crown filament." *Solar Physics*, 216, 109–120. 19

Lugaz, N, C J Farrugia, C W Smith, and K Paulson (2015), "Shocks inside cmes: A survey of properties from 1997 to 2006." *Journal of Geophysical Research: Space Physics*, 120, 2409–2427. 21

Magdalenić, J, C Marqué, V Krupar, M Mierla, A N Zhukov, L Rodriguez, M Maksimović, and B Cecconi (2014), "Tracking the cme-driven shock wave on 2012 march 5 and radio triangulation of associated radio emission." *The Astrophysical Journal*, 791, 115. 21

Maltby, P (1975), "The chromospheric evershed flow." *Solar Physics*, 43, 91–105. 21

Matsumoto, T and K Shibata (2010), "Nonlinear propagation of alfvén waves driven by observed photospheric motions: Application to the coronal heating and spicule formation." *The Astrophysical Journal*, 710, 1857. 34, 63, 64, 106

Meyer, F and H U Schmidt (1968), "Magnetisch ausgerichtete strömungen zwischen sonnenflecken." *Zeitschrift Angewandte Mathematik und Mechanik*, 48, 218–221. 103

Moll, R, R H Cameron, and M Schüssler (2011), "Vortices in simulations of solar surface convection." *Astronomy & Astrophysics*, 533, A126. 67, 68

Montesinos, B and J H Thomas (1997), "The evershed effect in sunspots as a siphon flow along a magnetic flux tube." *Nature*, 390, 485–487. 19, 103

Muthsam, H J, F Kupka, B Löw-Baselli, C Obertscheider, M Langer, and P Lenz (2010), "Antares–a numerical tool for astrophysical research with applications to solar granulation." *New Astronomy*, 15, 460–475. 67

Nagata, S, S Tsuneta, Y Suematsu, K Ichimoto, Y Katsukawa, T Shimizu, T Yokoyama, T D Tarbell, B W Lites, R A Shine, et al. (2008), "Formation of solar magnetic flux tubes with kilogauss field strength induced by convective instability." *The Astrophysical Journal Letters*, 677, L145. 66

Nesis, A, R Hammer, M Roth, and H Schleicher (2001), "Dynamics of the solar granulation-vii. a nonlinear approach." *Astronomy & Astrophysics*, 373, 307–317. 66

Nordlund, Å, R F Stein, and M Asplund (2009), "Solar surface convection." *Living Reviews in Solar Physics*, 6, 1–117. 67

Okamoto, T J, S Tsuneta, T E Berger, K Ichimoto, Y Katsukawa, B W Lites, S Nagata, K Shibata, T Shimizu, R A Shine, et al. (2007), "Coronal transverse magnetohydrodynamic waves in a solar prominence." *Science*, 318, 1577–1580. 101

Okamoto, T J, S Tsuneta, B W Lites, M Kubo, T Yokoyama, T E Berger, K Ichimoto, Y Katsukawa, S Nagata, K Shibata, et al. (2009), "Prominence formation associated with an emerging helical flux rope." *The Astrophysical Journal*, 697, 913. 102

Olver, F W J and L C Maximon (2010), "Bessel functions. in: Digital library of mathematical functions." URL `http://dlmf.nist.gov/10.` 145, 146, 147, 149

Orlando, S, G Peres, and S Serio (1995a), "Models of stationary siphon flows in stratified, thermally conducting coronal loops. 1: Regular solutions." *Astronomy and Astrophysics*, 294, 861–873. 19, 103

Orlando, S, G Peres, and S Serio (1995b), "Models of stationary siphon flows in stratified, thermally conducting coronal loops. ii. shocked solutions." *Astronomy and Astrophysics*, 300, 549–558. 19, 21, 103, 104, 106, 113

Panasenco, O, S F Martin, and M Velli (2014), "Apparent solar tornado-like prominences." *Solar Physics*, 289, 603–622. 20

Parenti, S (2014), "Solar prominences: observations." *Living Reviews in Solar Physics*, 11, 1–88. 103

Pereira, T M D, B De Pontieu, and M Carlsson (2012), "Quantifying spicules." *The Astrophysical Journal*, 759, 18. 4

Pishkalo, M I (1994), "Non-rigid rotation of solar spicules." *Astronomische Nachrichten*, 315, 391–397. 19

Plaza, C W, J C del Toro Iniesta, B R Cobo, V M Pillet, B W Lites, and A Skumanich (1997), "Evidence for a downward mass flux in the penumbral region of a sunspot." *Nature*, 389, 47–49. 19

Poisson, S D (1808), "Mémoire sur la théorie du son." *Journal de lEcole polytechnique*, 14, 319–392. 21

Polyanin, A D and V E Zaitsev (2002), *Handbook of exact solutions for ordinary differential equations*. CRC Press. 145

Priest, E (2014), *Magnetohydrodynamics of the Sun*. Cambridge University Press. 5, 6, 11, 12, 17, 35, 39, 50, 89, 107, 116

Priest, E R, A W Hood, and U Anzer (1989), "A twisted flux-tube model for solar prominences. i-general properties." *The Astrophysical Journal*, 344, 1010–1025. 102

Rankine, W J M (1859), "On the thermo-dynamic theory of steam-engines with dry saturated steam, and its application to practice." *Philosophical Transactions of the Royal Society of London*, 149, 177–192. 16, 21

Rimmele, T R (1994), "On the temporal behaviour of the evershed effect." *Astronomy and Astrophysics*, 290, 972–982. 61

Roberts, B, PM Edwin, and AO Benz (1984), "On coronal oscillations." *The Astrophysical Journal*, 279, 857–865. 5

Ryutova, M and T Tarbell (2003), "Mhd shocks and the origin of the solar transition region." *Physical review letters*, 90, 191101. 21

Schmieder, B and P Mein (1989), "Evolution of fine structures in a filament." *Hvar Observatory Bulletin*, 13, 31. 101

Schmieder, B, M A Raadu, and J E Wiik (1991), "Fine structure of solar filaments. ii-dynamics of threads and footpoints." *Astronomy and Astrophysics*, 252, 353–365. 101

Scullion, E, R Erdélyi, V Fedun, and J G Doyle (2011), "The response of a three-dimensional solar atmosphere to wave-driven jets." *The Astrophysical Journal*, 743, 14. 19

Shelyag, S, P S Cally, A Reid, and M Mathioudakis (2013), "Alfvén waves in simulations of solar photospheric vortices." *The Astrophysical Journal Letters*, 776, L4. 62, 67

Shelyag, S, P Keys, M Mathioudakis, and F P Keenan (2011), "Vorticity in the solar photosphere." *Astronomy & Astrophysics*, 526, A5. 68

Shimizu, T, B W Lites, Y Katsukawa, K Ichimoto, Y Suematsu, S Tsuneta, S Nagata, M Kubo, R A Shine, and T D Tarbell (2008), "Frequent occurrence of high-speed local mass downflows on the solar surface." *The Astrophysical Journal*, 680, 1467. 66

Solanki, S K, B Inhester, and M Schüssler (2006), "The solar magnetic field." *Reports on Progress in Physics*, 69, 563. 66

Spruit, H C and E G Zweibel (1979), "Convective instability of thin flux tubes." *Solar Physics*, 62, 15–22. 66

Spurk, J and N Aksel (2008), "Fluid mechanics, softcover reprint of hardcover 2nd ed." 67, 71

Stein, R F and Å Nordlund (1989), "Topology of convection beneath the solar surface." *The Astrophysical Journal*, 342, L95–L98. 66

Stein, R F and Å Nordlund (2006), "Solar small-scale magnetoconvection." *The Astrophysical Journal*, 642, 1246. 66, 68

Steiner, O, M Franz, N B González, C Nutto, R Rezaei, V M Pillet, J A Bonet Navarro, J C del Toro Iniesta, V Domingo, S K Solanki, et al. (2010), "Detection of vortex tubes in solar granulation from observations with sunrise." *The Astrophysical Journal Letters*, 723, L180. 67

Sterling, A C (2000), "Solar spicules: A review of recent models and targets for future observations–(invited review)." *Solar Physics*, 196, 79–111. 3, 4, 19

Sterling, A C and J V Hollweg (1988), "The rebound shock model for solar spicules-dynamics at long times." *The Astrophysical Journal*, 327, 950–963. 19, 34, 106

Su, Y, P Gömöry, A Veronig, M Temmer, T Wang, K Vanninathan, W Gan, and Y Li (2014), "Solar magnetized tornadoes: Rotational motion in a tornado-like prominence." *The Astrophysical Journal Letters*, 785, L2. 62

Tandberg-Hanssen, E (1995), "The nature of solar prominences." *Astrophysics and Space Science Library*, 199. 101

Tao, L, N O Weiss, D P Brownjohn, and M R E Proctor (1998), "Flux separation in stellar magnetoconvection." *The Astrophysical Journal Letters*, 496, L39. 66

Taroyan, Y (2008), "Alfvén instability in a compressible flow." *Physical review letters*, 101, 245001. 20, 27, 43, 69, 72, 104, 131

Taroyan, Y (2009), "Alfven instability in coronal loops with siphon flows." *The Astrophysical Journal*, 694, 69. 20, 103, 104

Taroyan, Y (2011), "Alfvén instability of steady state flux tubes. isothermal flow." *Astronomy & Astrophysics*, 533, A68. 20, 104

Taroyan, Y (2015), "Alfvén instability of steady state flux tubes-ii. upflows in stratified atmospheres." *Astronomy & Astrophysics*, 575, A104. 20, 104

Taroyan, Y and T Williams (2016), "Magnetic field twisting by intergranular downdrafts." *The Astrophysical Journal*, 829, 107. 65, 104, 106, 109

Thelen, J C and F Cattaneo (2000), "Dynamo action driven by convection: the influence of magnetic boundary conditions." *Monthly Notices of the Royal Astronomical Society*, 315, L13–L17. 66

Thomas, J H (1988), "Siphon flows in isolated magnetic flux tubes." *The Astrophysical Journal*, 333, 407–419. 103

Title, A M, K P Topka, T D Tarbell, W Schmidt, C Balke, G Scharmer, et al. (1992), "On the differences between plage and quiet sun in the solar photosphere." *The Astrophysical Journal*, 393, 782–794. 21

Titov, V S and P Démoulin (1999), "Basic topology of twisted magnetic configurations in solar flares." *Astronomy and Astrophysics*, 351, 707–720. 104

Török, T and B Kliem (2005), "Confined and ejective eruptions of kink-unstable flux ropes." *The Astrophysical Journal Letters*, 630, L97. 102, 104, 132

Tóth, G (1997), "Versatile advection code." In *High-Performance Computing and Networking*, 253–262, Springer. 31, 36, 91, 106

Tsiropoula, G, K Tziotziou, I Kontogiannis, M S Madjarska, J G Doyle, and Y Suematsu (2012), "Solar fine-scale structures. i. spicules and other small-scale, jet-like events at the chromospheric level: observations and physical parameters." *Space science reviews*, 169, 181–244. 3

Uchida, Y (1970), "Diagnosis of coronal magnetic structure by flare-associated hydromagnetic disturbances." *Publications of the Astronomical Society of Japan*, 22, 341. 5

Van Ballegooijen, A A, M Asgari-Targhi, S R Cranmer, and E E DeLuca (2011), "Heating of the solar chromosphere and corona by alfvén wave turbulence." *The Astrophysical Journal*, 736, 3. 40

van Ballegooijen, A A and S R Cranmer (2010), "Tangled magnetic fields in solar prominences." *The Astrophysical Journal*, 711, 164. 101

van Ballegooijen, A A and P C H Martens (1989), "Formation and eruption of solar prominences." *The Astrophysical Journal*, 343, 971–984. 102

Versteeg, H K and W Malalasekera (2007), *An introduction to computational fluid dynamics the finite volume method*. Pearson Education. 32

Vögler, A (2005), "On the effect of photospheric magnetic fields on solar surface brightness. results of radiative mhd simulations." *Memorie della Societa Astronomica Italiana*, 76, 842. 66

Vranjes, J (2014), "Viscosity effects on waves in partially and fully ionized plasma in magnetic field." *Monthly Notices of the Royal Astronomical Society*, 445, 1614–1624. 20

Vršnak, B, V Ruždjak, R Brajša, and A Džubur (1988), "Structure and stability of prominences with helical structure." *Solar physics*, 116, 45–60. 101

Wang, Y-M and G Stenborg (2010), "Spinning motions in coronal cavities." *The Astrophysical Journal Letters*, 719, L181. 102

Webb, A R and B Roberts (1978), "Vertical motions in an intense magnetic flux tube." *Solar Physics*, 59, 249–274. 66

Wedemeyer-Böhm, S, E Scullion, O Steiner, L H M R van der Voort, J de La Cruz Rodriguez, V Fedun, and R Erdélyi (2012), "Magnetic tornadoes as energy channels into the solar corona." *Nature*, 486, 505–508. 20

Wedemeyer-Böhm, S, E Scullion, L H M R van der Voort, A Bosnjak, and P Antolin (2013), "Are giant tornadoes the legs of solar prominences?" *Astrophysical Journal*, 774. 67

Wedemeyer-Böhm, S and O Steiner (2014), "On the plasma flow inside magnetic tornadoes on the sun." *Publications of the Astronomical Society of Japan*, 66, S10. 62

Wedemeyer-Böhm, S and L H M R van der Voort (2009), "Small-scale swirl events in the quiet sun chromosphere." *Astronomy & Astrophysics*, 507, L9–L12. 67

Weiss, N O, M R E Proctor, and D P Brownjohn (2002), "Magnetic flux separation in photospheric convection." *Monthly Notices of the Royal Astronomical Society*, 337, 293–304. 66

Whitham, G B (2011), *Linear and nonlinear waves*, volume 42. John Wiley & Sons. 51

Wiegel, R L (1992), *Oceanographical engineering*. Courier Corporation. 84

Williams, T, Y Taroyan, and V Fedun (2016), "The non-linear evolution of a twist in a magnetic shocktube." *Astrophysical Journal*, 817:92, 12pp. 18, 104, 106, 107, 116, 120, 130, 131

Yan, X L, E R Priest, Q L Guo, Z K Xue, J C Wang, and L H Yang (2016), "The formation of an inverse s-shaped active-region filament driven by sunspot motion and magnetic reconnection." *The Astrophysical Journal*, 832, 23. 102

Yang, B, Y Jiang, J Yang, Y Bi, and H Li (2016), "Observations of the growth of an active region filament." *The Astrophysical Journal*, 830, 16. 102

Zaqarashvili, T V, A J Díaz, R Oliver, and J L Ballester (2010), "Instability of twisted magnetic tubes with axial mass flows." *Astronomy & Astrophysics*, 516, A84. 62, 64

Zaqarashvili, T V and R Erdélyi (2009), "Oscillations and waves in solar spicules." *Space science reviews*, 149, 355–388. 19

Zhang, Y Z, K Shibata, J X Wang, X J Mao, T Matsumoto, Y Liu, and J T Su (2012), "Revision of solar spicule classification." *The Astrophysical Journal*, 750, 16. 4

Zirker, J B, O Engvold, and S F Martin (1998), "Counter-streaming gas flows in solar prominences as evidence for vertical magnetic fields." *Nature*, 396, 440–441. 101